

Phase-space geometry of reaction–diffusion dynamics

Fridtjof Brauns, Jacob Halatek,^{*} and Erwin Frey[†]

*Arnold Sommerfeld Center for Theoretical Physics and Center for NanoScience,
Department of Physics, Ludwig-Maximilians-Universität München,
Theresienstraße 37, D-80333 München, Germany*

(Dated: April 18, 2022)

Experimental studies of protein pattern formation (both in vivo and in vitro) have stimulated new interest in the dynamics of reaction–diffusion systems. However, a comprehensive theoretical understanding of the dynamics of such highly nonlinear, spatially extended systems is still missing. In contrast, for dynamical systems described by ordinary differential equations, major insights can be gained from the geometric analysis of their phase-space structure, and this approach has proven invaluable in shaping our intuition about nonlinear dynamics. Here we show how such an analysis can be generalized to mass-conserving reaction–diffusion (McRD) systems, which are the generic case for intracellular protein pattern-forming systems.

We present a comprehensive theory for two-component McRD systems, which serve as paradigmatic minimal systems that encapsulate the core principles and concepts of our framework. The key insight is that shifting local equilibria — controlled by the local mass density — give rise to concentration gradients that drive diffusive redistribution of total density. Thereby local chemical equilibria serve as a ‘supporting framework’ (referred to as *scaffold* here) for patterns during their entire dynamics.

We show that the *reactive nullcline* (line of chemical equilibria) and the *flux-balance subspace*, where the diffusive fluxes are balanced, are the geometric objects that facilitate a full characterization of the reaction–diffusion dynamics in the phase plane of the reaction kinetics. (i) We demonstrate that the lateral instability underlying pattern formation in reaction–diffusion systems (‘Turing instability’) is a mass-redistribution instability (MRI). The mechanism underlying the emergence of MRIs is a feedback loop between shifting local equilibria and mass redistribution due to gradients induced by the shifting equilibria (mass redistribution cascade). The onset of an MRI is characterized by a simple geometric criterion based on the slope of the reactive nullcline. Whether the onset of MRI is sub- or supercritical is determined by the local curvature of the nullcline. (ii) Beyond the weakly nonlinear analysis, we find that the characteristics and bifurcations of stationary patterns can be graphically determined by a flux-balance construction on the reactive nullcline (akin to the ‘common tangent construction’ employed to find binodal and spinodal lines for phase separation at thermal equilibrium). (iii) By dissecting the patterns into spatial regions that exhibit characteristic signatures, we provide a complete quantitative characterization of all pattern types in two-component reaction-diffusion systems with mass conservation. Remarkably, our approach unambiguously reveals that excitability is inextricably linked to regional lateral instabilities and can be easily read off the nullcline shape.

Taken together, these results demonstrate that phase-space geometry provides the essential elements of a comprehensive theory of pattern formation far beyond the linear regime — the effects of nonlinearities on the global dynamics are simply encoded in the curved shape of the nullcline. We discuss several cases where the physical insights gained from our analysis can be generalized to other non-equilibrium systems. Local equilibria, and their dependence on conserved quantities, and the spatial dynamics of these quantities, endow phase space with a distinct structure that encapsulates a broad range of non-equilibrium phenomena.

CONTENTS

I. Introduction	3	A. Models used for illustration and numerical studies	40
A. Motivation and background	3	B. Numerical simulation	41
B. Summary of key results	4	C. Linear stability analysis	41
C. Structure of the paper	4	1. Canonical linear stability analysis	41
II. Two-component mass-conserving reaction–diffusion systems	5	2. Approximation close to the onset of lateral instability	42
III. Setting the stage — geometric structures in phase space	6	3. Jacobian of mass-redistribution instability	42
A. Phase-space analysis of a well-mixed system	6	4. Eigenvectors of MRI	43
B. Stationary patterns are embedded in a flux-balance subspace of phase space	7	5. A mechanical analog for MRI	44
C. Stationary patterns are scaffolded by local equilibria	8	D. Some comments on the adiabatic scaffolding limit	44
D. Lateral instability	10	E. Geometric construction of bifurcations	45
IV. Two diffusively coupled compartments	12	F. Numerical continuation of stationary patterns	46
A. Mass-redistribution instability is a generic physical principle	13	G. Approximation of peak/trough patterns	47
B. MRI terminates due to flux-turnover balance	18	H. Lateral excitability	48
I. Stability of stationary patterns	48	I. Weakly nonlinear analysis	50
V. Characterization of stationary patterns	19	J. Nullcline curvature approximation	51
A. Interface width	19	References	52
B. Pattern classification	20		
C. Generic bifurcation structure for the total density \bar{n}	22		
D. Summary — regions generalize the concept of local compartments	24		
VI. The reactive nullcline determines the excitability threshold	24		
VII. Complete bifurcation structure	26		
A. Generic bifurcation structure of stationary patterns for monostable reaction kinetics	27		
B. Locally bistable kinetics	28		
C. The cusp scenario is generic	31		
D. Sub- and supercriticality of lateral instability in finite sized systems	32		
VIII. Conclusions and Discussion	34		
A. Reaction–diffusion systems	34		
B. Related non-equilibrium systems	37		
C. Outlook — Generalization to systems with more components and more conserved species	38		
Acknowledgments	40		

* jacob.halatek@physik.uni-muenchen.de

† frey@lmu.de

I. INTRODUCTION

A. Motivation and background

Nonlinear systems are as prevalent in nature as they are difficult to deal with conceptually and mathematically. They exhibit a vast and often bewildering variety of phenomena, examples of which crop up in nearly every discipline of the natural sciences, engineering, and mathematics. These range from bistable switches and limit-cycle oscillations to propagating fronts and pulses, pattern formation, and (spatiotemporal) chaos [1–7].

Mathematically, dynamical systems are described by sets of coupled equations, which are often nonlinear ordinary or partial differential equations. Unfortunately, cases in which these equations can be solved in closed analytical form are rare, making nonlinear problems appear inaccessible to mathematical analysis at first sight. A key insight, going back to the work of Poincaré [8], was that geometric structures in the phase space of a system can provide qualitative information about the *global* dynamics (trajectories in phase space) without an explicit solution of the differential equations. The essence of this geometric reasoning can be understood by considering simple systems with only two independent variables; see e.g. Ref. [1, 2]. In this case, the key geometric objects are nullclines, defined as curves in phase space along which one of the system’s two variables is in equilibrium. Points at which nullclines intersect mark equilibria (fixed points) of the system. These geometric objects organize phase-space flow, and thereby allow us to infer the qualitative dynamics from the shapes and intersections of the nullclines. Key concepts like linear stability, excitability, multi-stability, and limit cycles can be understood at this geometric level [1, 2]. Transitions (bifurcations) between qualitatively different regimes are revealed by structural changes of the flow in phase space as the control parameters are varied. One key advantage of such a geometric approach to nonlinear dynamical systems is that it yields systematic physical insights into the processes driving dynamics without requiring the explicit solution of the full set of equations.

Starting with Poincaré’s fundamental insight, a powerful mathematical theory of dynamical systems has been developed which encompasses concepts like stability theory for fixed points and periodic orbits, invariant manifolds, and bifurcation theory. An overview can be found in the “Background Material” in Ref. [9]; for a comprehensive mathematical treatise see e.g. Ref. [10]. Beyond it’s core framework, nonlinear dynamics has served as the basis for many further developments such as catastrophe theory [11, 12], chaos and control theory [13].

The geometric approach to dynamical systems has greatly facilitated understanding of a broad range of phenomena, including firing of neurons [2, 14, 15], chaotic laser dynamics [16, 17], chemical and biochemical oscillators [4, 18] like circadian clocks [19] and cell-cycle oscillators [20], and even ocean circulation [21] or surging

glaciers [22], to give a few examples.

Note that in all of the above examples the dynamics is given by sets of ordinary differential equations (ODEs) without (explicitly) taking the system’s spatial extent into account. In contrast, phenomena such as wave propagation and pattern formation explicitly require a description on a spatially extended domain, and therefore involve partial differential equations (PDEs). Finding ways to generalize the geometric ideas developed for ODEs to such spatially extended nonlinear systems remains a huge scientific challenge.

Instances where this has been successfully achieved are rare. One classical approach for nonlinear systems in one spatial dimension is the construction of steady-state patterns (including traveling-wave solutions in a co-moving frame). Mathematically, the steady state of a set of PDEs in one spatial dimension is described by a set of ODEs, which can be analyzed based on their phase-space geometry (see e.g. Ref. [23, 24]). An elementary example of this is the phase-plane analysis of traveling waves of the Fisher-KPP equation [25, 26] as described in [27]. This type of analysis has been very helpful in the study of steady-state solutions of spatially extended systems. Here, we go beyond this approach, and gain physical insight into the *global dynamics* of spatially extended systems from the analysis of geometric objects in phase space. Crucially, such a framework should be able to explain both, the dynamic process of pattern formation — initiated, for instance, by a lateral instability — as well as the final steady-state patterns in terms of the same concepts and principles.

While, in its full generality, this is likely a futile task, recent results for mass-conserving reaction–diffusion (McRD) systems have indicated ways in which progress can be made [28]. Based on numerical simulations, this study suggests a new way of thinking about pattern formation in terms of mass-redistribution and moving *local equilibria*: A dissection of space into (notional) local compartments allows us to characterize the spatiotemporal dynamics on the basis of the ODE phase space of local reactions. As (*globally* conserved) masses are spatially redistributed, the *local* masses in the compartments act as parameters for the reactive phase-space flow within them. The properties (position and stability) of the *local chemical equilibria* in the compartments are shown to depend on local masses and thus act as proxies for the local phase-space flow. (Please note that these chemical equilibria are not thermal equilibria but *non-equilibrium steady states* [30].) Diffusion acts to redistribute the conserved quantities between neighboring compartments and thereby induces changes in the local phase-space structure. This level of description proved to be very powerful in explaining chemical turbulence and transitions from chemical turbulence to long range order (standing and traveling waves) far from onset of the (subcritical) lateral instability. The prediction of chemical turbulence at onset, based on numerical simulations, was recently confirmed experimentally [31].

Hence, the advances in this “proof-of-principle” study suggest that a comprehensive theory of pattern formation in reaction–diffusion systems with conserved total densities (masses) can be developed based on the concept of mass-redistribution. Here, we present the basic concepts and mathematical framework of this theory, as exemplified by two-component reaction–diffusion systems. As our results encapsulate the principles underlying pattern formation in McRD systems and establish a range of canonical concepts, they will form the basis for future generalization towards systems with more components and more conserved quantities. Going beyond reaction–diffusion systems, we believe that a framework based on the redistribution of mass may be helpful in a broader context, since conserved quantities are inherent to many spatially extended systems, such as particle based active matter systems.

B. Summary of key results

In this paper, we present a comprehensive theory for two-component McRD systems in one spatial dimension. The central theme is the characterization of the spatiotemporal dynamics of such systems in the phase space of the reaction kinetics. This phase space is two-dimensional (i.e. a phase plane) in the case of two-component McRD systems. A key insight from our phase-space analysis, provided in Section III, will be how spatial variations in protein density give rise to spatially heterogeneous local chemical equilibria. The relationship between mass and chemical equilibria is represented geometrically as a line of chemical equilibria (*reactive nullcline*) in phase space. We show that this line of chemical equilibria is a central geometric object in phase space that organizes the spatiotemporal dynamics. Furthermore, we identify a one-parameter family of (one-dimensional) manifolds in phase space on which diffusive fluxes balance. Each steady-state pattern is embedded in one of these so-called *flux-balance subspaces*. The variable that parameterizes the family of flux-balance subspaces can be pictured as a non-equilibrium chemical potential (termed “*mass-redistribution potential*” because gradients within it drive mass-redistribution) that encapsulates the interplay between reactions and diffusion processes. In this way, the spatiotemporal dynamics of the reaction–diffusion system is fully determined by geometric structures in phase space. Importantly, all aspects of pattern formation ranging from linear instability (Sec. III D) and excitability (Sec. VI) to the characteristics (Sec. V) and bifurcations (Sec. VII) of patterns, can be extracted from the geometric features of the line of chemical equilibria and the flux-balance subspace. As an additional advantage of such a characterization, we note that the line of local equilibria could in principle be determined experimentally for any given system in which the average total density can be controlled in a well-mixed “reactor”.

In the following, we outline what we regard as the main advances and insights obtained from our framework:

- (i) A *flux-balance construction*, based on intersection points between flux-balance subspace and reactive nullcline (see Sec. III C), enables us to graphically construct stationary patterns and their complete bifurcation structure (see Sec. VII) in the limit of large system size. We also show how the concept of local equilibria underlying the framework reveals the physical basis of this graphical construction: patterns are *scaffolded* by local equilibria which are, in turn, encoded by the reactive nullcline.
- (ii) The principle of scaffolding by local equilibria can be generalized to dynamics. It reveals the core process underlying pattern formation in McRD systems — a mass-redistribution instability driven by shifting local equilibria and diffusive redistribution of mass (see Sec. III D). Based on this, we find that the slope and curvature of the nullcline provide simple criteria for the occurrence of lateral instability and whether the onset of instability is sub- or supercritical in systems with finite size (see Sec. VIII D).
- (iii) The concept of local compartments (and their local equilibria) can be generalized to spatial regions with respective regional attractors which are characterized by the average density within them (see Sec. V D). This concept of regions enables us to find simple heuristics for many properties of the pattern formation dynamics and steady-state patterns: The width of the interface region can be approximated by the marginal mode of the regional dispersion relation of the interface (see Sec. V A). On this basis, one can characterize different pattern types and the transitions between them as control parameters are changed (Sec. V B). Furthermore, the basin of attraction (“nucleation threshold”) for stationary patterns can be estimated by a simple heuristic using the reactive nullcline (Sec. VI).

Finally, we would like to highlight two key implications of our findings. First, our analysis shows that the onset of a mass-redistribution instability is generically subcritical (see Sec. VIII D). Second, we find an intrinsic connection between linear lateral instability and excitability via the concept of regional instability (see Sec. VI). Because these features are consequences of mass redistribution, we expect that they are not specific to two-component systems, but hold generically for McRD systems with more components.

C. Structure of the paper

We close this introductory section with a concise description of the logic and structure of our theoretical analysis in order to provide some guidance in reading the manuscript:

Section II briefly introduces two-component McRD systems. Such systems serve as a paradigmatic class of systems able to form (stationary) patterns. We give a literature overview of applications, most prominently cell polarization. Section III introduces the phase space and the basic geometric elements therein (Secs. III A and III B). These will allow us to characterize stationary patterns (via a “flux-balance construction”; Sec. III C) and the pattern-forming instability which we show is a *mass-redistribution instability* (Sec. III D). In Section IV, a system of two diffusively coupled, well-mixed compartments is used to illustrate the elementary aspects of pattern formation dynamics in McRD systems. This simple system allows us to study the details of the mass-redistribution instability (Sec. IV A). The two-compartment system also provides an intuitive picture of how the mass-redistribution cascade that drives lateral instability (i.e. the pattern-forming process) terminates by a balance of diffusive fluxes and reactive turnovers (*flux-turnover balance*, Sec. IV B).

Section V returns to the spatially continuous system and introduces the concept of spatial regions as a generalization of local compartments. Based on this, we provide a simple heuristic for the interface width (Sec. V A), characterize distinct pattern types in terms of the nullcline shape (Sec. V B), and construct the generic bifurcation diagram of stationary patterns under variation of the average total density (Sec. V C) by utilizing the flux-balance construction on the reactive nullcline.

In Section VI we use the concept of regions to show that linear instability and excitability are closely related and provide a simple heuristic based on the reactive nullcline to estimate the basin of attraction (“nucleation threshold”), of stationary patterns.

In Section VII we complete the bifurcation analysis for all control parameters (diffusion constants and kinetic rates in addition to the average total density). We show the generic bifurcation structures for monostable (Sec. VII A) and bistable (Sec. VII B) reaction kinetics in the limit of infinite system size, and characterize the transition between monostable and bistable regimes upon deformations of the reactive nullcline (cusp bifurcation, see Sec. VII C). We conclude our bifurcation analysis with a weakly nonlinear analysis in the vicinity of lateral stability onset, to study the transition from subcriticality to supercriticality in small systems (Sec. VII D).

Finally in Section VIII, we discuss the implications of our results in two broader contexts: reaction–diffusion systems, specifically in the context of protein pattern formation (Sec. VIII A), and non-equilibrium systems in general (Sec. VIII B). The outlook, Sec. VIII C outlines open questions, upcoming work, and avenues towards future generalizations of the mass-redistribution framework.

II. TWO-COMPONENT MASS-CONSERVING REACTION–DIFFUSION SYSTEMS

Our goal is to find geometric structures in phase space that allow the characterization of mass-conserving reaction–diffusion (McRD) systems. The simplest system of this type is a two-component reaction–diffusion system with two scalar densities, $m(x, t)$ and $c(x, t)$,

$$\partial_t m(x, t) = D_m \nabla_x^2 m + f(m, c), \quad (1a)$$

$$\partial_t c(x, t) = D_c \nabla_x^2 c - f(m, c), \quad (1b)$$

on a one-dimensional domain of length L with reflective (no-flux) boundary conditions $\nabla_x m|_{x=0, L} = 0$; all results can straightforwardly be generalized to periodic boundary conditions. The global average \bar{n} of total density $n(x, t) = m(x, t) + c(x, t)$ is conserved:

$$\bar{n} = \frac{1}{L} \int_0^L dx (m(x, t) + c(x, t)). \quad (1c)$$

We have chosen the above form for its conceptual simplicity. However, the principles that characterize pattern formation for this ‘minimal’ model can be generalized to more complex systems with more components and conserved species [28, 32–34]

Two-component systems of the above form have previously been studied as conceptual models for cell polarization [35–44], where Eq. (1) describes the dynamics of a protein species that cycles between membrane (slow diffusing, concentration $m(x, t)$) and cytosol (fast diffusing, concentration $c(x, t)$). In this biological context, the nonlinear kinetics term $f(m, c)$ is of the form

$$f_{\text{cell}}(m, c) = a(m)c - d(m)m, \quad (2)$$

where the non-negative terms $a(m)c$ and $d(m)m$ characterize the attachment of proteins from the cytosol to the membrane and the detachment back into the cytosol, respectively. This functional form of f_{cell} results from the fact that in intracellular systems chemical reactions are mainly restricted to the cell membrane. We will use kinetics of the form f_{cell} for illustration purposes; for specific examples we refer to Appendix A. Importantly however, our results hold for general kinetics f , and are not restricted to models for intracellular pattern formation.

Two-component McRD systems have also been studied for slime mold aggregation [45], cancer cell migration (glioma invasion) [46], precipitation patterns [47, 48], and simple contact processes [49, 50]. Furthermore, non-isothermal solidification models [51] can also be rewritten in the form Eq. (1); see e.g. Refs. [47, 52].

Finally we note that the classic Brusselator system [53], commonly used to study pattern formation, has a core of the form of Eq. (1) with additional linear terms that break mass conservation. These additional terms are not essential for the ability to form patterns in the first place. In fact, in Ref. [44] a mass-conserving variant of the Brusselator model is studied. In Refs. [54, 55]

the terms breaking mass conservation are set to a slow timescale.

The theory we develop in this paper holds generally for any reaction–diffusion system of the form Eq. (1), regardless of the particular underlying physics. Yet, for the sake of specificity, we use the notation and language of intracellular pattern formation. Throughout the paper, we will use (m, c) -phase-space plots to analyze the dynamics of the two-component system, Eq. (1). By convention, we plot the faster diffusing (e.g. cytosolic) species c on the vertical axis and the slower diffusing species m on the horizontal axis.

III. SETTING THE STAGE — GEOMETRIC STRUCTURES IN PHASE SPACE

In this section we will introduce the basic geometric concepts in phase space that we will later use for a full characterization of pattern formation, including pattern types, bifurcations, and the corresponding characteristic length and time scales. To this end, we will first study the spatially homogeneous (well-mixed) case where we can use the classical geometric tools for studying ordinary differential equations [1, 2, 5]. Subsequently, we will build on the phase-space structures obtained from the well-mixed case to also understand pattern formation in spatially extended systems in terms of flow in phase space.

A. Phase-space analysis of a well-mixed system

For a well-mixed system, the dynamics reduces to a set of ordinary differential equations

$$\partial_t m = f(m, c), \quad \partial_t c = -f(m, c). \quad (3)$$

Since the kinetic interactions conserve total density (protein mass), $\partial_t n = 0$, the reactive flow in (m, c) -phase space is restricted to the *reactive phase space* where $n = m + c$ is a constant of motion; see illustration in Fig. 1(a). The chemical reactions are balanced at the chemical equilibria (fixed points),

$$(m^*, c^*) : \begin{cases} f(m^*, c^*) = 0, \\ m^* + c^* = n, \end{cases} \quad (4)$$

which are given by the intersection points between the reactive *nullcline* (NC) (or ‘line of chemical equilibria’), $f(m^*, c^*) = 0$, and the reactive phase space for a given mass n . The *reactive flow* in the respective phase space is organized by the location and (linear) stability of these fixed points (which are both functions of n); see Fig. 1(a) and discussion below. By varying the total density n , i.e. by shifting the reactive phase space, one can construct a bifurcation diagram showing the chemical equilibrium $c^*(n)$ as a function of the total density n (Fig. 1(b)). The total density is a control parameter

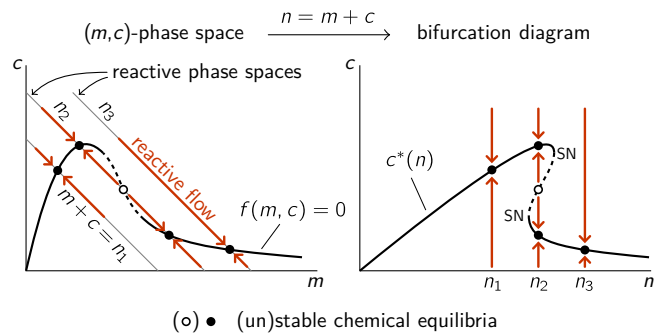


FIG. 1. Phase space and bifurcation structure of a well-mixed, mass-conserving two-component system. The total density n is a control parameter of mass-conserving reactions. The properties (number, position, and stability) of chemical equilibria depend on the total density (mass) in a well-mixed compartment. The conservation law $m + c = n$ is geometrically represented by 1-simplexes in phase space — each value of the total density corresponds to a unique 1-simplex. We refer to these subspaces as reactive phase spaces (local phase spaces in context of spatially extended systems). Local chemical reactions interconvert the conformational states of the proteins and hence change their densities, giving rise to a flow in phase space (red arrows) which, due to mass conservation, is confined to the reactive phase spaces. The flow vanishes along the *reactive nullcline* $f(m, c) = 0$ (black line) which is a line of chemical equilibria. Intersections of a reactive phase space with the reactive nullcline are chemical equilibria $(m^*(n), c^*(n))$ for a given total density n , shown as disks (\bullet, \circ) for three different values $n_{1,2,3}$. The (m, c) -phase space can be transformed into a bifurcation diagram $c^*(n)$ by the (skew) transformation $n = m + c$. Because of the conservation law, the well-mixed system has only one degree of freedom, so the only possible bifurcations are saddle-node bifurcations (SN) where the reactive nullcline is tangential to a reactive phase space. (In the presence of a symmetry or for fine-tuned parameters, there can also be a pitchfork bifurcation [1].)

of the chemical equilibria. When total density changes, the local equilibria will *shift*. These *shifting (or moving) local equilibria*, introduced in Ref. [28], are the key to understanding the mass-conserving reaction–diffusion dynamics as we will see repeatedly throughout this paper.

In each reactive phase space, we can eliminate (the cytosolic density) $c(t)$ and write the dynamics in terms of (the membrane density) $m(t)$ alone: $\partial_t m(t) = f(m(t), n - m(t))$; equally well $m(t)$ could be eliminated. In the vicinity of an equilibrium m^* the linearized reactive flow reads $\partial_t m(t) \approx (f_m - f_c)(m(t) - m^*)$, with $f_{m,c} := \partial_{m,c} f|_{(m^*, c^*)}$. We can read off the eigenvalue $\sigma_{\text{loc}}(n) := f_m - f_c$ for the local equilibrium and obtain to leading linear order in the vicinity of the reactive nullcline:

$$\begin{aligned} f(m, c) &\approx \sigma_{\text{loc}}(n) \cdot (m - m^*(n)) \\ &= -\sigma_{\text{loc}}(n) \cdot (c - c^*(n)). \end{aligned} \quad (5)$$

The sign of σ_{loc} — and thereby stability of the chemical equilibria — can be inferred from the slope of the reactive nullcline

$$\chi(n) := \partial_m c^*(m)|_n = -\frac{f_m}{f_c}\Big|_n. \quad (6)$$

For $f_c > 0$, which is always the case for attachment–detachment kinetics where $f_c = a(m)$, local equilibria are stable, $\sigma_{\text{loc}}(n) < 0$, if (and only if) the slope of the reactive nullcline is less steep than the slope of the reactive phase space:

$$\chi(n) = -f_m/f_c > -1. \quad (7)$$

Note that the local eigenvalue σ_{loc} can be rewritten as $\sigma_{\text{loc}} = f_c \cdot (-\chi - 1)$, which shows why the slope criterion, Eq. (7), for local stability is reversed for $f_c < 0$. Figure 1(a) shows an example for a reaction kinetics where the dynamics is monostable except for a window of protein masses exhibiting bistability with one unstable (\circ) and two stable fixed points (\bullet).

B. Stationary patterns are embedded in a flux-balance subspace of phase space

To apply the above approach to spatially extended systems, one has to understand the role of diffusive coupling. A standard approach would be to begin the analysis of the reaction–diffusion system by performing a linear stability analysis of the homogenous steady state(s). Because we are interested in the complete nonlinear dynamics underlying pattern formation, we choose a different route and study the non-trivial steady states (stationary patterns) first. The canonical linear stability analysis can be found in Appendix C. Later in this section (Sec. III D) and further in Sec. IV, we will elucidate the relation of lateral instability to phase-space geometry and discuss the underlying physical mechanism — a mass-redistribution instability.

A *stationary pattern* $\tilde{m}(x)$, $\tilde{c}(x)$ is solution to the set of steady-state equations,

$$D_m \nabla_x^2 \tilde{m} + f(\tilde{m}, \tilde{c}) = 0, \quad (8a)$$

$$D_c \nabla_x^2 \tilde{c} - f(\tilde{m}, \tilde{c}) = 0, \quad (8b)$$

under the constraint of a given average total density \bar{n} (Eq. (1c)). Figure 2(a) shows the sketch of a typical stationary pattern $\tilde{m}(x)$ (solid line) and the corresponding local equilibria $m^*(x)$ (black disks) obtained from a numerical solution of Eq. (8) with a reaction term e.g. as in Refs. [39, 44, 56] (see Appendix A). We study patterns with monotonic density profiles, which serve as elementary building blocks for more complex stationary patterns (see end of this section, and Section V). The example shown in Fig. 2(a) is a ‘mesa’ pattern exhibiting two plateau regions connected by an interface region with an inflection point of the concentration profile at x_0 .

Here we ask what can be learned about the steady-state pattern by applying geometric concepts in phase space alone, i.e. without relying on an explicit numerical solution. We start from the observation that Eq. (8) imply that in steady state the diffusive fluxes of m and c have to balance locally at each position x in the spatial domain $[0, L]$:

$$D_m \nabla_x \tilde{m}(x) = -D_c \nabla_x \tilde{c}(x). \quad (9)$$

This local *flux-balance condition* is obtained by adding the two steady-state equations, Eq. (8a) and Eq. (8b), integrating over x and employing no-flux boundary conditions. Integrating this relation once more from the boundary to any point x in the domain yields that any stationary pattern obeys the linear relation

$$\frac{D_m}{D_c} \tilde{m}(x) + \tilde{c}(x) = \eta_0, \quad (10)$$

where η_0 is a constant of integration. As we will show later in Section III C, the value of $\eta_0(\bar{n}, L)$, as a function of the global total density \bar{n} and the system size L , is determined by the balance of reactive processes. Equation (10) implies that any stationary pattern is confined to a linear subspace of the (m, c) -phase space; see Fig. 2(b). We shall call this subspace the *flux-balance subspace* (FBS), since it represents the local balance between the diffusive fluxes on the membrane and in the cytosol (Eq. (9)). The slope $(-D_m/D_c)$ of the flux-balance subspace is uniquely determined by the ratio of the diffusion constants. Consequentially and importantly, whenever the diffusion constants D_m and D_c are unequal, the flux-balance subspace cannot coincide with any reactive phase space (which has slope -1). Hence, any stationary pattern (non-uniform $\tilde{m}(x)$) is inextricably linked to a non-uniform total density profile $\tilde{n}(x) := \tilde{m}(x) + \tilde{c}(x)$. The *local total densities* $\tilde{n}(x)$ determine the *local (reactive) phase spaces* of the spatially extended system, which we will use in the following section to characterize the stationary pattern.

Equation (10) has been previously used to mathematically simplify the construction and analysis of stationary patterns in two-component systems, by introducing the new phase-space coordinate (orthogonal to the flux-balance subspace)

$$\eta := \frac{D_m}{D_c} m + c, \quad (11)$$

and describing the spatiotemporal dynamics in terms of the scalar fields $n(x, t)$ and $\eta(x, t)$ (cf. Refs. [36, 44]). The physical origin (diffusive flux balance) and the geometric interpretation (flux-balance subspace) discussed above explains why Eq. (10) has proven to be useful before (and why it will be useful in our further analysis). In particular, note that by adding Eqs. (1a) and (1b) one finds that gradients in $\eta(x, t)$ drive mass redistribution:

$$\partial_t n(x, t) = D_c \nabla_x^2 \eta(x, t). \quad (12)$$

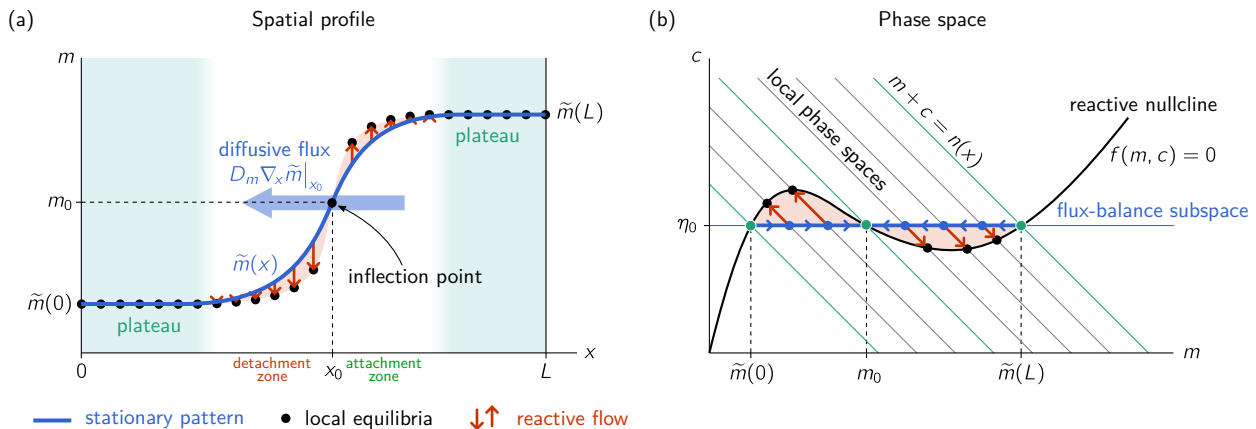


FIG. 2. Illustration of a stationary pattern and its embedding in phase space which motivates our flux-balance construction on the reactive nullcline. (See Movie 1 in the Supplementary Material for a visualization of the dynamics that lead to such a steady state pattern). (a) Local chemical equilibria m_x^* (\bullet) scaffold the pattern profile due to the local reactive flow towards the local equilibria (red arrows). At the inflection point x_0 the flux-balance subspace intersects the reactive nullcline $\tilde{f}(m(x_0), \eta_0) = 0$. In a steady state, the diffusive flux across the inflection point blue arrow exactly cancels the cumulative reactive turnover on either side of the inflection point (indicated by red shaded areas). (b) The stationary pattern is embedded in phase space (thick blue line) and is embedded in a flux-balance subspace (thin blue line). The local reactive flows (red arrows) are restricted to the local phase spaces where total density is conserved locally. The intersections between the local phase spaces and the reactive nullcline $f(m, c) = 0$ yield the local equilibria (\bullet). Slow membrane diffusion (blue arrows) balances the reactive flows towards the equilibria in the vicinity of x_0 (see Sec. IV B for a detailed discussion of this *flux-turnover balance*). The regions left and right of x_0 can be intuitively characterized as attachment and detachment zones based on the direction of the reactive flow in them (cf. Fig. 4). A balance of total turnovers (red shaded areas between pattern and local equilibria in (a) and (b)) determines η_0 (cf. Eq. (19)). (For visual clarity, we show a schematic pattern profile and phase-space picture for the case $D_m \ll D_c$, based on graphs from numerical data. See Fig. 18 in Appendix A for the original plots produced directly from a numerical simulation of Eq. (1).)

We will therefore call $\eta(x, t)$ the *mass-redistribution potential*. (One may picture it to play the role of a non-equilibrium chemical potential.) When we substitute c using η , the reaction term reads

$$\tilde{f}(m, \eta) := f(m, \eta - m D_m / D_c), \quad (13)$$

and the stationarity conditions, Eqs. (8a) and (8b), are replaced by

$$D_m \nabla_x^2 \tilde{m} + \tilde{f}(\tilde{m}, \tilde{\eta}) = 0, \quad (14a)$$

$$D_c \nabla_x^2 \tilde{\eta} = 0. \quad (14b)$$

From the second equation, we recover that in steady state, the mass-redistribution potential must be constant in space, $\tilde{\eta} = \eta_0$, (on a domain with no-flux or periodic boundary conditions). The mass-redistribution potential plays a role analogous to the chemical potential in Model B dynamics. However, it does not follow from a free energy density. Instead, it is determined by the local concentrations via Eq. (11), so the mass redistribution dynamics Eq. (12) is not closed. Later, in Sec. III D, we will introduce an approximate “closure relation” for Eq. (12).

The above analysis can be generalized along various lines: In systems with N components of one conserved species, the flux-balance subspace in N -dimensional phase space is a $N - 1$ dimensional hyperplane, orthogonal to the vector of diffusion constants

$(D_1, D_2, \dots, D_N)^T$. For systems with spatial dimension larger than one, Eq. (14b), which holds in any spatial dimension, can be used to construct the flux-balance subspace. This implies that $\tilde{\eta} = \eta_0$ must be constant in space for stationary patterns in any spatial dimension.

As consequence of the flux-balance condition, one can conclude that extrema of the concentrations $\tilde{m}(x)$ and $\tilde{c}(x)$ have to coincide in space for any stationary pattern. Therefore, any non-monotonic stationary pattern can be dissected at its extrema by inserting no-flux boundaries. In that sense, monotonic patterns are the elementary building blocks of composite non-monotonic patterns.

C. Stationary patterns are scaffolded by local equilibria

The spatially inhomogeneous total density profile $\tilde{n}(x)$ of a stationary pattern is key to understanding the relationship between the stationary pattern $(\tilde{m}(x), \tilde{c}(x))$ and the reactive nullcline $(m^*(n), c^*(n))$. Consider the system as being spatially dissected into notional *local* compartments, an approach introduced in Ref. [28]. Within each such compartment, local kinetic interactions induce a reactive flow $f(m, c)$ that lies in the *local phase space* $((m, c) : m + c = \tilde{n}(x))$ which is determined by the respective local mass $\tilde{n}(x)$. The *local (chemical) equilibria*

where the kinetic interactions within a compartment balance depend on the local total density $\tilde{n}(x)$ in the compartment

$$(m_x^*, c_x^*) : f(m_x^*, c_x^*) = 0 \text{ for } m_x^* + c_x^* = \tilde{n}(x), \quad (15)$$

where we use the abbreviation $m_x^* := m^*(n(x))$, and analogously for c_x^* . Recall that the local chemical equilibria are geometrically determined by intersection points of the local reactive phase with the reactive nullcline. The local equilibria together with their linear stability serve as proxies for the local reactive flow (as in the well-mixed system discussed in the section III A; cf. Eq. (5)). Thereby, compartmentalization extends the phase-space structure of the local kinetic interactions to the spatially extended system (Fig. 2(b)).

The N-shape of the reactive nullcline shown in Fig. 2(b) is one of two prototypical nullcline shapes exhibited by all two-component McRD models mentioned in Sec. II. The other prototypical shape is only subtly different in its behavior for large m where instead of bending back up it continues to approach the m -axis monotonically (see Fig. 19 in Appendix A). This second nullcline shape is ‘hump’-shaped and can give rise to ‘peak’-patterns as we will discuss later in Sec. V B.

1. The flux-balance construction on the reactive nullcline

What is the relation between the local equilibria (m_x^*, c_x^*) and the stationary pattern $(\tilde{m}(x), \tilde{c}(x))$? To gain some intuition, let us consider the following *gedanken-experiment* (cf. [28]): Dissect a given pattern into small spatial compartments and shut off diffusive coupling between them. Then each (well-mixed) compartment will relax to the chemical equilibrium (black disks) determined by the total density $\tilde{n}(x)$ in each of the compartments, cf. Fig. 2(a). In that sense, the local equilibria act as a scaffold for the pattern. Because total density must be conserved individually in each of the (now uncoupled) compartments the approach (red arrows) to the local equilibria is confined to the reactive phase space (gray lines) given by the total density in the compartment.

Let us now consider diffusive coupling between these compartments. In steady state, the *net* diffusive flux in and out of the compartment is balanced by the deviation from local equilibrium (it is instructive to compare Eq. (4) for chemical equilibria and Eqs. (8) for stationary pattern). If the gradient does not change across the compartment, such that the flux into and out of the compartment are identical, the net diffusive flux vanishes: $\nabla_x [D_m \nabla_x \tilde{m}(x)] = 0$. In turn, the stationary pattern must coincide with the local chemical equilibria: $\tilde{m}(x) = m_x^*$ and $\tilde{c}(x) = c_x^*$, when the gradient does not change across a compartment. This holds exactly at *inflection points* of the pattern. For *plateaus*, the gradient is small, $\nabla_x \tilde{m}(x) \approx 0$, in a spatially extended region, and so is the local net flux, i.e. $\nabla_x^2 \tilde{m}(x) \approx 0$. Hence, for

plateaus we have $f(\tilde{m}(x), \tilde{c}(x)) \approx 0$, such that the pattern can be locally approximated by the respective local chemical equilibria, i.e. $\tilde{m}(x) \approx m_x^*$ and $\tilde{c}(x) \approx c_x^*$ in plateau regions. Since the reactive flow is linear in the vicinity of local equilibrium (cf. Eq. (18)), the deviation from local equilibrium is proportional to the small local net diffusive flux.

Because local equilibria are represented by the reactive nullcline while the stationary pattern must be embedded in a flux-balance subspace, we can identify plateaus and the inflection point as intersection points of flux-balance subspace and nullcline (FBS–NC intersections) in phase space. As illustrated in Fig. 2, these ‘*landmark points*’ in phase space enable us to graphically construct the spatial patterns in real space as two plateaus connected by an interface (*flux-balance construction*).

Near the interface the densities $\tilde{m}(x)$ and $\tilde{c}(x)$ (of a stationary pattern) will deviate from the corresponding local chemical equilibria. The ensuing reactive flows (red arrows) left and right of the inflection point are of opposite sign and correspond to attachment and detachment zones for protein patterns (see Fig. 2(a)) [57]. In total, these reactive flows have to cancel because there cannot be a *net* reactive turnover in steady state. This *total turnover balance* determines the FBS-position η_0 as we will see in the next section. In particular, we will show that total turnover balance approximately corresponds to a balance of the areas between FBS and NC in phase space (red shaded areas in Fig. 2(b)), reminiscent of a Maxwell construction.

Building on the above geometric characterization we will later in Sec. V analyze the phase-space structure in the vicinity of landmark points (plateaus and inflection points) by linearizing the phase-space flow around them. This will enable us to further quantify the spatial profile of stationary patterns, i.e. to determine the relevant length scales.

2. Turnover balance determines η_0

Integrating one of the stationarity conditions, Eq. (8a), over the whole spatial domain $[0, L]$ yields that in steady state the total reactive turnover must vanish

$$\int_0^L dx \tilde{f}(\tilde{m}(x), \eta_0) = 0. \quad (16)$$

This *total turnover balance* determines the position η_0 of the flux-balance subspace in steady state. A mathematically more convenient form of turnover balance is obtained by multiplying Eq. (8a) with $\partial_x \tilde{m}(x)$ before integrating:

$$\int_{\tilde{m}(0)}^{\tilde{m}(L)} dm \tilde{f}(m, \eta_0) = 0. \quad (17)$$

In this form, it becomes evident that the total turnover balance does not depend on the full density profile $\tilde{m}(x)$,

but only on the densities at the boundaries, $\tilde{m}(0)$ and $\tilde{m}(L)$. Total turnover balance, Eq. (17), together with the stationarity condition for $\tilde{m}(x)$, Eq. (14a), fully determine the stationary patterns.

Geometrically, total turnover balance can be interpreted as a kind of (approximate) Maxwell construction (balance of areas) in (m, c) -phase space, under the following approximations: First, we linearize the reactive flow around the reactive nullcline (cf. Eq. (5)):

$$f(m(x), c(x)) \approx \sigma_{\text{loc}}(\tilde{n}(x)) \cdot (m(x) - m_x^*). \quad (18)$$

Further, suppose for the moment that the local eigenvalue $\sigma_{\text{loc}}(n(x))$ is approximately constant in the range of total densities attained by the pattern. Turnover balance, Eq. (17), is then represented by a balance of the areas between nullcline and flux-balance subspace on either side of the inflection point (see areas shaded in red (light gray) in Fig. 2(b)):

$$\int_{\tilde{m}(0)}^{\tilde{m}(L)} dm [m - m^*(\tilde{n}(m))] = 0, \quad (19)$$

where we used the relation

$$\tilde{n}(m) := m + \eta_0 - \frac{D_m}{D_c} m \quad (20)$$

for the total density in steady state. The expression in the square brackets of Eq. 19 is simply the distance of the reactive nullcline from the flux-balance subspace measured along the respective local phase space. The integral over this distance is the area between the flux-balance subspace (FBS) and the reactive nullcline (NC).

In the characterization of pattern profiles in Sec. V below, we will use that for a spatial domain size L much larger than the interface width, we can approximate the plateau concentrations by FBS-NC intersections: $\tilde{m}(0) \approx m_-(\eta_0)$ and $\tilde{m}(L) \approx m_+(\eta_0)$. In this case, Eq. (17) is closed and can be solved for η_0 , either numerically or geometrically using the approximate ‘Maxwell construction’, Eq. (19).

We close this section with a side remark on what is sometimes called the method of ‘Newton mapping’ or ‘rolling ball analogy’. Here one maps the second order differential equation, Eq. (14a), describing the stationary front in space to the equation of motion of a point-like particle moving between two ‘hilltops’ in a potential energy landscape; see e.g. Ref. [3]. The corresponding mechanical potential is given by $V(m) = -\int dm f$, and the total turnover balance condition maps to an equal height condition, $V(\tilde{m}(0)) = V(\tilde{m}(L))$, at the ‘position’ \tilde{m} of the particle at ‘times’ 0 and L . While such an approach may sometimes be mathematically instructive, we would like to emphasize the role of the actual physical processes and phase-space geometry in this paper.

3. Summary of geometric structures in phase space

Let us pause for a moment and briefly summarize our findings so far. We have established three major geometric structures in (m, c) -phase space: First, the *reactive nullcline*, $f(m, c) = 0$, along which the local kinetic interactions are balanced; second, the *local phase spaces*, $m + c = \tilde{n}(x)$, determined by the local total densities $\tilde{n}(x)$ — local equilibria (m_x^*, c_x^*) are intersections of the reactive nullcline and the local phase spaces; third, the family of *flux-balance subspaces*, within which diffusive flows in membrane and cytosol balance each other. The position of the flux-balance subspace, η_0 , of a stationary pattern is determined by total turnover balance, Eq. (17), which represents a balance of reactive processes.

This geometric picture underlies the key results we present in the remainder of the paper. Up to now, we have only discussed the embedding of the pattern in the (m, c) -phase space. To study the possible pattern profile shapes $\tilde{m}(x)$ in real space, we need to understand the dynamic process of pattern formation, in particular the factors determining the interface region. As we will see below (Sec. V), the interface of a pattern is inextricably connected to lateral instability. We will therefore first analyze lateral instability and the dynamic process of pattern formation in the following section. With these tools at hand, we will then be able to characterize the distinct pattern types exhibited by two-component McRD systems.

D. Lateral instability

How can the geometric structures introduced in the previous section help us to understand the physical process of pattern formation? Previous research [28] suggests that the total densities are the essential degrees of freedom and their redistribution is the key dynamic process. Building on this insight, we now systematically connect the pattern formation dynamics – in particular lateral instability – to the geometric structures established above (Sec. III).

1. Mass redistribution instability

The intimate connection between shifted local equilibria and the stationary pattern (cf. Fig. 2) suggests that mass redistribution and moving local equilibria are all one needs to describe the core dynamics of pattern formation. Consider the dynamics of the local total density $n(x, t) = c(x, t) + m(x, t)$. Because the kinetics conserve local total density, the time evolution of $n(x, t)$ is driven only by diffusion due to spatial gradients in the concentrations $c(x, t)$ and $m(x, t)$:

$$\partial_t n(x, t) = D_c \nabla_x^2 c(x, t) + D_m \nabla_x^2 m(x, t). \quad (21)$$

As a result of mass redistribution, the local equilibria $\{c^*(n(x,t)), m^*(n(x,t))\}$ change. In turn, these shifted equilibria induce changes in the local reactive fluxes and thereby altered spatial gradients in $c(x,t)$ and $m(x,t)$. This intricate coupling between redistribution of total mass, reactive flows, and diffusive flows drives pattern formation.

Qualitatively, one may capture the essence of this coupling between reactive and diffusive flow by the observation that the dynamics depend mainly on the direction in which the local equilibria shift due to increasing or decreasing local total density. Let us therefore posit that the relevant diffusive gradients can be (qualitatively) estimated by replacing the local concentrations by the (locally stable) local equilibrium:

$$c(x,t) \rightarrow c^*(n(x,t)), \quad m(x,t) \rightarrow m^*(n(x,t)), \quad (22)$$

such that local mass $n(x,t)$ is the only remaining degree of freedom:

$$\partial_t n(x,t) \approx D_c \nabla_x^2 c^*(n) + D_m \nabla_x^2 m^*(n). \quad (23)$$

Using the chain rule, we can rewrite the mass redistribution dynamics as

$$\partial_t n(x,t) \approx \nabla_x \cdot [(D_c \partial_n c^* + D_m \partial_n m^*) \nabla_x n] \quad (24)$$

which is simply a diffusion equation for the total density $n(x,t)$. The effective diffusion constant will become negative (which entails anti-diffusion) if

$$\frac{\partial_n c^*}{\partial_n m^*} = \chi(n) = -\frac{f_m}{f_c} < -\frac{D_m}{D_c}, \quad (25)$$

where $\chi(n) = \partial_m c^*(m)|_n$ is the slope of the reactive nullcline $c^*(m)$ (cf. Eq. (6) in Sec. III A; remember that we assume $f_c > 0$, for f_c the inequality Eq. (25) is reversed). Starting from a homogenous steady state $(m^*(\bar{n}), c^*(\bar{n}))$, *lateral instability* due to effective anti-diffusion occur if

$$\chi(\bar{n}) < -\frac{D_m}{D_c}. \quad (26)$$

Geometrically this condition means that a spatially homogeneous steady state is laterally unstable if (and only if) the slope of the nullcline is steeper than the slope of the flux-balance subspace. Note that anti-diffusion will amplify perturbations on arbitrarily small lengths scales, as Eq. (23) does not have any intrinsic length scale. Therefore, Eq. (24) is no longer well-behaved on a continuous domain when there is lateral instability; for a more detailed discussion see Appendix D.

Let us compare this instability criterion to ‘classical’ linear stability analysis of Eq. (1) around the homogenous steady state (see Appendix C). There one obtains the dispersion relation $\sigma(q)$ for the growth rate σ of a mode with wavenumber q (see Fig. 3). It exhibits a band of unstable modes, $\sigma(q) > 0$ for $0 < q < q_{\max}$, with

$$q_{\max}^2 := \frac{f_m}{D_m} - \frac{f_c}{D_c} = \frac{\tilde{f}_m}{D_m} \quad (27)$$

if and only if $f_m/D_m > f_c/D_c$, i.e. precisely when the slope criterion, Eq. (25), is fulfilled. Equation (27) can be rewritten as $q_{\max}^2 = f_c/D_m(-\chi - D_m/D_c)$, which shows why the slope criterion Eq. (25) is reversed for $f_c < 0$.

One might be surprised that the ad hoc ‘approximation,’ Eq. (22), yields the exact onset criterion for lateral instability, Eq. (25). Before we discuss the mathematical reason for this in the next paragraph, let us briefly outline the central implications of the effective mass redistribution dynamics, Eq. (24), and the corresponding instability criterion, Eq. (25), for the rest of this paper:

(i) The lateral instability in two-component McRD systems is effective anti-diffusion (‘diffusion backwards in time’) of total density, meaning that spatial perturbations are amplified. Hence, mass redistribution is the underlying physical process of lateral instability which is therefore a *mass redistribution instability* (MRI).

(ii) MRI in reaction–diffusion systems is a Turing instability [58]. We will refer to the bifurcation where a homogeneous steady state becomes laterally unstable (i.e. Turing unstable), as *Turing bifurcation* [59].

(iii) The criterion for the Turing bifurcation (onset of lateral instability), Eq. (25), has a simple geometric interpretation in (m, c) -phase space: the slope of the nullcline $\chi(\bar{n}) = -f_m/f_c|_{\bar{n}}$ (cf. Eq. (6)) at the homogenous equilibrium $(m^*(\bar{n}), c^*(\bar{n}))$ has to be steeper than the slope of the flux-balance subspace $-D_m/D_c$ (recall that we found a similar slope-criterion for local stability, in Sec. III A). In flux-balance coordinates the criterion for lateral instability (existence of a band of unstable modes to be precise) simply reads $\tilde{f}_m > 0$ (cf. Eq. (27)).

(iv) Cytosolic diffusion is the transport process driving the mass-redistribution instability. To study the physical principle underlying this instability, we can neglect membrane diffusion and consider the limit $D_m \ll D_c$. The linearization of Eq. (24) for $n(x,t) = \bar{n} + \delta n(x,t)$ then reduces to a simple diffusion equation

$$\partial_t \delta n(x,t) \approx (\partial_n c^*|_{\bar{n}}) \cdot D_c \nabla_x^2 \delta n. \quad (28)$$

Hence, local equilibria that shift under redistribution of mass are the underlying reason for effective anti-diffusion (negative effective diffusion constant) which takes place when $\partial_n c^*|_{\bar{n}} < 0$ (or equivalently $\partial_m c^*(m)|_{\bar{n}} < 0$ [60]).

(v) Anticipating results we will obtain later in a detailed discussion of MRI and the role of membrane diffusion (Sec. IV A), we note that re-stabilization (of the MRI) at short length scales, $q > q_{\max}$, is a consequence of membrane diffusion and the finite rate of reactive processes (local chemical relaxation

to local equilibrium). Importantly, in Sec. V A, we will also show that $q_{\max}(n(x_0))$, at the pattern inflection point x_0 , determines the width of the interface.

(vi) The mass-redistribution instability is generically subcritical. To obtain a supercritical bifurcation the mass-redistribution cascade must be stopped by the counteracting membrane diffusion immediately after the onset of pattern growth. This requires fine-tuning, such that cytosolic transport due to shifting local equilibria just barely dominates at the onset of instability. We will analyze and discuss sub- vs. supercriticality in Sec. VII D.

(vii) In the vicinity of onset, the dispersion relation has a universal form (see Appendix C:

$$\begin{aligned}\sigma_q^{(2)} &\approx \frac{D_m D_c}{-\sigma_{\text{loc}}} q^2 (q_{\max}^2 - q^2) \\ &= -D_{\text{eff}} q^2 - \frac{D_m D_c}{-\sigma_{\text{loc}}} q^4,\end{aligned}\quad (29)$$

where $D_{\text{eff}} = D_c \partial_n c^* + D_m \partial_n m^*$ is the effective diffusion constant in the adiabatic scaffolding (long wavelength) limit. D_{eff} is negative in the laterally unstable case (anti-diffusion). Interestingly, the dispersion relation in the vicinity of onset, Eq. (29), has the same form as the one of Model B [61]. Hence, the linear dynamics close to onset are effectively described by Model B. Preliminary analytic results point toward the possibility of a systematic (approximate) mapping of the entire *non-linear* two-component McRD dynamics to Model B (*work in progress* [32]).

Finally, we note that the mass-redistribution dynamics, Eq. (24), can be rewritten most compactly using the mass-redistribution potential η , (cf. Eq. (12)):

$$\partial_t n(x, t) \approx D_c \nabla_x \cdot [\partial_n \eta^*(n) \nabla_x n]. \quad (30)$$

From this, it follows that a mass redistribution instability takes place if an increase in total density entails a decrease of the mass redistribution potential (i.e. $\partial_n \eta^*|_{\bar{n}} < 0$).

2. Scaffolding can be generalized beyond the adiabatic limit

On sufficiently large length scales, diffusive relaxation (transfer of mass) is slow compared to chemical relaxation, such that the approximation Eq. (22) which we call *adiabatic scaffolding* becomes exact — the concentrations are *slaved* to the local equilibria. Thus, any long wavelength instability in a McRD system can be exactly described in the asymptotic limit of adiabatic scaffolding. In the dispersion relation $\sigma(q)$ (see Fig. 3(b)), this type of instability is characterized by a band of unstable modes that extends down to long wavelength

($q \rightarrow 0$) (this case is called ‘type II’ instability in the Cross–Hohenberg classification scheme [62]). Because two-component McRD systems always have a long wavelength instability (‘type II’) at onset, we obtained the exact criterion for onset of lateral instability Eq. (25) via the adiabatic scaffolding limit. However, scaffolding as a physical concept provides insight into the spatial dynamics of systems also without this limit: In a five-component McRD model for *in vitro* Min patterns, the concept of scaffolding allowed to predict the transition to chaos (qualitative change of the local attractors from stable fixed point to limit cycle) [28]. In this system, the onset of lateral instability is not a long wavelength instability but takes place for a band of unstable modes bounded away from $q = 0$, corresponding to ‘type I’ instability in the Cross–Hohenberg classification scheme.

For two-component McRD systems, we will show below (Sec. IV A) that there is a *reaction-limited* regime, corresponding to short wavelengths, complementary to the *diffusion-limited* long wavelength regime. In the reaction-limited regime, just as in the five-component model studied Ref. [28], the concentrations are not slaved to the local equilibria. Nonetheless, scaffolding facilitates a *quantitative* understanding of the dynamics because local equilibria serve as *proxies* for local reactive flow.

One may compare the adiabatic scaffolding limit to the approach used to analyze limit cycle attractors of relaxation oscillators. There the N-shaped nullcline allows an analytic construction of the limit cycle in the asymptotic timescale separation limit. However, the qualitative phase-space structure that underlies the oscillations can also be deduced from the nullcline shapes without the timescale separation. In both cases, adiabatic scaffolding and the relaxation oscillator, treating the timescale separation in a mathematically rigorous way requires singular perturbation theory (see Appendix D).

Adiabatic scaffolding can also be understood as a closure relation. In that picture, $n(x, t)$ corresponds to a ‘coarse-grained order parameter’ with the microscopically correct dynamics given by Eq. (21). This equation is not closed, because $m(x, t)$ and $c(x, t)$ are not known. Adiabatic scaffolding, Eq. (22), is a closure for Eq. (21) at the price of losing the ‘microscopic’ length scale. One could try construct higher order closures that also take into account deviations from the local equilibria.

IV. TWO DIFFUSIVELY COUPLED COMPARTMENTS

The above analysis shows that the mass-redistribution instability does not require an interplay of two length scales (other than the instability in activator–inhibitor, systems which are driven by short range self-catalytic production and long range inhibition by degradation). Instead, the key physical process is simply the diffusive redistribution of mass, as the adiabatic scaffolding limit demonstrates (cf. Eq. (24)). This suggests that the time

evolution of the pattern-forming process and its termination in a stationary pattern can be studied in a simplified system with two well-mixed ‘compartments’ coupled by diffusion; see Fig. 3. Physically, the two-compartment system represents the elementary feature of any pattern — an interface — as illustrated by Fig. 3(a). In this section, we will use this two-compartment system to study mass-redistribution instability in detail.

Consider two well-mixed compartments with chemical concentrations denoted by $\mathbf{u}_{1,2}$, where $\mathbf{u}_i := (m_i, c_i)$. The kinetic interactions $\mathbf{f} := (f, -f)$ conserve the local total density (mass) $n_i = m_i + c_i$ in each compartment $i = \{1, 2\}$. Mass is exchanged between the compartments by a diffusive exchange process that acts to remove concentration differences. Correspondingly we have the coupled compartment dynamics

$$\begin{aligned}\partial_t \mathbf{u}_1 &= \hat{\mathcal{D}}(\mathbf{u}_2 - \mathbf{u}_1) + \mathbf{f}(\mathbf{u}_1), \\ \partial_t \mathbf{u}_2 &= \hat{\mathcal{D}}(\mathbf{u}_1 - \mathbf{u}_2) + \mathbf{f}(\mathbf{u}_2),\end{aligned}\quad (31)$$

conserving average total density $\bar{n} = (n_1 + n_2)/2$. We relate the (diffusive) exchange rates $\mathcal{D}_{m,c}$ to the diffusion constants $D_{m,c}$ via

$$\hat{\mathcal{D}} = \text{diag}(\mathcal{D}_m, \mathcal{D}_c) = \frac{\pi^2}{2L^2} \text{diag}(D_m, D_c). \quad (32)$$

For this choice of exchange rates, the linearization of Eq. (31) is identical to the linearization of the spatially continuous dynamics, Eq. (1), for a Fourier mode $\sim \cos qx$ with $q = \pi/L$; see Appendix C. (The factor 2 in the denominator originates from the linearization of the exchange terms in Eq. (31).) In this linear approximation, the two-compartment dynamics therefore exactly represents the dynamics of a single mode $q = \pi/L$ in the spatially continuous system, and one can use the system size L as a bifurcation parameter to sample the whole dispersion relation $\sigma(q = \pi/L)$; see Fig. 3(b).

As the pattern amplitude grows, nonlinearities will lead to mode coupling in a spatially continuous system. This is not captured by the two-component system which only describes the dynamics at one length scale. Nonetheless, we can gain a qualitative understanding of the full nonlinear pattern formation process, including the termination of mass-redistribution in a stationary pattern. Later in Sec. V we will study spatially continuous systems in terms of spatial *regions* instead of nonlinearly coupled modes.

A. Mass-redistribution instability is a generic physical principle

We have already learned that the lateral instability is a mass-redistribution instability driven by shifting local equilibria and cytosolic redistribution (cf. Eq. (28)). Specifically, the instability in the two-component McRD system always is a long wavelength instability, where the

timescales of chemical relaxation and diffusive redistribution are separated (adiabatic scaffolding).

In the adiabatic scaffolding limit, we found that the MRI is effective anti-diffusion of total density; cf. Eq. (28). This might seem counterintuitive at first, since the individual components diffuse ‘normally’. To resolve this apparent conundrum it is key to understand that the gradients which induce diffusive flows are established by shifting equilibria. For illustration purposes let us neglect membrane diffusion for now ($D_m = 0$). Following a small (random) perturbation which redistributes mass δn from one compartment to the other, the chemical equilibria in both compartments shift. Now recall that for a MRI the slope of the reactive nullcline needs to be negative. In this case, the equilibrium shifts to lower cytosolic concentration $c^*(n)$ as total density n is increased; for an illustration please refer to Fig. 3(c). In other words, in the compartment with a higher total density, there will be a reactive flow towards the membrane (red arrows) as the shifted local equilibrium is approached — thus creating a cytosolic sink. Conversely, the compartment with lower total density becomes a cytosolic source, and a gradient δc builds up. Mass redistribution ($\partial_t \delta n$, illustrated by purple arrows) due to the ensuing diffusive flux in the cytosol $D_c \delta c$ will further shift the equilibria, thus sustaining and amplifying the diffusive flux — the cycle feeds itself. We conclude that the *mass-redistribution instability is a self-amplifying mass redistribution cascade*. In contrast, when the cytosolic equilibrium density rises due to an increase in total density (i.e. for positive nullcline slope $\partial_n c^*|_{\bar{n}} > 0$) the compartment with more total density will become cytosolic source inducing mass redistribution that brings the system back to a homogenous state.

1. Reaction- and diffusion-limited regimes of the mass-redistribution instability

As we have just seen, the direction in which the equilibria shift determines the orientation of the cytosolic gradient, and therefore yields the criterion for the onset of lateral instability. A key characteristic of any instability is the growth rate of perturbations around the unstable steady state. How is the growth rate of the pattern-forming MRI determined from the interplay of diffusive and reactive fluxes?

In linear approximation for small perturbations $\delta n = n_2 - n_1, \delta c = c_2 - c_1$, the rate of change of c can be rewritten as $-\sigma_{\text{loc}} \cdot (\delta c - \delta c^*)$ (cf. Eq. (5)). The shift δc^* of local equilibria along the (linearized) reactive nullcline due to redistribution of mass δn is given by $\delta c^* = \partial_n c^*|_{\bar{n}} \cdot \delta n$. Together with the cytosolic flow redistributing total density, $\partial_t \delta n \approx D_c \delta c$, we obtain the linearized dynamics (still for $D_m = 0$),

$$\partial_t \delta n(t) = -D_c \delta c, \quad (33a)$$

$$\partial_t \delta c(t) = -D_c \delta c + \sigma_{\text{loc}} \cdot (\delta c - c^*|_{\bar{n}} \delta n), \quad (33b)$$

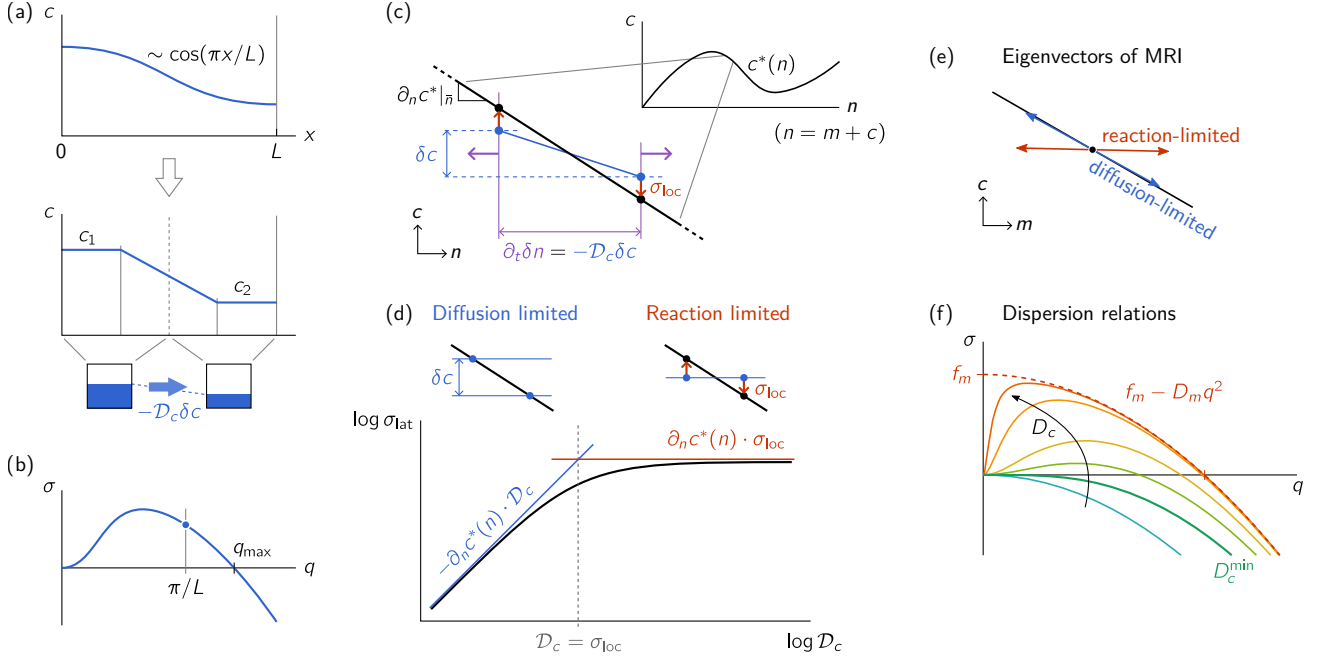


FIG. 3. Linear stability analysis of two diffusively coupled compartments. (a) The dynamics of the longest wavelength mode in a spatially continuous system with reflective boundaries can be matched (in the linear regime) by two compartments coupled by diffusive exchange. (b) By varying the system size, one can sample the full dispersion relation of the spatially continuous system (blue line). The bifurcation to lateral instability happens at $L_{\min} = \pi/q_{\max}$ (cf. Eq. (27)). (c) Lateral instability in (n, c) -phase space (i.e. the ‘bifurcation structure’ where the reactive nullcline appears as $c^*(n)$, cf. Fig. 1) is caused by a negative nullcline slope. Local chemical equilibria (●) shift due to mass redistribution (δn). Locally concentrations approach the local equilibria as a result of chemical relaxation (red arrows) – building up a gradient δc that induces further mass redistribution (purple arrows). (d) The growth rate of the instability depends on the timescale of cytosolic diffusion $\mathcal{D}_c \sim D_c/L^2$, the rate of chemical relaxation σ_{loc} , and the rate at which the equilibria shift due to mass redistribution $\partial_n c^*|_{\bar{n}}$. For slow diffusion, the concentrations are locally slaved to the equilibrium, such that the instability is diffusion limited. For fast diffusion, cytosolic gradients are homogenized quickly such that the limiting timescale is the approach of shifting equilibria which generates the cytosolic gradient. (e) Eigenvectors of mass-redistribution instability in the reaction-limited (red arrow) and diffusion-limited regime (blue arrow). In the former case, the cytosolic gradient is small compared to the membrane gradient, in the latter case the eigenvector is “slaved” to the reactive nullcline. (f) Dispersion relations for a range of $D_c/D_m = 1, 2, 4, 10, 100, 1000$, for a nullcline slope of $\chi = -1/2$ (up to the timescale $|\sigma_{\text{loc}}|^{-1}$ and the length scale $\sqrt{D_m/|\sigma_{\text{loc}}|}$, the shape of the dispersion relation is fully determined by $\chi(\bar{n})$, D_c/D_m , and the sign of σ_{loc}). The Turing bifurcation takes place at $D_c^{\min} = -D_m/\chi$ (thick green line). The dashed red line marks the reaction-limited growth rate $f_m - D_m q^2$ which is approached for wavenumbers $q \gg \sqrt{|\sigma_{\text{loc}}|/D_c}$, far away from onset (cf. Fig. 21 in Appendix C).

with the corresponding Jacobian

$$\begin{pmatrix} 0 & -\mathcal{D}_c \\ -\partial_n c^*|_{\bar{n}} \cdot \sigma_{\text{loc}} & -\mathcal{D}_c + \sigma_{\text{loc}} \end{pmatrix}. \quad (34)$$

Of the two eigenvalues of this Jacobian, the one with the larger real part determines the growth rate of the lateral instability, signified as σ_{lat} . As illustrated in Fig. 3(d), there are two limiting regimes: (i) In the *reaction-limited* regime ($\mathcal{D}_c \gg |\sigma_{\text{loc}}|$), the instability is limited by the rate at which the shifting equilibria are approached ($\sigma_{\text{lat}} \approx \partial_n c^* \cdot \sigma_{\text{loc}} = f_m$). (ii) In the *diffusion-limited* regime ($\mathcal{D}_c \ll |\sigma_{\text{loc}}|$), the concentrations are slaved to the local equilibria such that the growth rate of the lateral instability is limited by cytosolic redistribution via diffusion ($\sigma_{\text{lat}} \approx -\partial_n c^* \cdot \mathcal{D}_c$). In Appendix C4, we calculate the eigenvectors in phase space for the two

limiting regimes.

2. The role of membrane diffusion

Above we found that the physical processes driving a mass-redistribution instability are chemical reactions and cytosolic diffusion. What is the role of membrane diffusion that we had set to zero so far? Mathematically one needs to study the full Jacobian, Eq. (C10), including membrane diffusion, given in Appendix C3. Here, we provide a physical discussion for the role of membrane diffusion.

To start with, we notice that when the nullcline slope is negative ($-1 < \partial_n c^* < 0$), the membrane gradient will always be opposed to the cytosolic gradient (because

$\delta m = \delta n - \delta c$ and $\delta c^* = \delta n \partial_n c^*$). Therefore, membrane diffusion will always counteract the cytosolic diffusion that drives the MRI. How does this counteracting flow play out in the diffusion- and reaction-limited regimes of the MRI? To study the effect of membrane diffusion, imagine a system where membrane diffusion is ‘switched off’ initially, so the instability is governed by the dynamics Eq. (33) discussed above with the diffusion- and reaction-limited regimes. We then ask how switching on membrane diffusion affects the dynamics. Note that the terms diffusion- and reaction-limited refer to respective slow and fast *cytosolic* diffusion compared to the reactive flows. In a spatially continuous system, these regimes correspond to long and short wavelengths, respectively. As we will see next, membrane diffusion plays different roles in these two regimes.

Let us start with the diffusion-limited regime, corresponding to the limit where exchange rates are much smaller than reaction rates: $\mathcal{D}_{m,c} \ll |\sigma_{\text{loc}}|$. As noted earlier, one can use the analysis of the two-compartment system to infer the dynamics of the spatially continuous system: the exchange rates relate to the diffusion constants (Eq. (32)), $\mathcal{D} \sim D/L^2$, and $q = \pi/L$, cf. the dispersion relation in Fig. 3(b). Hence, the diffusion-limited regime of the two-compartment system corresponds to the long wavelength regime, $q \lesssim \sqrt{|\sigma_{\text{loc}}|/D_c}$, in the spatially continuous system.

In this regime, local concentrations are slaved to local equilibria, and thereby concentration gradients are directly determined by the differences in the local equilibria: $\partial_t \delta n = -\mathcal{D}_m \delta m^* - \mathcal{D}_c \delta c^*$. The diffusive flows balance when $-D_m/D_c = \delta c^*/\delta m^* = \chi$. Thus we recover the nullcline slope criterion, Eq. (25), for the onset of the (long wavelength) lateral instability. In conclusion, the role of membrane diffusion in the diffusion-limited (i.e. long wavelength) regime is to determine the maximal nullcline slope required for a MRI.

Next we discuss the reaction-limited regime, where cytosolic diffusion is much faster than chemical relaxation: $\mathcal{D}_c \gg |\sigma_{\text{loc}}|$, corresponding to short wavelengths, $q \gg \sqrt{|\sigma_{\text{loc}}|/D_c}$, in the spatially continuous system.

Recall that we consider a system that has a mass-redistribution instability for $D_m = 0$ and ask how this instability is affected by ‘switching on’ membrane diffusion. In the reaction-limited regime, the growth rate of perturbations in the absence of membrane diffusion is $\sigma_{\text{lat}} \approx \partial_n c^* \cdot \sigma_{\text{loc}} = f_m$, as we found previously in this section (see Fig. 3(d)). Additional (slow) membrane diffusion will counteract this instability, giving rise to the dispersion relation $\sigma(q) \approx f_m - D_m q^2$, as shown in Fig. 3(f). In particular, membrane diffusion balances against the MRI on the scale $\ell = \sqrt{D_m/f_m}$, and suppresses instability on shorter scales. These simple estimates hold for short enough length scales, deep in the laterally unstable regime (far from onset; see Appendix C3). Mass-redistribution due to cytosolic diffusion becomes limiting for long wavelengths, respectively small wavenumbers $q \lesssim \sqrt{|\sigma_{\text{loc}}|/D_c}$, where adiabatic scaffolding holds,

as discussed above.

Finally, we would like to note that it is important to keep in mind that the lateral instability is always driven by cytosolic mass redistribution. From this perspective the strict asymptotic limit $D_c \rightarrow \infty$ is pathological as it masks the core dynamics underlying lateral instability in McRD systems: the formation of gradients in the fast diffusing component(s) and the ensuing diffusive fluxes that redistribute total density. Somewhat deceptively, the dispersion relation in this regime resembles the shape of a locally unstable system for $q > 0$ (Fig. 3), even though the system is locally stable. Furthermore, in systems with more than two components, the subtle interplay of multiple fast diffusing components might play an important role for pattern formation [31]. Such aspects would be missed if fast diffusing components are assumed to be well-mixed at all times (which corresponds to setting their diffusion constants to infinity).

3. The marginal mode q_{max}

Above, we have found the right-hand edge of the band of unstable modes, $q_{\text{max}} \approx \sqrt{f_m/D_m}$ (in the limit $D_m \ll D_c$), based on a simple scaling argument. As shown next, the exact expression for q_{max} can be found quite easily by utilizing phase-space geometry. We start from the observation that q_{max} is a non-oscillatory marginal mode; it cannot be oscillatory for a locally stable fixed point, $\sigma_{\text{loc}} < 0$, as shown in Appendix C. Hence, the eigenvalue $\sigma(q_{\text{max}}) = 0$, so the mode $\sim \cos(q_{\text{max}}x)$ must fulfill the steady-state condition, Eq. (8), and the corresponding eigenvector must point along a flux-balance subspace $\propto (1, -D_m/D_c)^T$ in phase space. The steady state condition in flux-balance subspace is given by Eq. (14a), which, in linearization around a homogeneous steady state reads

$$0 = D_m \nabla_x^2 \delta m(x) + \left(f_m|_{\bar{n}} - \frac{D_m}{D_c} f_c|_{\bar{n}} \right) \delta m(x). \quad (35)$$

This equation is solved by the mode $\delta m(x) \propto \cos(q_{\text{max}}x)$ with $q_{\text{max}}^2 = f_m/D_m - f_c/D_c$ (cf. Eq. (27)). In the expression for q_{max} , the two effects of membrane diffusion are interlinked: (i) The condition $q_{\text{max}} = 0$ determines the critical NC-slope ($\chi_{\text{crit}} = -D_m/D_c$) for the (long wavelength) onset of lateral instability. (ii) In the laterally unstable regime, q_{max} determines the minimal length scale, $\ell = \sqrt{D_m/f_m}$, that can exhibit an instability ($q_{\text{max}} \rightarrow \ell^{-1}$ for $D_c \rightarrow \infty$).

We will later show that the marginal mode q_{max} at the *pattern inflection point* determines (to lowest order) the interface width of a stationary pattern.

4. The biophysical principle of attachment and detachment zones

A major motivation to study two-component McRD systems is intracellular pattern formation – specifically

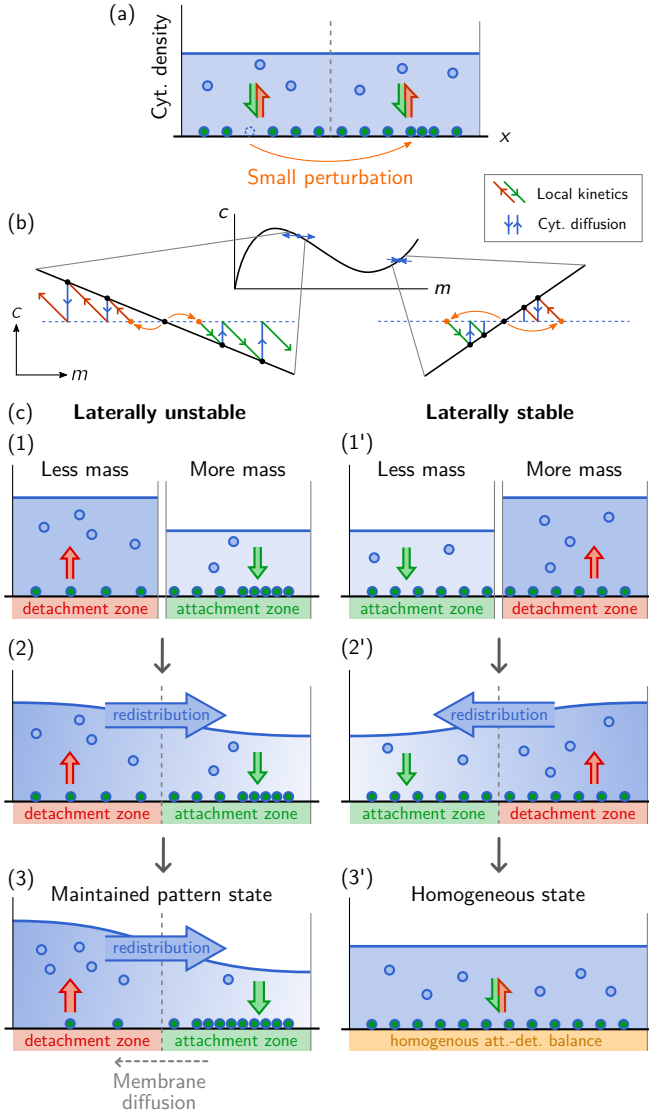


FIG. 4. Illustration of lateral (in)stability using the heuristic picture of attachment and detachment zones [57]. (a) A spatially extended system where proteins can switch between a membrane bound (illustrated by filled circles) and a cytosolic state (open circles); cytosolic density profile is shown as blue line. Panels (c1)–(c3) illustrate the time evolution of a system following a small redistribution of mass (orange arrow). The direction in which local equilibria shift due to a change of local mass can be read off from the reactive nullcline, shown in the (m, c) -phase-space plots (b). Shifting chemical equilibria cause the formation of attachment and detachment zones ((c1) and (c1')). Diffusive coupling leads to mass redistribution due to the induced cytosolic gradients (c2) and (c2')). Alternating between local chemical relaxation in isolated compartments (c1), (c1') and diffusive relaxation can be illustrated as a cobweb diagram in (m, c) -phase space. The mass-redistribution cascade continues until a steady-state pattern (c3) is reached, where diffusion on the membrane balances against cytosolic diffusion. A laterally stable system returns to the homogenous steady state (c3').

cell polarization. In a recent review on intracellular self-organization, we introduced attachment and detachment zones as heuristic concepts to illustrate the core mechanism of intracellular pattern formation [57]. Figure 4 shows how shifting local equilibria underly this picture of spatially separated attachment and detachment zones. These zones denote spatial regions where one has a net reactive flow of proteins from the cytosol to the membrane (attachment zone) or conversely from the membrane to the cytosol (detachment zone). Whether an increase in local total density leads to formation of an attachment or detachment zone is determined by the direction in which the cytosolic equilibrium concentration shifts. If the concentration decreases, an attachment zone forms; conversely, a detachment zone forms when the cytosolic equilibrium concentration increases.

The bottom panel in Fig. 4(c) shows a stationary pattern where the mass-redistribution cascade has stopped because membrane diffusion counteracts cytosol diffusion. The diffusive fluxes in and out of the compartments must be compensated by respective reactive turnovers within the compartments (cf. Eq. (36)): proteins in the cytosolic state diffusively flow from the detachment to the attachment zone where net conversion to the membrane-bound state dominates. The diffusive flux on the membrane transports these proteins back to the detachment zone where they detach into the cytosol, thus closing the cycle. In the next section (Sec. IV B), we will discuss this *flux–turnover* balance in detail. How flux–turnover balance is achieved in a spatially continuous system determines the characteristic pattern type, and depends on the shape of the reactive nullcline as we will discuss in Sec. V B.

5. Ostwald ripening is a mass-redistribution instability

The key principles underlying the mass-redistribution instability can also be found in other physical systems beyond mass-conserving reaction–diffusion systems (McRD). Some representative examples are shown in Fig. 5. The main ingredients are the notion of a ‘local equilibrium’ controlled by a conserved quantity, and the redistribution of that quantity due to gradients that are induced by shifting of the ‘local equilibria’. In a reaction–diffusion system, the local equilibrium is the chemical equilibrium in a well-mixed compartment, controlled by the total density in the compartment as shown in Fig. 5(a).

Binary mixtures (close to equilibrium) can phase-separate by spinodal decomposition [65]. This process is phenomenologically similar to a Turing instability (band of unstable modes) but is physically unrelated. The patterns that form due to spinodal decomposition then undergo a coarsening process driven by interface curvature. Curvature driven coarsening of spherical droplets is called Ostwald ripening. Interestingly, Ostwald ripening can be phrased in the language of ‘local equilibria’ and

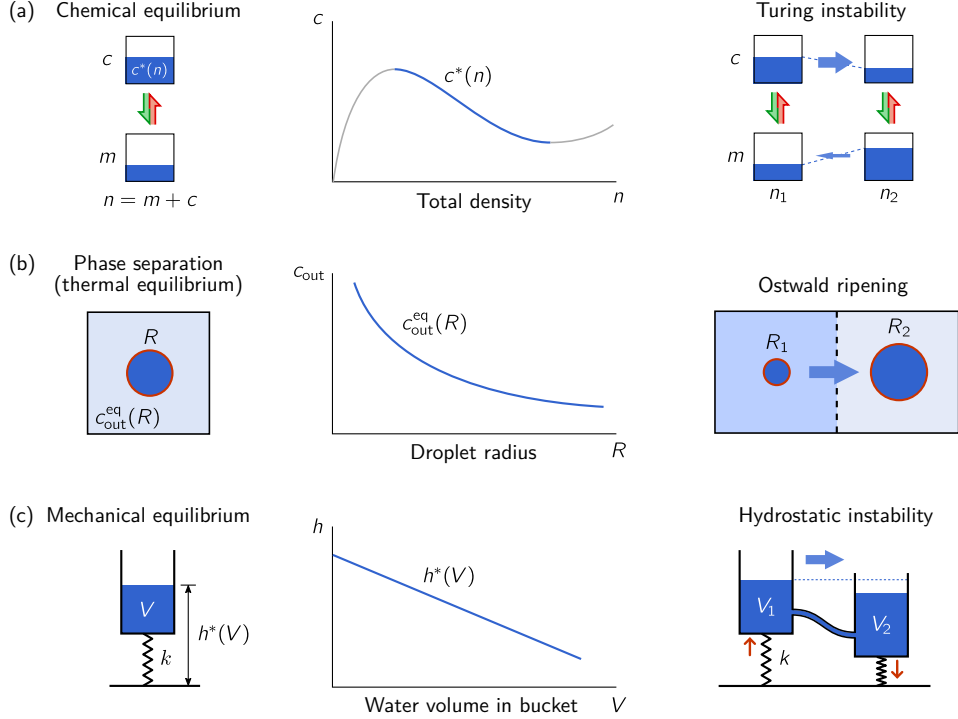


FIG. 5. Three physically distinct but topologically equivalent systems exhibiting mass-redistribution instabilities: (a) Mass-conserving reaction–diffusion systems; (b) Ostwald ripening (coarsening) in equilibrium phase separation; (c) a mechanical analog constructed from hydrostatically coupled buckets on springs. Each of the systems has a conserved quantity that plays the role of a control parameter in isolated compartment (shown on the left), where it controls the the equilibrium relations shown in the center). The equilibrium state of an isolated compartment plays the role of a ‘local equilibrium’. When two compartments are laterally coupled (by diffusion in (a) and (b); hydrostatically in (c)), redistribution of the conserved quantity shifts the ‘local equilibria’, thereby inducing gradients which drive further redistribution of the conserved quantity. This cascade underlies the lateral instability in all three systems. The gradients in the three systems are in: (a) the concentration of the cytosolic (fast diffusing) component, $c^*(n)$, decreasing as total density increases due to recruitment to the membrane (cf. Fig. 4); (b) the concentration outside the droplet, $c_{\text{out}}^{\text{eq}}(R)$, decreasing as the droplet radius increases due to interfacial tension (see Refs. [63, 64]); (c) the water level, $h^*(V)$, decreasing as the water volume increases due to the depression of the (weak) spring (see Appendix C 5).

mass redistribution (Fig. 5(b)). The analog of a local equilibrium is a phase-separated equilibrium state with a single droplet in a compartment. The spatial average \bar{c} of the concentration (order parameter) in the compartment is conserved. The equilibrium concentration outside the droplet, $c_{\text{out}}^{\text{eq}}(R)$, depends on the droplet radius R due to the interfacial tension [63, 64]. The droplet radius $R \sim V_{\text{drop}}^{1/d}$ in turn depends on the average concentration in the compartment via conservation of mass $V_{\text{box}}\bar{c} = V_{\text{box}}c_{\text{out}}^{\text{eq}} + V_{\text{drop}}(c_{\text{in}}^{\text{eq}} - c_{\text{out}}^{\text{eq}})$. For systems in (thermodynamic) equilibrium, one always has $\partial_R c_{\text{out}}^{\text{eq}} < 0$, i.e. an outside concentration decreasing with increasing radius, and thus a mass-redistribution instability (compare nullcline slope criterion, Eq. (25), for the reaction–diffusion system, which is laterally unstable when the cytosolic (fast diffusing) concentration lowers as total density is increased).

The mass-redistribution instability is the general physical principle underlying the Turing instability in mass-

conserving reaction–diffusion systems. In phase space, the mass-redistribution instability is characterized by the slope of the line of local equilibria (reactive nullcline in the case of a reaction–diffusion system). This phase-space structure is shared by all three physically distinct processes shown in Fig. 5 — Turing instability, Ostwald ripening and the mechanical analog (the latter will be explained in the next paragraph). These phenomena are therefore *topologically equivalent*. In fact, along similar lines as we have studied above for the McRD system (cf. Fig. 3(d)), Wagner [64] considers both a diffusion- and reaction-limited regimes of the Ostwald ripening process. Also note that in non-equilibrium systems, there can be reverse Ostwald ripening ($\partial_R c_{\text{out}}^{\text{eq}} > 0$, see e.g. Refs. [66–68]), corresponding to lateral stability in the reaction–diffusion language.

Since understanding the Ostwald process requires an in-depth knowledge of the physics of phase separation, we devised a more elementary and intuitive system exhibiting MRI based on mechanical equilibrium: two water-

filled buckets – each resting on an overdamped spring – exchanging water through a pipe due to hydrostatic pressure gradient (Fig. 5(c)). Chemical equilibria correspond to mechanical equilibria — the height of the water level $h^*(V)$ as function of the water volume V in the bucket. For a sufficiently soft spring, the compression of the spring can lead to a decrease of the water level above ground upon increase of the water volume ($\partial_V h^*(V) < 0$, see Appendix C 5 for details). The essential point of the analogy is, that the equilibria shift as water flows from one bucket to the other. The flow of water is driven by the hydrostatic pressure difference (proportional to the height difference δh) — analogously to cytosolic diffusion due to a cytosolic gradient. In the case $\partial_V h^*(V) < 0$, this gives rise to a mass-redistribution instability equivalent to both Ostwald ripening of phase separated droplets and Turing’s instability in a chemical system with diffusive coupling. Note that membrane diffusion is not captured by the mechanical analogy.

B. MRI terminates due to flux-turnover balance

How does the mass-redistribution cascade driving lateral instability terminate? In general, this will depend on the interplay between local relaxation to chemical equilibria and diffusive flows induced by concentration gradients; see Fig. 6(a). There are several asymptotic limits which are instructive.

Consider the situation where membrane diffusion is negligible (Fig. 6(b)), i.e. for $\mathcal{D}_m \ll \mathcal{D}_c$ and $\mathcal{D}_m \ll \sigma_{loc}$ (as we discussed for lateral instability previously in this section). Then, one can set $\mathcal{D}_m = 0$. In this limit there is no process counteracting cytosolic redistribution of mass, such that the mass-redistribution cascade will continue until all cytosolic gradients are removed, $c_1 = c_2$, and the diffusive flux between the compartments ceases. In steady state, the reactive flows within each of the compartments have to vanish, and both compartments must be in their respective chemical equilibrium with identical cytosolic concentration, $c^*(n_1) = c^*(n_2)$.

How does this picture change if there is a non-zero membrane diffusive exchange rate ($\mathcal{D}_m \neq 0$)? Then, the membrane gradient building up as the pattern amplitude grows leads to a diffusive flux $\mathcal{D}_m(m_2 - m_1)$ that counteracts cytosolic redistribution $\mathcal{D}_c(c_2 - c_1)$. In steady state, these diffusive fluxes must balance each other: the pattern lies in a flux-balance subspace (cf. Eq. (10)). Moreover, the diffusive fluxes need to be compensated by corresponding reactive turnovers that interconvert membrane-bound and cytosolic proteins in each of the two compartments; see Fig. 6(c). This flux–turnover balance was already introduced heuristically within the picture of attachment and detachment zones above.

Finally, we examine flux–turnover balance in two limiting cases for the system size: close to onset of lateral instability $L \approx L_{min} = \pi/q_{max}$, and in a large system $L \gg L_{min}$. At $L = L_{min}$, the homogeneous steady state

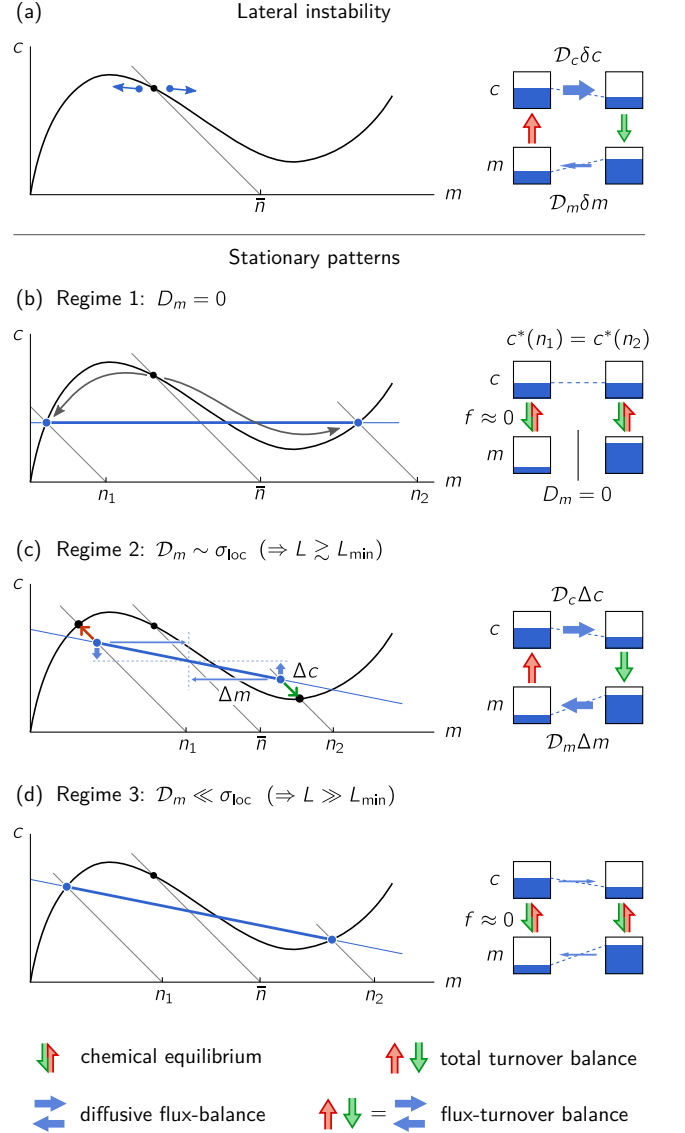


FIG. 6. Stationary patterns are determined by different processes in three distinct regimes of diffusive and kinetic timescales. (a) Lateral instability is a mass-redistribution instability driven by cytosolic diffusion. How the mass-redistribution cascade terminates, depends on the interplay of local relaxation to the chemical equilibria (illustrated by red/green arrows; rate $\sim \sigma_{loc}$), and the diffusive redistribution (illustrated by blue arrows; rates $\mathcal{D}_{m,c}$): (b) When membrane diffusion is negligible ($\mathcal{D}_m = 0$), the cytosolic gradient must vanish, so that mass redistribution ceases. The compartments then effectively decouple such that each must be in chemical equilibrium – with identical cytosolic concentrations $c^*(n_1) = c^*(n_2)$. (c) For non-negligible membrane diffusion ($\mathcal{D}_m \sim \sigma_{loc}$), cytosolic and membrane fluxes have to balance in steady state. To sustain these fluxes (illustrated by blue arrows), there has to be reactive turnover in each compartment (red and green arrows). This is flux–turnover balance. (d) In a large system ($L \gg L_{min}$), the exchange rates are small compared to the chemical reactions ($\mathcal{D}_m \ll \sigma_{loc}$). Hence, the compartments must be close to chemical equilibrium.

is marginally stable, i.e. flux–turnover balance is fulfilled for small perturbations along the marginally stable eigenvector (cf. discussion of q_{\max} above). For a slightly larger system, the reactive flows initially dominate and drive a mass redistribution instability by inducing a cytosolic gradient. If the reactive flows grow sub-linearly with pattern amplitude, the linearly growing diffusive flux on the membrane will quickly outcompete them. Hence the pattern will stop growing at small amplitude. In this case, the bifurcation at L_{\min} is supercritical. Otherwise (if the reactive flows grow super-linearly), the bifurcation will be subcritical (see Sec. VIII D below for a detailed discussion of sub- vs. supercriticality). For large system size ($L \gg L_{\min}$), the exchange rates $\mathcal{D}_{m,c} \propto D_{m,c}/L^2$ between the two compartments become small (correspondingly, in a spatially continuous the gradient of the longest wavelength mode q_1 becomes shallow; cf. Eq. (32)). Therefore, also the reactive turnovers that balance against the diffusive fluxes must become small: the compartments approach chemical equilibria (Fig. 6(d)). These chemical equilibria must be FBS–NC intersection points. Therefore, they can be found by geometric construction in (m, c) -phase space by constraining their center of mass to the conserved average total density $(n_1 + n_2)/2 = \bar{n}$. The corresponding pattern in a spatially continuous system comprises two plateaus connected by an interfacial region as shown in Fig. 2. Since reactive turnover vanishes in the plateaus, flux–turnover balance in a spatially continuous system must be established in the interfacial region (cf. Fig. 2). In the following section, we will characterize the pattern attractors in the spatially continuous system. The key additional aspect compared to the two-compartment system will be the self-organization of spatial regions: the interface and the plateaus.

V. CHARACTERIZATION OF STATIONARY PATTERNS

With an intuitive picture of the principles underlying pattern formation in two-component McRD systems in hand, we now return to the spatially continuous system. We first study the characteristic types of stationary patterns exhibited by two-component McRD systems. In the following, we focus on *elementary* stationary patterns with monotonic concentration profiles on a domain with no-flux boundaries. More complex, non-monotonic steady-state patterns (also in domains with periodic boundary conditions) can always be dissected into such elementary patterns at their extrema (recall that due to the diffusive flux–balance condition, Eq. (9), extrema in $\tilde{m}(x)$ and $\tilde{c}(x)$ must coincide). It was previously observed in the literature that two-component McRD systems typically exhibit coarsening, also called ‘winner takes all’ dynamics, where high density regions compete for mass until only one winner, i.e. a single high density region (peak or plateau) remains [35, 36, 44, 69].

For specific types of the reaction term, inevitability of coarsening was actually proved mathematically, by showing that any *stable* steady state must be monotonic in space [70, 71]. This numerical and mathematical evidence suggests that non-monotonic (composite) patterns are generically unstable and exhibit a coarsening dynamics, similar to the Ostwald ripening process of phase separation near thermal equilibrium. Studying ‘composite’ patterns, in particular their stability, will be an important direction for future research.

As a preliminary to the following sections, we study flux–turnover balance in the spatially continuous system. Multiplying the stationarity condition, Eq. (8a), by $\partial_x \tilde{m}(x)$ (as we did for total turnover balance Eq. (17) and integrating over a spatial subinterval $[0, x]$), one obtains a relation that depends only on the boundary concentrations $\tilde{m}(0)$ and $\tilde{m}(L)$:

$$\begin{aligned} \frac{1}{2} D_m (\nabla_x \tilde{m}|_{x_0})^2 &= \int_{\tilde{m}(0)}^{m_0(\eta_0)} dm \tilde{f}(m, \eta_0) \\ &= - \int_{m_0(\eta_0)}^{\tilde{m}(L)} dm \tilde{f}(m, \eta_0). \end{aligned} \quad (36)$$

This equation shows that the net turnover on either side of the pattern inflection point x_0 , has to be balanced by the net diffusive flux across that point; for an illustration see Fig. 2(a). Because the reactive flow changes sign at the inflection point, the reactive turnover (integrated flow) is extremal there and determines the maximal slope $\tilde{m}'(x_0)$ of the pattern profile. Depending on how the reactive turnover saturates on either side of the inflection point, the system exhibits, as we will learn in Sec. V B, three distinct characteristic elementary pattern types, classified by the shape of the concentration profile $\tilde{m}(x)$: mesas, peaks/troughs and nearly harmonic (or ‘weakly nonlinear’) patterns; see Fig. 7.

The pattern type determines the ‘positional information’ it can convey, i.e. how it can organize biological function [72]. Mesa patterns (two plateaus connected by an interface) define sharply separated zones / spatial domains, as e.g. the PAR system in *C. elegans* [73, 74]. Peak patterns (a sharp high density region rising from a low density plateau) sharply position a single spot, as e.g. the Cdc42 system in *S. cerevisiae* [37, 44, 75, 76]. The interface width determines how sharp the features are defined (i.e. how steep the intracellular gradient is). When the interface width is comparable to the system size, a pattern without plateaus (‘weakly nonlinear’) forms that determines polarity but no sharp positioning.

A. Interface width

The width of the interfacial region, L_{int} , is the only intrinsic length scale of the elementary patterns. Therefore, we begin our characterization of the pattern attractors by estimating L_{int} . Recall that the pattern inflection point, which defines the position of the interface re-

gion, is at chemical equilibrium – geometrically determined by a FBS–NC intersection (m_0, c_0) (cf. Fig. 2 in Sec. III C). The interface, and with it the pattern, is maintained by a balance of diffusion and the reactive flow in the vicinity of the pattern inflection point, i.e. by flux-turnover balance (cf. Sec. IV B). Therefore, the phase-space flow in the vicinity of the inflection point determines the properties (in particular the width) of the interface. To leading order, we can determine the interface $\tilde{m}(x - x_0) \approx m_0 + \delta\tilde{m}(x)$ by linearizing the steady-state equation, Eq. (8a), around the inflection point,

$$0 = D_m \nabla_x^2 \delta\tilde{m}(x) + \left(f_m|_{n_0} - \frac{D_m}{D_c} f_c|_{n_0} \right) \delta\tilde{m}(x), \quad (37)$$

where $n_0 = m_0 + c_0$ is the total density at the pattern inflection point, and we used the flux-balance subspace, Eq. (10), to substitute the cytosol concentration $\delta\tilde{c}(x)$. We already encountered an equation of the form of Eq. (37) when we studied the marginal mode q_{\max} in the dispersion relation (right-hand edge of the band of unstable modes). Hence, the interface length scale is determined by

$$L_{\text{int}} \simeq \pi/q_{\max}(n_0) = \pi\sqrt{D_m/\tilde{f}_m|_{n_0}}, \quad (38)$$

the marginal mode of the dispersion relation *at the inflection point*. The interface shape is approximated by the corresponding eigenfunction $\delta\tilde{m}(x) \propto \sin(q_{\max}(n_0)x)$.

Let us pause for a moment to look at the interface region from the perspective of mass redistribution: the total density n_0 at the inflection point is such that the corresponding chemical equilibrium is laterally unstable, because the nullcline slope is steeper than the FBS-slope there; see Fig. 9 below, where we elaborate on this point in terms of spatial *regions*. From the spectrum of modes, only the marginally stable one, $q_{\max}(n_0)$, fulfills the (linearized) stationarity condition. Thus, intuitively it must be the q_{\max} mode that determines the interface length scale. Importantly, as the pattern is formed by mass redistribution, the total density n_0 at the inflection point does not coincide in general with the average total density \bar{n} — the interface width is determined $q_{\max}(n_0)$, not by $q_{\max}(\bar{n})$.

Note on notation: In the following we will usually denote the interface width by $L_{\text{int}}(\eta_0)$, using that the inflection point (m_0, c_0) , and hence $n_0 = m_0 + c_0$ is determined geometrically as FBS–NC intersection point given the FBS-position η_0 .

The maximal slope of the interface profile $\tilde{m}'(x_0)$ is attained at the pattern inflection point x_0 and can be calculated by flux-turnover balance (36); see Sec. IV B. Together with the harmonic mode $\delta\tilde{m}(x) \propto \sin(\pi x/L_{\text{int}})$ obtained by linearizing phase space flow, we find the (approximate) stationary pattern profile in the vicinity of the inflection point

$$\tilde{m}(x) \approx m_0 + \tilde{m}'(x_0) \frac{L_{\text{int}}}{\pi} \sin\left(\pi \frac{x - x_0}{L_{\text{int}}}\right). \quad (39)$$

To go beyond this leading order approximations, one can perform a perturbative expansion of $\tilde{f}(m_0 + \delta m, \eta_0)$ and $\tilde{m}(x_0 + \delta x)$ in Eq. (8a) around the pattern inflection point (m_0, η_0) . The solution of this expansion can then be matched to the plateaus to obtain an approximation of the interface profile shape. Linearization around the plateaus yields exponential decay towards the plateaus (“exponential tails”) $\sim \exp(-x/\ell_{\pm})$, where the decay lengths are given by $\ell_{\pm}^2 = D_m/\tilde{f}_m(n_{\pm})$.

B. Pattern classification

With an estimate for the interface width at hand, we can now turn to the characterization of the pattern types exhibited by two-component McRD systems.

1. Plateau–interface–plateau (mesa pattern)

Reactive turnover is generated when the concentrations (which, in steady state, are constrained to the flux-balance subspace) deviate from the local equilibria, represented by the reactive nullcline. Hence, when the maximum/minimum of a growing pattern reaches an intersection point of FBS and NC in phase space, the reactive turnover on this side of the pattern inflection point saturates and the system assumes a plateau slaved to local equilibria in a spatially extended part of the system (cf. Sec. III C). When the reactive turnover saturates on both sides of the inflection point ($L \gg L_{\text{int}}$), the pattern profile comprises two plateaus connected by an interface (Fig. 7(a)). We will call these patterns ‘mesa patterns’ [54].

Before we continue to characterize mesa patterns, we provide a geometric argument for the lateral stability of the plateau regions: In the previous section, we learned that the interface width is determined by the $q_{\max}(n_0)$ -mode, where n_0 is the total density at the interface (pattern inflection point). Hence, the interface must exhibit a band of unstable modes $[0, q_{\max}(n_0)]$. From the slope criterion for lateral instability, Eq. (25), we conclude that the slope of the reactive nullcline at the inflection point must always be smaller than the FBS-slope ($-\partial_m c^*(m) < -D_m/D_c$). In turn, the plateaus must be laterally stable because at the corresponding FBS–NC intersection points $-\partial_m c^*(m) > -D_m/D_c$, for a N-shaped nullcline. Note that in McRD systems with more than two-components, this geometric argument can be broken due to the additional phase-space dimensions: there can be “secondary” processes destabilizing the plateaus (such processes have been referred to as ‘anti-coarsening’ [77], ‘peak-splitting’ [78, 79], or ‘self-replication’ [55] in the literature).

To characterize mesa patterns ($L \gg L_{\text{int}}$), we first determine the FBS-position, η_0 , using total turnover balance, (17) (cf. Sec. III C). Since the plateaus are slaved

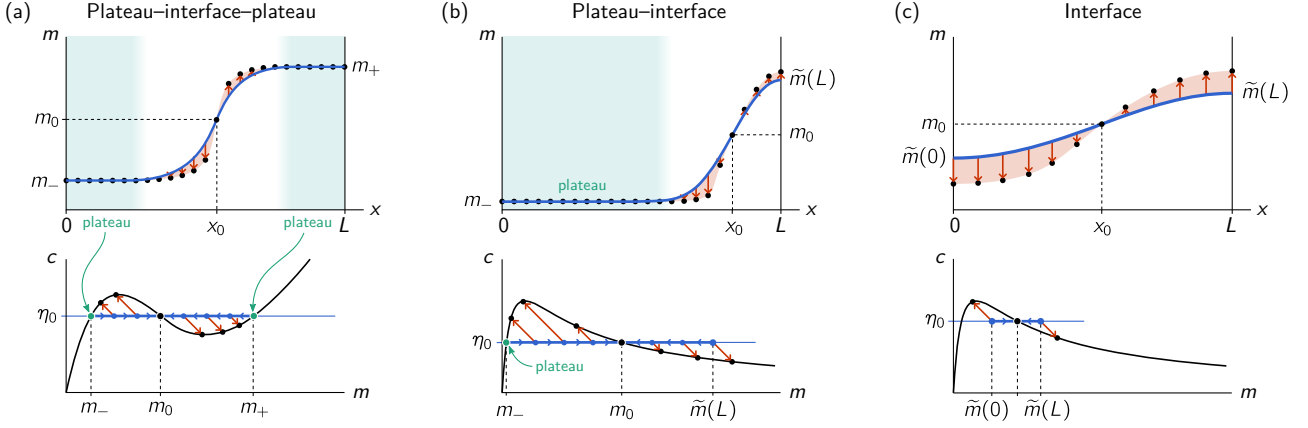


FIG. 7. Three possible types of polarized patterns, classified by the number of plateaus. Since the plateaus reveal themselves as intersections of flux-balance subspace and reactive nullcline (in regions with positive slope) in phase space, the shape of the reactive nullcline together with the ratio of diffusion constants (flux-balance subspace) determine the characteristic pattern type of a given two-component system. (a) When local equilibria limit further amplitude growth on both sides of the inflection point two plateaus form resulting in a mesa pattern. (b) A (half-)peak connected to a single plateau forms when a local equilibrium is reached on one side of the inflection point. At this equilibrium, the flow vanishes so the turnover is bounded, which in turn determines the peak amplitude on the other side in dependence of system size and average total density. (c) The weakly nonlinear, interface only, profile type only occurs in short systems where the reactive turnover is balanced by the linearly growing diffusive flux at small amplitude (before any plateau is reached). (Note that the number of arrows shown does not have a deeper meaning but is chosen for illustration purposes alone.)

to (laterally stable) local chemical equilibria we can approximate the boundary concentrations

$$\tilde{m}(0) \approx m_-(\eta_0), \tilde{m}(L) \approx m_+(\eta_0), \quad (40)$$

where the *plateau scaffolds* $m_{\pm}(\eta_0)$ are geometrically determined in phase space as intersection points $m_{\pm}(\eta_0)$ of FBS and NC:

$$\tilde{f}(m_{\pm}, \eta_0) = 0. \quad (41)$$

With the approximation, Eq. (40), the total reactive turnover balance condition, Eq. (17), becomes:

$$\eta_0^{\infty} : \int_{m_{-}^{\infty}}^{m_{+}^{\infty}} dm \tilde{f}(m, \eta_0^{\infty}) = 0, \quad (42)$$

where $m_{\pm}^{\infty} = m_{\pm}(\eta_0^{\infty})$ and η_0^{∞} denotes the FBS-position in the large system size limit. Equation (42) is closed and can be solved for η_0^{∞} . Once one has determined η_0^{∞} , the interface width, L_{int} , can be estimated with Eq. (43) using the total density $n_0(\eta_0^{\infty})$ at the geometrically determined inflection point.

Note that equation Eq. (42) – and thus η_0^{∞} – does neither depend on \bar{n} nor on L . For mesa patterns, the average total density \bar{n} determines the position x_0 of the interface. Assuming an interface much narrower than the system size, its position can be approximately determined by mass conservation, $n_{-}^{\infty} x_0 + n_{+}^{\infty} (L - x_0) \approx L \bar{n}$, which yields

$$x_0 \approx L \frac{n_{+}^{\infty} - \bar{n}}{n_{+}^{\infty} - n_{-}^{\infty}}, \quad (43)$$

where n_{+}^{∞} and n_{-}^{∞} are the average total densities in the plateau regions:

$$n_{\pm}^{\infty} := \eta_0^{\infty} + (1 - D_m/D_c) m_{\pm}(\eta_0^{\infty}). \quad (44)$$

Notably, a geometric argument shows that mesa patterns are the generic pattern for $L \rightarrow \infty$ if the ratio of the diffusion constants is nonzero $D_m/D_c > 0$, and $m \geq 0$ and $c \geq 0$ (as must be the case for concentrations): the FBS will intersect the m -axis ($c = 0$) at $(D_c/D_m)\eta_0$, and hence must intersect the nullcline at some finite value $m < (D_c/D_m)\eta_0$. For $L \rightarrow \infty$, the pattern profile will reach this third FBS-NC intersection point, and thus become a mesa pattern. Below, we will discuss the conditions under which other pattern types, namely ‘peak/trough patterns’ and ‘weakly nonlinear patterns’ occur.

Mesa patterns are commonly studied with a so called “Newton mapping” as briefly described in Sec. III C where we introduced total turnover balance. Our analysis puts this mathematical analogy into the context of phase-space geometry. Moreover, the phase-space geometric analysis presented here also allows us to study patterns with a plateau only on one side as we will see next.

The approximation Eq. (40) for the plateau densities, and in turn also Eq. (43) for the interface position, will break down when the distance of the interface to one of the system boundaries becomes smaller than the interface width $L_{\text{int}}(\eta_0^{\infty})$. Then the steady-state pattern no longer exhibits a plateau on that side and instead becomes a plateau-interface pattern, forming either a peak when

$\bar{n} \gtrsim n_-^\infty$, or a trough (‘anti-peak’) when $\bar{n} \lesssim n_+^\infty$. Based on the approximation for the interface position, Eq. (43), we can estimate a condition on \bar{n} for the transition from a mesa to a peak/trough pattern:

$$L |\bar{n} - n_\pm^\infty| \lesssim L_{\text{int}}(\eta_0^\infty) [n_+^\infty - n_-^\infty]. \quad (45)$$

2. Plateau–interface (peak/trough pattern)

Let us now study these peak/trough patterns. They form when the turnover saturates at a FBS–NC intersection on only one side of the inflection point such that only a single plateau forms. Consider, for specificity, a situation where the minimum membrane concentration extends to the plateau on the left hand side, $\tilde{m}(0) \approx m_-(\eta_0)$, while the maximum membrane concentration (‘peak amplitude’) $\tilde{m}(L)$ does not extend to the third FBS–NC intersection point $m_+(\eta_0)$. This typically happens when the reactive nullclines $c^*(m)$ decreases monotonically to the right of its turning point (Fig. 7(b)), and the flux-balance subspace is very shallow ($D_c \gg D_m$). The ensuing pattern comprises a plateau and an interface that forms a ‘peak’ (or, conversely, if the maximum is determined by a plateau, the interface forms a ‘trough’ or ‘anti-peak’).

Importantly, the position of the flux-balance subspace η_0 of peak/trough patterns is not given by η_0^∞ as we can no longer approximate the integral limits in total turnover balance by the plateaus m_\pm . Instead, we can estimate η_0 by making use of linearized flux–turnover balance in the vicinity of the pattern inflection point. Above, in Sec. V A, we have shown that this linearized flux–turnover balance (approximately) determines interface width $L_{\text{int}}(\eta_0)$, and that the interface shape can be approximated by $\sin((x - x_0)/L_{\text{int}})$; hence, we can roughly estimate the mass in a peak as

$$N_{\text{peak}} \approx \frac{1}{2} L_{\text{int}}(\eta_0) \tilde{m}(L). \quad (46)$$

To find a value for the FBS-position η_0 consistent with this estimate, we use that the pattern inflection point m_0 is approximately half-way between the plateau m_- and the maximum $\tilde{m}(L)$, such that we can eliminate $\tilde{m}(L) \approx m_- + 2(m_0 - m_-)$ in Eq. (46). The remaining unknowns m_0 and m_- are determined geometrically (FBS–NC intersections) as functions of η_0 , so we can determine the relation $\bar{n}(\eta_0) \approx n_-(\eta_0) + N_{\text{peak}}(\eta_0)/L$. The inverse of this relation yields the FBS position $\eta_0(\bar{n})$ as a function of the average total density \bar{n} . This estimate will hold until the peak density $\tilde{m}(L)$ reaches $m_+(\eta_0)$, where a second plateau will start to form, such that the peak pattern transitions to a mesa pattern. In Appendix G we present the details of the peak approximation, and a comparison to numerical solutions.

3. Interface (‘weakly nonlinear’ pattern)

Finally, if the mass-redistribution cascade is stopped by counteracting membrane diffusion before an intersection of FBS an NC is reached on either side of the inflection point, the pattern has no plateaus (Fig. 7(c)). For this to happen, the pattern must saturate at small amplitude, which typically is the case if the system size L is sufficiently small ($L_{\text{int}} \gtrsim L$) such that the membrane gradient grows quickly with amplitude, and thus can outcompete the reactive turnover; compare Fig. 6(c) for the corresponding case in the two-compartment system. For such a pattern, weakly nonlinear analysis can be used to find whether the diffusive flux outgrows the reactive turnover at small amplitudes (Sec. VIII D). At the onset of lateral instability, this competition of reactive and diffusive flows determines if the bifurcation (lateral instability) is sub- or supercritical. Stationary small amplitude patterns appear in the vicinity of a supercritical bifurcation, when $L \gtrsim L_{\text{int}}$.

C. Generic bifurcation structure for the total density \bar{n}

Now that we have classified the different types of stationary patterns exhibited by two-component McRD systems, we turn to study bifurcations where the patterns change structurally or in stability. The bifurcation parameter we study first is the average total density \bar{n} . This parameter does not affect the phase-space geometry (NC and FBS), which makes it particularly easy to study. Later, in Sec. VII, we generalize our findings to bifurcation parameters that change the phase-space geometry: diffusion constants change the FBS-slope, whereas kinetic rates affect the nullcline shape. For biological systems, the average total density \bar{n} is a natural parameter as it can be tuned by up- or down-regulating the production of a protein.

Let us begin with the bifurcations where the homogeneous steady state becomes laterally unstable. We have already learned in Sec. III D that there is a band of unstable modes, $[0, q_{\text{max}}]$, if the NC-slope $\chi(\bar{n})$ is negative and steeper than the FBS-slope, $-D_m/D_c$ (cf. Eq. (25) and Fig. 3(c)). Also recall that a system of size L is laterally unstable if its longest wavelength mode lies in the band of unstable modes ($\pi/L < q_{\text{max}}(\bar{n})$, where $q_{\text{max}}^2 = \tilde{f}_m/D_m$ as defined in Eq. (27)). In particular, in the limit of large system size, $L \rightarrow \infty$, the range of lateral instability ($n_{\text{lat}}^-, n_{\text{lat}}^+$), is delimited by the points $\tilde{f}_m(n_{\text{lat}}^\pm) = 0$, where the flux-balance subspace is tangential to the reactive nullcline (dash-dotted green lines in Fig. 8(a); recall that $\tilde{f}_m = f_m - f_c D_m/D_c = (-D_m/D_c - \chi)f_c$).

We have learned that the range of lateral instability is geometrically determined. What about the range where stationary patterns exist? The plateau scaffolds $m_\pm(\eta_0)$ are geometrically determined by the reactive nullcline via the FBS–NC intersection points. The position η_0 of the

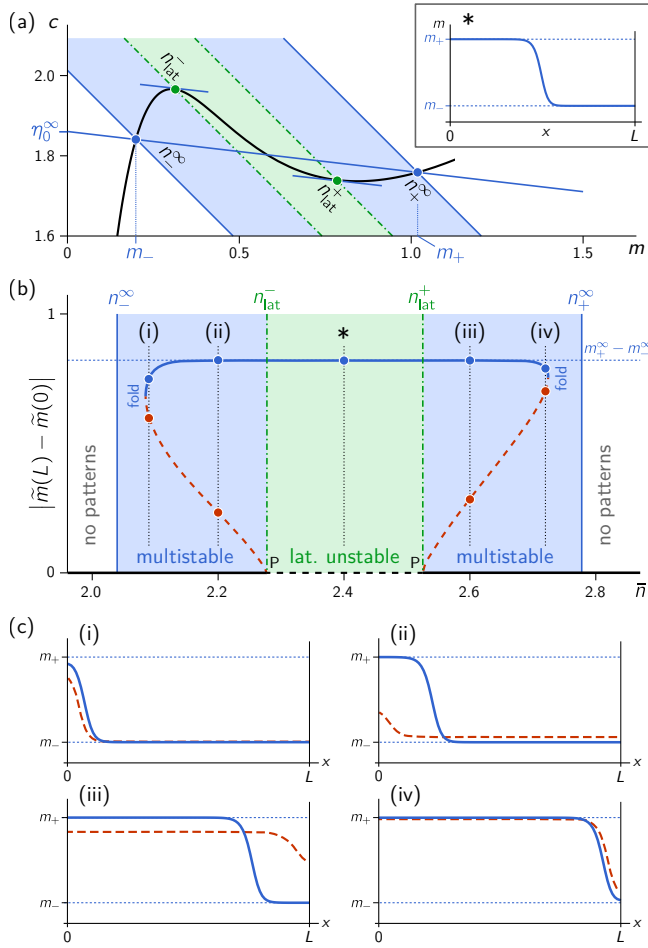


FIG. 8. Bifurcations of mesa patterns in the large system size limit ($L \rightarrow \infty$) can be constructed geometrically using the reactive nullcline. (a) Geometric construction of pattern bifurcation points for an example two-component system: Eq. (A1*) with $k = 0.07$, $D_m = 1$, and $D_c = 10$. The laterally unstable regime (shaded in green) is delimited by Turing bifurcations where the FBS is tangential to the NC (green dots, n_{lat}^{\pm}). FBS-NC intersection points (blue dots, n_{lat}^{\pm}), delimit the range of pattern existence (shaded in blue), where the FBS-position, η_0^{∞} , is determined by global turnover balance, Eq. (17). Inset in the top right corner: membrane density $\tilde{m}(x)$ of a stable mesa pattern for $\bar{n} = 2.4$ (see star in (b)). (b) Bifurcation structure of the pattern amplitude $|\tilde{m}(L) - \tilde{m}(0)|$ for the control parameter \bar{n} obtained by numerical continuation (cf. Appendix F) for a system size of $L = 100$. The branch of stable patterns (solid blue line) and the branches of unstable patterns (dashed red line) meet in fold bifurcations of patterns. Due to the finite system size, these fold bifurcations are offset from n_{lat}^{\pm} (vertical solid blue lines) by an amount $\sim L_{\text{int}}(\eta_0^{\infty})/L$. The unstable patterns emerge in subcritical pitchfork bifurcations (P) from the homogeneous steady state (black line) at the Turing bifurcations (vertical dash-dotted green lines). (c) Profiles $\tilde{m}(x)$ of stationary patterns (solid blue: stable, dashed red: unstable) for the average total densities $\bar{n} = 2.09, 2.2, 2.6$, and 2.72 (see thin dashed lines in (b)). The plateau scaffolds $m_{\pm}(\eta_0^{\infty})$ are shown as thin black lines.

flux-balance subspace generally depends on \bar{n} and L via total turnover balance, Eq. (17). However, in the large system size limit ($L \rightarrow \infty$), the FBS position η_0^{∞} is independent of \bar{n} and L (cf. Eq. (42)). For patterns to exist, the average total density \bar{n} must lie in-between the plateau densities n_{lat}^{\pm} ; see Fig. 8(a), cf. Eq. (43). Hence, in the limit $L \rightarrow \infty$, stationary patterns exist in the range $n_{\text{lat}}^- < \bar{n} < n_{\text{lat}}^+$.

Importantly the range of pattern existence generically extends beyond the range of lateral instability ($n_{\text{lat}}^- > n_{\text{lat}}^+$ and $n_{\text{lat}}^+ < n_{\text{lat}}^-$) by geometric necessity for N-shaped nullclines; see Fig. 8(a). This implies, that generically there are regions of multistability in parameter space, where stable stationary patterns exist, and the homogeneous steady is stable (regions shaded in blue in Fig. 8).

To gain some intuition on the steady states in the multistable regimes, we performed numerical continuation (see Appendix F for details) of the steady-state patterns for an example two-component McRD system using the attachment–detachment kinetics Eq. (A1*) from Ref. [39] which exhibit an N-shaped nullcline. Figure 8(b) shows the numerically obtained bifurcation structure where we plot the pattern amplitude $|\tilde{m}(L) - \tilde{m}(0)|$ against the bifurcation parameter \bar{n} . The star marks a typical stable mesa pattern (see inset in (a)) in the central region of the branch of stable patterns (blue line). As the plateaus are slaved to the plateau scaffolds $m_{\pm}(\eta_0^{\infty})$, the pattern amplitude stays approximately constant ($m_+ - m_-$, dashed blue line) across the whole range of \bar{n} where patterns exist. Changing total average density only shifts the interface position (cf. panels (ii) and (iii) in (c)). When the interface position is in the vicinity of a boundary, mesa pattern transitions to peak patterns (see. panels (i) and (iv) in (c)) as we learned in the previous section (Eq. (45) in Sec. VB). The numerical continuation shows, that the peak/trough patterns are then annihilated in saddle-node bifurcations (SN), where the branch of stable patterns meets a branch of unstable patterns (dashed, red line). Due to the finite system size, the exact positions of the SN-bifurcation points are slightly offset from n_{lat}^{\pm} (by an amount $\sim L_{\text{int}}/L$). The branches of unstable patterns emerge from homogeneous steady state in subcritical pitchfork bifurcations (P) at the Turing bifurcations (n_{lat}^{\pm}). (In a finite sized system, the onset of lateral instability is offset by an amount $\sim L^2$; see Sec. VIID). In the multistable regions (shaded in blue), patterns can be triggered by a finite amplitude perturbation. The unstable patterns are “transition states” that lie on the separatrix separating the basins of attraction of the stable patterns and the stable homogeneous steady state. The actual separatrix is a complicated object in the high-dimensional PDE phase space. In the next section, we will show that a heuristic can be inferred from the nullcline shape to estimate the ‘excitability threshold’ for prototypical class of spatial perturbation profiles lateral excitability; see Sec. VI.

Because the unstable patterns are peak/trough patterns, they can be approximated by the ‘peak approx-

imation’ introduced in Sec. VB (see also Appendix G). Importantly, this implies that the qualitative structure of the branches of unstable patterns is determined by (m, c) -phase-space geometry independently of the details of the reaction term $f(m, c)$, as long as the reactive nullcline $f(m, c) = 0$ is N-shaped.

In summary, we conclude that the qualitative form of the bifurcation structure shown in Fig. 8(b) is determined by geometric relations in (m, c) -phase space. In particular, we find that two-component McRD systems generically have regions of multistability and that the onset of lateral instability is generically subcritical for large system size $L \gg L_{\text{int}}$. Further, this implies that such systems are excitable, and that there is hysteresis of stationary patterns when the total average density is varied.

In Sec. VII we extend our geometric reasoning to a (\bar{n}, D_c) -bifurcation diagram and also study the effect of nullcline shape deformations due to kinetic parameters. Furthermore, for systems close to onset, e.g. $L \gtrsim L_{\text{min}}$ we can apply weakly nonlinear analysis which enables us to approximate small amplitude patterns and yields the transition from sub- to supercriticality (Sec. VIID). As we will learn, this transition can also be related to local geometric properties of the reactive nullcline (specifically its curvature), similarly to the slope criterion for the onset of lateral instability (cf. Eq. (25)).

D. Summary — regions generalize the concept of local compartments

In this section, we have shown how to characterize the stationary pattern with the aid of structures in phase space. The recurring idea was to (notionally) decompose the pattern into spatial regions (plateaus and interface) corresponding to FBS–NC intersection points in phase space; see Fig. 9(a,b). The (linearized) properties of phase space in the vicinity of these landmark points were then used to determine the regional properties in space (Fig. 9(c,d)). This decomposition into regions can be understood as an extension of the original compartmentalization approach (cf. [28]) to a regional scale. Recall that the dissection (“compartmentalization”) of a system into isolated small (i.e. well-mixed) local compartments, is the foundation for the concept of local equilibria that serve as proxies for the local reactive dynamics. Equivalently, we can ask what would happen in a spatial region if we were to isolate it from the rest of the system. The properties of that notional isolated region, e.g. the linear stability of the homogeneous steady state in it, serve as proxy for the regional dynamics in the full system. The regional properties depend on the regional average mass which is redistributed between regions by diffusion. Taken together, just as the local equilibria scaffold the interface, we can think of the regional “attractors” as scaffold for the global pattern. The properties of the full pattern can be pieced together by (characteristically distinct) isolated regions (plateaus and interface).

Let’s compare this decomposition into spatial regions with a typical Fourier-mode based (Galerkin expansion) approach. There, patterns with an interface width small compared to the system size require a large number of (nonlinearly coupled) modes to be taken into account. Hence, such patterns fall into the so called “strongly nonlinear regime” where an approach based on mode-coupling becomes unmanageable. Consequentially, studies based on mode-coupling methods in general provide insight only for pattern formation close to a supercritical onset that can be described by a narrow band of (weakly coupled) modes.

In contrast, in our phase-space geometric approach, the nonlinear kinetics is encoded by the nullcline shape. The internal properties of the spatial regions are determined by *regionally linear* properties of phase space flow. We will therefore refer to this as *method of regional phase spaces and regional attractors*. In this approach, the interface position – determining the global spatial structure – can be pictured as a collective degree of freedom. A conceptually similar, but technically more involved approach to study interfaces (also called ‘internal layers’) and their dynamics is singular perturbation theory (specifically matched asymptotic expansion) where one uses an asymptotic separation of spatial scales, see e.g. Ref. [80] and references therein. Such methods also facilitate a phase-space geometric analysis [23].

VI. THE REACTIVE NULLCLINE DETERMINES THE EXCITABILITY THRESHOLD

Before we delve into the more technical analysis of bifurcation structures, we would like to discuss one more important aspect of pattern formation: excitability, i.e. the ability to transition from one stable attractor (homogeneous steady state) into another one (stationary pattern) by a large enough perturbation. Excitability is a particularly important aspect of two-component McRD systems, because, as we have shown above, these systems generically have regions of multistability. Furthermore, biologically it is often desirable to be able to form a pattern following an external or internal signal that exceeds a certain threshold. As of yet, this threshold could only be determined numerically [40]. In the following, we will show how simple heuristic reasoning – based on *regional* lateral instability – yields a geometric criterion for the excitability threshold in (m, c) -phase space.

As we have shown in the previous section, the hallmark of a stationary pattern is a laterally unstable region surrounding the pattern inflection point x_0 (even if the homogeneous state of the system is laterally stable). In the proposed framework, the phase-space dynamics are simply represented by the expansion of the system in (m, c) -phase space due to mass redistribution. Hence, to lead to a stationary pattern, a trajectory in the (high-dimensional) phase space of a partial differen-

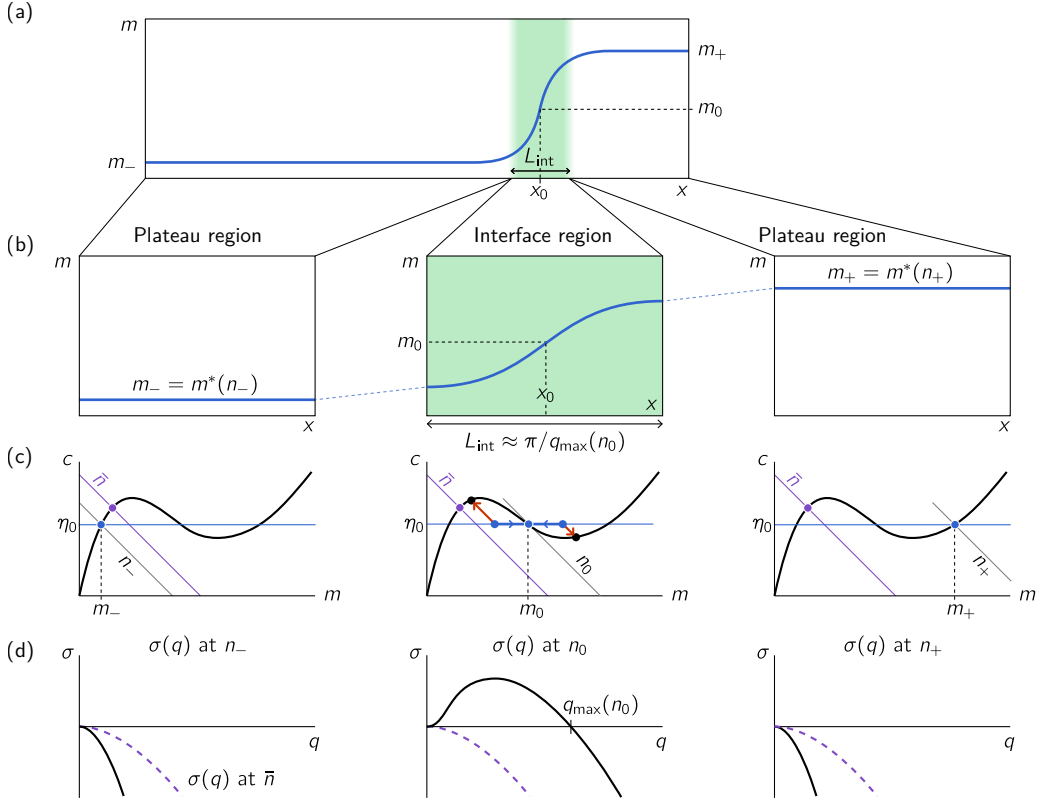


FIG. 9. Decomposition of a stationary pattern (a) into spatial regions that correspond to (m, c) -phase-space regions in the vicinity of landmark points. (b) Three characteristic spatial regions of the pattern (plateaus and the interface) can be notionally isolated. (c) The average total density in each of the regions (n_- , n_0 , and n_+) determines a different chemical equilibrium via the respective reactive phase space. (d) Linearization of the reaction-diffusion dynamics around these equilibria yields regional dispersion relations revealing the properties of the regions: The plateaus are laterally stable regions — anti-coarsening is not possible. On the other hand, the interface region is always laterally unstable, even if the global homogenous steady state (\bar{n}) is laterally stable. In particular, the interface width can be estimated by the marginally stable mode $q_{\text{max}}(n_0)$ at the right-hand edge of the dispersion relation of the interface region: $L_{\text{int}} \simeq \pi/q_{\text{max}}(n_0)$. The dashed lines show the dispersion relation of the homogenous steady state \bar{n} .

tial equation (PDE) must enter and remain in a (linearly) laterally unstable region in (m, c) -phase space (shaded in green in Fig. 10). The laterally unstable region in (m, c) -space corresponds to a respective region in real space. If the homogenous state is laterally stable then a finite perturbation is required to create a laterally unstable region. Let us study a prototypical perturbation able to induce a laterally unstable region: a step function that represents moving a ‘block’ of protein mass (total density) from one end of the system to the other; for an illustration of the spatial perturbation and the resulting flows in phase space see Fig. 10. Generalization to other perturbations is straightforward and based on analogous arguments. Such perturbations can be created by various means of ‘active’ mass redistribution, e.g. active transport in the cell cortex, along microtubules, and hydrodynamic cytosolic flows; see for instance [73].

Following a (large amplitude) perturbation, there are two distinct processes that are triggered in phase space

as shown in Fig. 10. On the one hand, in the laterally unstable region (green shaded area), a mass-redistribution instability will start to form a pattern, thus further amplifying the perturbation. On the other hand, because the perturbation shifts the regional chemical equilibria (black disks), there will be reactive flows (red arrows) in the regions that induce a cytosolic gradient which leads to mass redistribution between the regions by cytosolic diffusion (large blue arrows). If the cytosolic density in the laterally stable region is lower than in the laterally unstable one, the regional instability may not be sustained and the system returns to homogenous steady state (Fig. 10(b)). Conversely, if the cytosolic density is lower in the laterally unstable region than in the laterally stable region, then the cytosolic flow between the regions (blue arrow) will sustain the regional instability (Fig. 10(c)). Because the mass-redistribution instability creates a self-organized and self-sustaining cytosolic sink, the laterally unstable region can be self-sustained. The

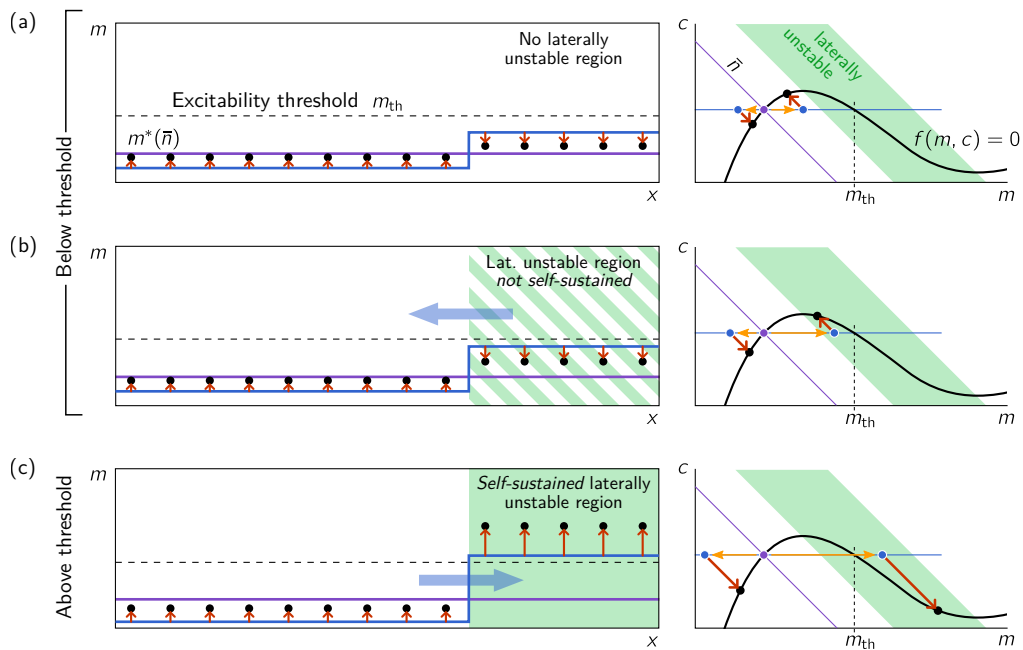


FIG. 10. Subcritical stationary patterns can be induced by perturbations above a threshold that can be heuristically estimated from the reactive nullcline. (a) After a small perturbation (blue profile, yellow arrows in phase space), that does not induce a laterally unstable region, the system returns to its uniform steady state (purple line). (b) A perturbation that creates a laterally unstable region, but does not cross the nullcline. Because the cytosolic concentration is lower in the laterally stable region, mass-redistribution (illustrated by the blue arrow) will disband the laterally unstable region. (c) A perturbation that crosses the nullcline will not only induces a laterally unstable region but also shifts the cytosolic equilibria such that the lateral instability is (self-)sustained by mass redistribution from the stable into the unstable region (blue arrow).

heuristic criterion for a (self-)sustained laterally unstable region is that the perturbation must cross the nullcline (see Fig. 10(c)). Then, the overall cytosolic concentration in the laterally unstable region is decreased by reactive flows (red arrows) such that cytosolic diffusion (blue arrow) between the regions will sustain the laterally unstable region.

Strikingly, this simple criterion already provides a very good approximation for the excitability threshold in comparison to full numerical simulation; see Appendix H, where we study the excitability threshold in a two-parameter family of perturbations. We conclude that the reactive nullcline provides the key information for understanding pattern formation dynamics, in a similar way as for the characterization of stationary patterns (Sec. V and the analysis of the linear mass-redistribution instability (Sec. III D)). Specifically it enables one to estimate the basins of attraction of the uniform steady state and the polarized pattern. We further learned, that regional lateral instability underlies excitability of laterally stable homogeneous steady states.

The threshold estimate provided here might help to understand nucleation of patterns from laterally stable homogeneous steady states. The unstable peak/trough patterns (dashed red lines in Fig. 8 are part of the separatrix between to the basin of attraction of stable stationary patterns, and can be pictured as canonical critical nu-

cleus [81]. The peak approximation described in Sec. V B and compared to numerical continuation in Appendix G provides a simple estimate for this critical nucleus.

VII. COMPLETE BIFURCATION STRUCTURE

Bifurcation diagrams of two-component McRD systems have previously been studied for specific choices of the reaction kinetics $f(m, c)$ using numerical methods [56]. Furthermore, based on numerical studies of various models, it was hypothesized that there might be a general bifurcation scenario underlying cell polarity systems [43]. Here we use the insight gained on phase-space geometry to systematically build the complete general bifurcation structure of two-component McRD systems. Our findings generalize previous results and unify them in the context of phase-space geometry. For large system size, the bifurcation structures are fully determined geometrically. We illustrate the effect of finite system size using numerically computed bifurcation diagrams shown in Appendix F.

Above, we studied the bifurcation diagram of stationary patterns for the bifurcation parameter \bar{n} in a system with monostable kinetics; see Sec. V C and Fig. 8 therein. Recall, that in large systems ($L \rightarrow \infty$), the bifurcation points in \bar{n} can be found based on geometric reasoning

in phase space: (i) Lateral instability is identified by a criterion on the nullcline slope: $\chi(\bar{n}) < -D_m/D_c$. Hence, the range of lateral instability is bounded by points n_{lat}^\pm where the FBS is tangential to the NC: $\chi(n_{\text{lat}}^\pm) = -D_m/D_c$. (ii) FBS–NC intersection points $m_\pm(\eta_0^\infty)$ provide the scaffold for the plateaus of mesa patterns, where the FBS-position, η_0^∞ , is determined by total turnover balance, Eq. (42). Mesa patterns exist as long as the average total density can be distributed between two plateaus n_\pm^∞ , i.e. in the range $n_-^\infty < \bar{n} < n_+^\infty$; recall that $n_\pm^\infty = n_\pm(\eta_0^\infty)$ depend on the position η_0^∞ and slope $-D_m/D_c$ of the FBS (cf. Eq. (44)).

Both of these geometric bifurcation criteria depend on the diffusion constants via the slope of the flux-balance subspace $-D_m/D_c$. We keep D_m fixed (thus fixing the smallest characteristic length scale $\ell = \sqrt{D_m/f_m}$ where spatial structures can be maintained against membrane diffusion (cf. Fig. 3(f)) and vary D_c to rotate the FBS in (m, c) -phase space.

A. Generic bifurcation structure of stationary patterns for monostable reaction kinetics

We construct the (\bar{n}, D_c) -bifurcation diagram by inferring n_{lat}^\pm and n_\pm^∞ , as described above, as functions of D_c . Qualitatively, this can even be done manually with pen and paper in the spirit of a graphical construction (see e.g. Ref. [1]) based on the geometric criteria (i), (ii) above, as shown in Fig. 8. Figure 11(a) shows the qualitative structure obtained by this graphical construction. A quantitative construction of the bifurcation diagram can be performed with simple numerical implementation of the bifurcation criteria described above, e.g. in Mathematica (see Supp. File: `flux-balance-construction.nb`, and Fig. 23 for figures of quantitative bifurcation structures). As we will see in the following, the structure of the bifurcation diagram is qualitatively the same for all monostable, N-shaped nullclines, independently of the details (nonlinearities and kinetic rates) of the reaction term $f(m, c)$. The bifurcation diagram is qualitatively different when the nullcline has a section of bistability (where $\chi < -1$, cf. Fig. 1). We will analyze this case and in particular the role of bistability further below in Sec. VII B.

As D_c is decreased, the flux balance subspace becomes steeper, and thus the bifurcation points n_{lat}^\pm and n_\pm^∞ start to converge (see Fig. 11; cf. Fig. 8). They meet in the inflection point of the reactive nullcline, n_{inf} , where the nullcline slope, χ_{inf} , is extremal ($\partial_n \chi|_{n_{\text{inf}}} = 0$). The extremal nullcline slope at the nullcline inflection point determines the minimal cytosolic diffusion constant,

$$D_c^{\text{min}} := \frac{D_m}{-\chi(n_{\text{inf}})}, \quad (47)$$

above which there are three FBS–NC intersection points. When the ‘critical’ point $(n_{\text{inf}}, D_c^{\text{min}})$ is traversed in D_c -direction, the FBS–NC intersections bifurcate in a (su-

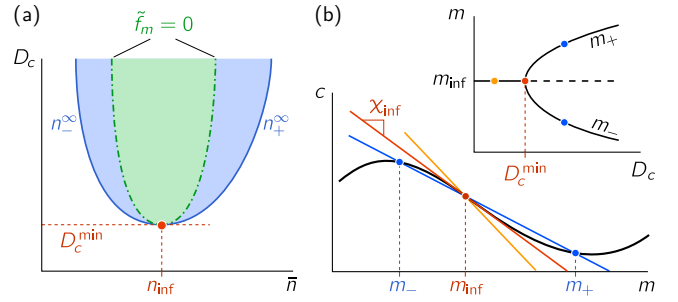


FIG. 11. (\bar{n}, D_c) -bifurcation diagram of stationary patterns for a system with monostable kinetics (same color code as in Fig. 8). (a) The bifurcation diagram for a large system ($L \rightarrow \infty$) is obtained by tracking the geometrically constructed bifurcation points n_{lat}^\pm and n_\pm^∞ as D_c , and thus the slope and position of the FBS, are varied (cf. Fig. 8). The onset of lateral instability (Turing bifurcation shown as green dash-dotted line) is generically subcritical since there exist stationary patterns outside the range of lateral instability ($n_{\text{lat}}^-, n_{\text{lat}}^+$); in the blue regions, the system is multistable (both the stationary patterns and the homogenous steady state are stable). The scaffolds for the low and high density plateaus (n_\pm^∞) bifurcate supercritically from the homogenous steady state at the critical point $(n_{\text{inf}}, D_c^{\text{min}})$ (red point). (b) The critical point in the (\bar{n}, D_c) -bifurcation diagram corresponds to the inflection point of the nullcline n_{inf} , where the nullcline slope $-f_m/f_c$ reaches its extremal value χ_{inf} and thus determines the minimal cytosolic diffusion D_c^{min} (cf. Eq. (47)). At D_c^{min} , the scaffolds of the plateaus, m_\pm , bifurcate in a supercritical pitchfork bifurcation from the nullcline inflection point m_{inf} (see inset).

percritical) pitchfork bifurcation; see Fig. 11(b). Since the FBS–NC intersection points m_\pm are the scaffolds for the plateaus (in short: *plateau scaffolds*; cf. Fig. 2), this bifurcation at the critical point $(n_{\text{inf}}, D_c^{\text{min}})$ is a bifurcation of the scaffold itself. Importantly, the actual pattern is bounded by the plateau scaffolds. Thus, if there are no plateau scaffolds (i.e. only one FBS–NC intersection point), there cannot be stationary patterns. For $L \rightarrow \infty$, patterns emerge slaved to the plateau scaffold, such that the pattern bifurcation is supercritical at the nullcline inflection point ($\bar{n} = n_{\text{inf}}$). Away from the nullcline inflection point ($\bar{n} \neq n_{\text{inf}}$), the lateral instability bifurcation is always subcritical for $L \rightarrow \infty$ because the range (n_-^∞, n_+^∞) where patterns exist always exceeds the range $(n_{\text{lat}}^-, n_{\text{lat}}^+)$ of lateral instability, as we have learned above in Sec. V C (cf. Fig. 8).

As we will see below in Sec. VIID, for finite L , the bifurcation is supercritical in the vicinity of the nullcline inflection point. The transition from super- to subcriticality depends on a subtle interplay of diffusive and reactive flow together with geometric factors like nullcline curvature.

Interestingly, the regimes and their interrelation in the (\bar{n}, D_c) -bifurcation diagram, as shown in Fig. 11(a), are phenomenologically similar to the phase diagram of (near equilibrium) phase separation kinetics for binary

mixtures, described by Model B / Cahn–Hilliard equation [65]. In fact, mathematical relations between two-component McRD systems and models for phase separation have been found for specific forms of the reaction term $f(m, c) = c - g(m)$; see e.g. Refs. [47, 52]. Furthermore, using the amplitude equation formalism, a mapping from two-component McRD models to Model B has been found for the vicinity of the critical point [82], where the pattern emerges from the Turing bifurcation in a supercritical or weakly subcritical pitchfork bifurcation (Fig. 11(b), cf. Sec. VIID below).

Strikingly, our geometric reasoning shows that the physics implied by the bifurcation diagram is the same as in phase separation kinetics (binodal and spinodal regimes) for all N -shaped nullclines, and far away from the critical point. This includes also cases where a mathematical equivalence of the underlying dynamics (e.g. in terms of a mapping to gradient dynamics) has not yet been found. This suggests that there might be a deeper connection between two-component McRD systems and (near equilibrium) phase separation kinetics. We elaborate on this promising outlook in the discussion in Sec. VIIB 1.

B. Locally bistable kinetics

Changing the kinetic rates deforms the nullcline shape. When the nullcline slope becomes smaller than -1 , a bistable section emerges (cf. Fig. 1).

1. Fronts in bistable media

To elucidate the role of bistability, let us first consider the case of equal diffusion constants $D_c = D_m =: D$. (Although this does not make sense in the intracellular context anymore, where typically $D_c > D_m$, we stick to the notation with concentrations m and c .) Then mass redistribution decouples from the kinetics $\partial_t n = D \nabla_x^2 n$, i.e. the total density becomes uniform by diffusion (see the mass-redistribution dynamics, Eq. (12), and note that $\eta(x, t) = n(x, t)$ for equal diffusion constants). As a consequence, the system can be reduced to one component, for instance the membrane density

$$\partial_t m = D \nabla_x^2 m + f(m, \bar{n} - m), \quad (48)$$

where the local kinetics is bistable at every point in space (Fig. 12). This corresponds to a (classical) one-component model for bistable media which generically exhibits propagating fronts [3]. A standard calculation, commonly performed by ‘Newton mapping’ (briefly described in Sec. IIIC) or by phase-space analysis (in $(m, \partial_x m)$ -phase space), shows that the propagation velocity v of a front is proportional to the imbalance in reactive turnover [3]: $v \propto \int_{m_-}^{m_+} dm f(m, \bar{n} - m)$. Hence, a stationary front can only be realized by fine-tuning of

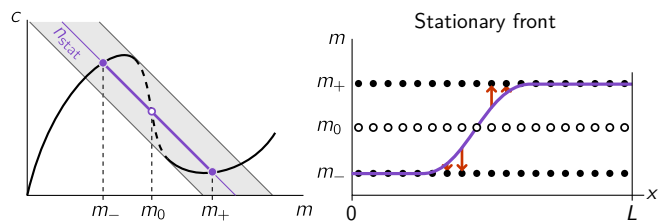


FIG. 12. Phase-space structure for bistable local kinetics in the case of equal diffusion constants, $D_m = D_c$, where there is no mass redistribution such that the system can be reduced to a one-component system, Eq. (48). The stable equilibria m_{\pm} form a *static*, spatially homogenous scaffold; the equilibrium m_0 is locally unstable. Only if the local kinetics are fine-tuned such that the total turnover vanishes (e.g. by tuning $\bar{n} = n_{\text{stat}}$), the front is stationary (marginally stable).

parameters, e.g. the average total density \bar{n} , such that total turnover is balanced:

$$n_{\text{stat}} : \int_{m_-}^{m_+} dm f(m, n_{\text{stat}} - m) = 0. \quad (49)$$

The balanced (fine-tuned) case corresponds to Allan–Cahn (also called ‘model A’ dynamics [83]). (In a finite size system, there will be exponentially slow coarsening, see Ref. [80] and references therein.)

With respect to the concept of local chemical equilibria as scaffolds for patterns (cf. Sec. IIIC), the bistable local chemical equilibria (fixed points m_{\pm}) can be regarded as a *static scaffold* for front solutions; see Fig. 12. Because there is no mass-redistribution, the scaffold must remain static and can not adapt to balance the total reactive turnover. Instead, fine-tuning of parameters (e.g. \bar{n}), is required to obtain a balance of total turnover and thus a stationary front. In the (\bar{n}, D_c) -bifurcation diagram, Fig. 13(a), the stationary bistable front with a static scaffold appears only at a singular point $(\bar{n}, D_c) = (n_{\text{stat}}, D_m)$.

What happens when the diffusion constants are unequal $D_c \neq D_m$? Then, mass will be redistributed, leading to shifting of the local equilibria that scaffold the pattern. As we know from our analysis for monostable reaction terms, this dynamic scaffold is able to self-balance the total reactive turnover — fine-tuning of \bar{n} is no longer required to obtain stationary patterns. Interestingly, for a bistable reaction term, stationary patterns can be constructed both for $D_m > D_c$ and for $D_m < D_c$, as we discuss next; see Fig. 13(b,c). To determine the stability of these patterns, we will examine below (after the description of the bifurcation diagram) how the scaffold self-balances via mass redistribution.

2. Bifurcation diagram for locally bistable reaction kinetics

The bifurcation diagram, Fig. 13(a), for the large system size limit ($L \rightarrow \infty$) is obtained using the same geo-

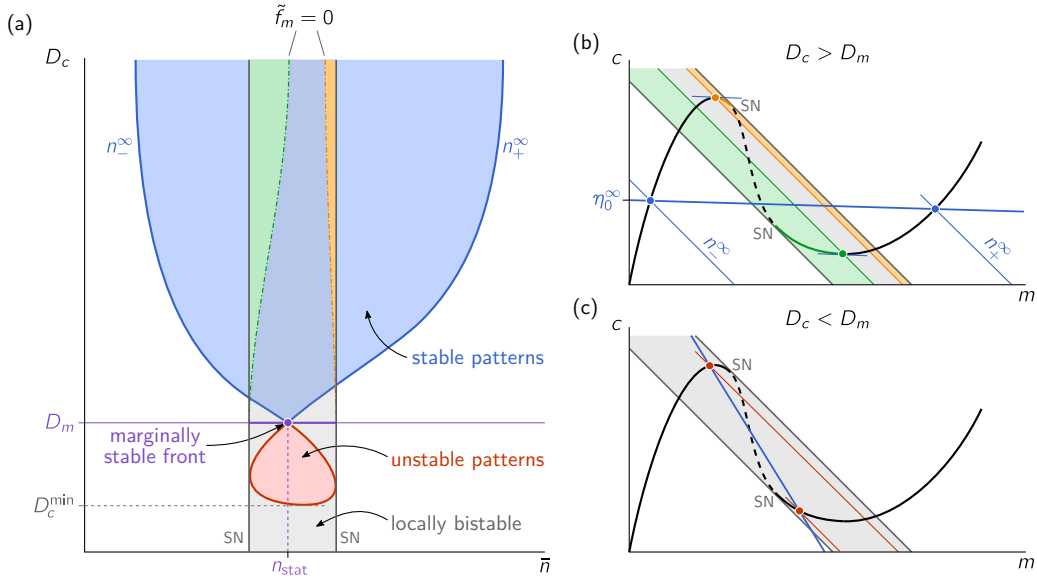


FIG. 13. Geometrically determined, schematic (D_c, \bar{n}) -bifurcation diagram in the large system size limit for a system with bistable kinetics (the locally bistable region is shaded in gray in both the bifurcation diagram (a) and the phase-space plots (b)). (a) Bifurcation diagram: the regions where stationary patterns exist (shaded in red and blue) and where a homogenous steady state is laterally unstable (shaded in green and orange) are constructed based on the same geometric criteria as in the case of monostable kinetics (cf. Fig. 8). Along the purple line $D_c = D_m$ there is no mass redistribution, and the system exhibits classical traveling fronts within the bistable regime (cf. Fig. 12). A marginally stable front exists at the singular point at $(D_c = D_m, n_{\text{stat}})$ where total reactive turnover is balanced by fine-tuning \bar{n} (cf. Eq. (49)). Outside the regions shaded in red and blue, there are no *stationary* patterns. There might however be non-stationary patterns like the traveling fronts in the bistable medium for $D_c = D_m$. Non-stationary patterns for $D_c \geq D_m$ are outside the scope of this study. (b) Phase-space plot showing the reactive nullcline (black line, dashed in the locally unstable region). The sections of the nullcline where homogenous steady state is laterally unstable (shaded in green and orange) are delimited by points where the FBS is tangential to the NC. Intersection points (blue dots) of the flux-balance subspace (thick blue line) with the reactive nullcline determine the range n_{\pm}^{∞} where stationary patterns exist. (c) Phase-space plot for the case $D_c < D_m$, where the slope of the FBS (thick red line) is steeper than -1 . The plateau scaffolds of stationary patterns can be constructed via FBS-NC intersection points (red dots), as long as $D_c > D_c^{\text{min}}$ (cf. Eq. (47)). These patterns are unstable though (cf. Eq. (50)).

metric criteria as for the case of locally monostable reaction kinetics (see Fig. 13(b), cf. Fig. 8(a)). The presence of a bistable nullcline section does not affect the feasibility of the geometric construction itself. However, the bifurcation diagram one obtains is qualitatively different from the monostable case, as we will see next. We discuss the regimes of stationary patterns (shaded in blue and red) first, before we analyze the regions of lateral instability (shaded in green and orange).

The region where stable stationary patterns exist (shaded in blue) is delimited by lines $n_{\pm}^{\infty}(D_c)$. These lines converge in singular point (n_{stat}, D_m) , where a marginally stable front exists in a bistable medium without mass redistribution, as we have studied above in Sec. VII B 1. Along the purple line, $D_c = D_m$, the dynamics can be reduced to a classical one-component system (cf. Eq. (48) and Fig. 12). It exhibits propagating waves within the region of bistability located between the two saddle-node (SN) bifurcations of local equilibria (gray area in Fig. 13(a)); compare the bistable (gray) area in Fig. 12 and Fig. 13(b,c), where the nullcline slope is steeper than -1 . Only for the fine-tuned value right

at $\bar{n} = n_{\text{stat}}$, the front velocity is zero (purple dot). At (n_{stat}, D_m) , the dynamic scaffold that self-adapts via mass redistribution for $D_c \geq D_m$ bifurcates from the static scaffold $m_{\pm}(n_{\text{stat}})$ of the marginally stable front.

For bistable kinetics the slope at the inflection point of the nullcline, χ_{inf} , is necessarily steeper than -1 so stationary patterns may also exist for $D_c^{\text{min}} < D_m$ (cf. Eq. (47)), since they can be constructed from FBS-NC intersection points as shown in Fig. 13(c). (We stick to the notation with concentrations m and c , although they are not meaningful as “membrane” and “cytosolic” concentrations, in the case $D_c < D_m$. Instead they should be understood as abstract concentrations [84]. The corresponding region where such stationary patterns exist is shaded in red in the bifurcation diagram shown in Fig. 13(a). In the bottom half of this “balloon”-shaped region the equilibria that form the plateau of the constructed pattern are locally unstable. Hence these patterns cannot be stable. As we will see in the next subsection, *all* stationary patterns for $D_c < D_m$ are unstable (even if their plateaus are locally stable) since they are destabilized by the imbalance of reaction turnover in-

duced by any (infinitesimal) perturbation. In contrast, stationary patterns for $D_c > D_m$ are stable because the self-adapting scaffold re-balances the reactive turnover.

The regions with a laterally unstable homogeneous steady state (NC-slope steeper than FBS-slope, cf. Eq. 25) are shaded in green and orange to distinguish in the bistable region which of the two locally stable chemical equilibria is laterally unstable; see Fig. 13(b) [85].

In conclusion, we found the generic (\bar{n}, D_c) -bifurcation diagram of stationary patterns for an N-shaped nullcline with a bistable section using the same geometric arguments as for the case of a monostable nullcline. Since our analysis crucially relies on the flux-balance subspace, it is limited to stationary patterns. For the special case $D_c = D_m$ the existence of non-stationary patterns (traveling fronts) in the locally bistable regime is well known. By continuity, we expect that there will be traveling fronts also $D_c \neq D_m$. Furthermore, we speculate that there will be non-stationary patterns outside the regime of local bistability, because mass redistribution may dynamically create a *region* of bistability that travels through the system.

3. The dynamic scaffold self-balances by shifting the flux-balance subspace

In the following, we will assess the stability of the stationary (mesa) patterns found by the geometric construction above. (We only discuss the stability of mesa patterns, which are generic in the limit of large system size, $L \rightarrow \infty$.) Our geometric framework allows a simple heuristic to study pattern stability. Instead of a full stability analysis of the stationary pattern, we consider only the stability of the FBS-position (mass-redistribution potential $\eta(x, t)$), as a proxy for the pattern stability. Intuitively, in the direction along the FBS, the pattern is stabilized by scaffolding. In the following we present a simple stability criterion for stationary patterns, derived from this intuition. Details of the (ad hoc) derivation and a comparison to numerics is presented in Appendix I. A mathematically rigorous stability analysis of stationary patterns (in particular using the ‘‘Singular Limit Eigenvalue Problem’’ introduced by [86], see [80] for a survey), is outside the scope of this paper.

Recall that in steady state $\tilde{\eta}(x) = \eta_0^\infty$ is spatially uniform and determined by total turnover balance, Eq. (17), that can be geometrically interpreted as a Maxwell construction (balance of the red-shaded areas in Figs. 2(b) and 14). How does the system evolve following a perturbation of the FBS-position η ? Consider a spatially uniform shift, $\delta\eta > 0$. Then the area between NC and FBS to the left of m_0 (inflection point of the pattern) will decrease, while the area on the right will increase; see Figs. 2(b) and 14. The net reactive flow (‘‘sum of the arrows in the two areas’’) leads to a change of the average concentrations m and c (in the interface region) which amounts to a shift of the FBS-position, as shown in

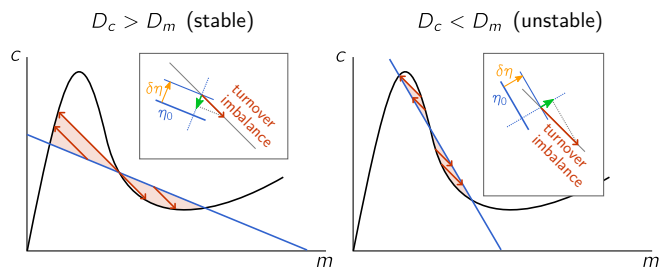


FIG. 14. Geometric construction of the stability of the FBS-position η_0 due to total turnover imbalance which serves as proxy for the stability of the pattern that is embedded in the FBS. In steady state, the reactive turnovers (illustrated by red arrows) on either side of the inflection point must be balanced. Inset boxes: A perturbation $\delta\eta$ (yellow arrow) that shifts the FBS-position η_0 will induce an imbalance of reactive turnovers (red arrow). Projecting this net reactive turnover onto the η -axis (dashed blue line) yields the movement of the FBS induced by the turnover imbalance (green arrow). For $D_c > D_m$, the FBS returns to its steady-state position η_0 . Conversely, for $D_c < D_m$, the FBS is driven further away from its steady-state position, such that the initial perturbation is further amplified in a destabilizing feedback loop.

the insets in Fig. 14. Because the net reactive flow points along a reactive phase space (slope -1), the direction in which the FBS shifts due to turnover imbalance depends on its slope. For $D_c > D_m$, i.e. a FBS-slope larger than -1 , it will move down and, hence, relax back to η_0^∞ (recall that we considered an upwards shift as perturbation, the arguments work analogously for a downwards shift). In other words, the scaffold will adapt until total reactive turnover is balanced again. We conclude that the scaffold is *self-balancing* when $D_c > D_m$. Conversely, when $D_c < D_m$, the FBS will move further in the direction of the perturbation, thus destabilizing the pattern.

This qualitative stability argument can be expressed mathematically, to obtain a quantitative approximation for the growth rate of perturbations $\delta\eta(x_0, t) := \eta(x_0, t) - \eta_0^\infty$ in the vicinity of a stationary mesa pattern $(\tilde{m}(x), \eta_0^\infty)$ (see Appendix I):

$$\partial_t \delta\eta(x_0, t) \approx \delta\eta(x_0, t) \frac{D_m/D_c - 1}{m_+ - m_-} \int_{m_-}^{m_+} dm \tilde{f}_\eta(m, \eta_0^\infty) \quad (50)$$

where $\tilde{f}_\eta = \partial_\eta \tilde{f}$. Comparison to numerically computed linear stability (dominant eigenvalue) of stationary patterns confirms shows that Eq. (50) is a good lowest order approximation for pattern stability; see Appendix I and Fig. 28. The integral over \tilde{f}_η is the turnover imbalance due to a shift of the FBS, and thereby captures the geometric intuition based on the ‘Maxwell construction’ (area balance) we outlined above. The prefactor $(D_m/D_c - 1)$ determines the direction in which FBS will shift because the integrand is always positive for $f_c > 0$ ($\tilde{f}_\eta(m, \eta_0^\infty) = f_c(m, \eta_0^\infty) - m D_m/D_c > 0$). We hence recover the stability criterion from our geometric argument above.

C. The cusp scenario is generic

It has been argued that bistability of the reaction kinetics is an essential prerequisite for polarization to emerge in two-component McRD systems [39, 40]. Recently, this claim has been questioned [87].

Above we have shown that bistability is not necessary for pattern formation. Instead, in systems with conserved quantities, a (non-homogeneous) pattern scaffold can generically self-organize by due to shifting chemical equilibria when there is mass-redistribution ($D_c \neq D_m$). However, there is an interesting and more subtle connection between bistability and the ability to form patterns. This connection is revealed by studying the transition from monostable to bistable kinetics due to variation of kinetic parameters.

Variations in the kinetic parameters will change the shape of the reactive nullcline. This may not only lead to quantitative but also qualitative changes in the (\bar{n}, D_c) -bifurcation diagram, namely if there is a transition from a monostable to a bistable reaction kinetics: Imagine that variation of some rate k in the reaction kinetics generates nullcline deformations as shown in Fig. 15(a). Let us start with a nullcline that is strictly monotonically increasing with m . Then according to the geometric criterion, Eq. (25), there is no lateral instability and hence no stationary patterns; recall that we showed in Sec. V A that an interface, the elementary element of a pattern, must be a laterally unstable region. Upon further changing the kinetic rate k there may eventually be a threshold value k_{saddle} beyond which the nullcline shows a region with a negative slope. A regime of lateral instability, and with it a regime where patterns can exist, emerges once the nullcline slope first becomes steeper than the slope of the FBS: $\chi_{\text{crit}} = -D_m/D_c$. Eventually, at $k = k_{\text{cusp}}$, a further deformation of the nullcline may create a section with slope $\chi < -1$ where there is bistability of local chemical equilibria. The bistable regime (shaded in gray) emanates in a cusp bifurcation where the two saddle-node (SN) bifurcations of chemical equilibria meet in a single point, and the nullcline inflection point has slope $\chi_{\text{inf}} = -1$ such that it is tangential to the reactive phase space $m + c = n_{\text{inf}} = n_{\text{cusp}}$; see Fig. 15(b). The surface of chemical equilibria in the two-parameter bifurcation structure starts to fold over itself at the cusp point. Because the Turing bifurcations lie on different sheets of the folded surface of local equilibria, The Turing-bifurcation line (dash-dotted green line) crosses over itself in the bistable region of the bifurcation diagram.

At the cusp point, the topology of the (\bar{n}, D_c) -bifurcation diagram changes from the topology characteristic for monostable reaction kinetics (leftmost panel in Fig. 15(c), cf. Fig. 11) to the one characteristic for bistable reaction kinetics (rightmost panel; cf. Fig. 13). At $k = k_{\text{cusp}}$, the bifurcation diagram has the singular topology shown in the center panel, with the cusp critical point at (n_{cusp}, D_m) .

Interestingly, by changing kinetic rates, the reactive

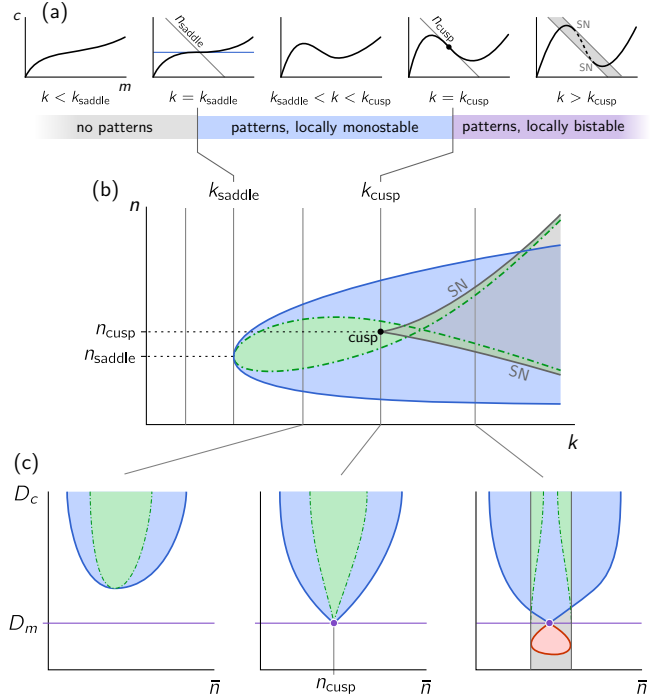


FIG. 15. Schematic of the cusp bifurcation scenario in (k, \bar{n}) -bifurcation diagram (same color code as Figs. 8, 11, and 13, Fig. 23). (a) We analyze the effect of a series of deformations of the reactive nullcline parametrized by the (notional) kinetic rate k . The respective (schematic) (k, \bar{n}) -bifurcation diagram of stationary patterns (for $D_m/D_c \rightarrow 0$ and $L \rightarrow \infty$) is shown in (b). Initially, the nullcline is monotonic, and hence does not facilitate pattern formation. At k_{saddle} a section of negative nullcline-slope emerges in a saddle point (slope $\chi = 0$ at the inflection point), such that patterns can form for $D_m/D_c \rightarrow 0$ (generally, the critical nullcline slope χ_{crit} is simply the ratio $-D_m/D_c$, cf. Eq. (47)). The regimes of lateral instability (green) and pattern existence (blue) emanate from this critical point. At k_{cusp} the nullcline has slope -1 at its inflection point, corresponding to a cusp bifurcation of chemical equilibria, where a region of bistability (shaded in gray, bounded by saddle-node bifurcations) emanates for $k > k_{\text{cusp}}$. At this point, the respective (\bar{n}, D_c) -bifurcation diagram (see (c)) transitions from the structure for monostable kinetics, Fig. 11(a), to the structure for bistable kinetics, Fig. 13(a). In the small gray triangular region in the top-right corner of the (k, n) -bifurcation diagram, the system is locally bistable but does not exhibit stable stationary patterns, because the reactive turnover is too asymmetric to be balanced by the the dynamic scaffold. (c) Schematic (\bar{n}, D_c) -bifurcation diagrams for $k_{\text{saddle}} < k < k_{\text{cusp}}$ (monostable kinetics, Fig. 11), at the cusp ($k = k_{\text{cusp}}$), and for $k > k_{\text{cusp}}$ (bistable kinetics, Fig. 13).

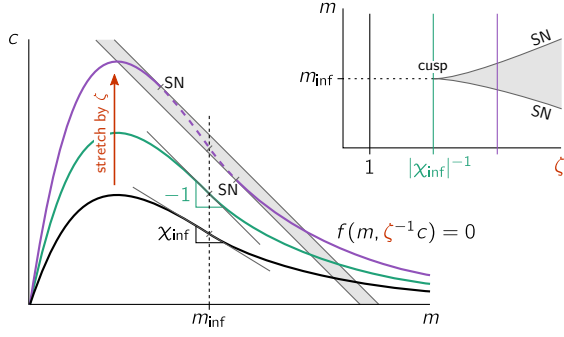


FIG. 16. Any nullcline with a section of negative slope can be deformed to exhibit cusp bifurcation where two saddle-node (SN) bifurcations of the chemical equilibria meet (see inset). The generic deformation to achieve this is a stretching in the c -direction by a factor ζ . To obtain this deformation, one replaces c in the reaction term $f(m, c)$ by $\zeta^{-1}c$, and obtains the stretched nullcline: $f(m, \zeta^{-1}c) = 0$. Say the original nullcline (black curve, $\zeta = 1$) has a slope $\chi_{\text{inf}} < 0$ at the inflection point m_{inf} . Then, the nullcline stretched by factor $\zeta = |\chi_{\text{inf}}|^{-1}$ (green curve), will have the slope -1 at the inflection point corresponding to a cusp point (see inset). When stretched further, the nullcline (purple curve) will have section with slope steeper than -1 (dashed section, region shaded in gray), where the chemical equilibria are bistable. Each of the three nullclines in the phase space corresponds a vertical line of the same color in the bifurcation diagram (inset).

nullcline of any system that is able to form stationary patterns, can be deformed to undergo such a cusp bifurcation of (local) chemical equilibria. To see how this works, first recall that to obtain stationary patterns, there must be a section where the nullcline slope is $\chi < -D_m/D_c < 0$, i.e. necessarily negative. This section can be deformed into a bistable region (slope $\chi < -1$) by a stretch of the nullcline in the c -direction in phase space; see Fig. 16. Let us denote the stretch factor by ζ , then the stretched nullcline is determined by $f(m, \zeta^{-1}c) = 0$. A slope χ of the original nullcline $f(m, c) = 0$ will become a slope $\zeta\chi$ for the stretched nullcline. Hence, a stretch factor $\zeta = |\chi_{\text{inf}}|^{-1}$ leads to a nullcline that has a slope -1 at its inflection point, hallmark of a cusp bifurcation (cf. Fig. 16). Any larger stretch factor leads to a bistable region (nullcline section with slope steeper than -1). We conclude that the generic bifurcation scenario underlying any pattern-forming two-component McRD system is a cusp bifurcation (Fig. 15). This result, obtained by geometric reasoning, explains previous numerical observations [43].

D. Sub- and supercriticality of lateral instability in finite sized systems

Up to now, we have focused on the large system size limit ($L \rightarrow \infty$) where bifurcation diagrams can be constructed from phase-space geometry. In particular, we

found that the onset of a mass-redistribution instability is generically subcritical. To analyze sub- vs. supercriticality in the case of finite system size, we use a perturbative approach (weakly nonlinear analysis, see e.g. [88]) for the pattern close to onset. In the vicinity of the homogenous steady state (m^*, c^*) , we expand a stationary state $(\tilde{m}(x), \eta_0)$ in harmonic functions (eigenmodes of the Laplace operator under no-flux boundary conditions):

$$\tilde{m}(x) = m^* + \sum_{k=0}^{\infty} \delta m_k \cos(k\pi x/L). \quad (51)$$

As we have learned in Sec. III D, the band of unstable modes always extends to long wavelengths ($q \rightarrow 0$) in a two-component McRD system ('type II' instability, cf. Fig. 3(b,f)). Therefore, in a finite size system, the mode that becomes unstable first at the onset of the lateral instability is the longest wavelength mode: $\cos(\pi x/L)$. We want to study the steady-state amplitude of this mode in the vicinity of the onset bifurcation. It is not sufficient, though, to keep only this first harmonic in the mode expansion, Eq. (51), since higher harmonics couple to it through the nonlinear terms. For an expansion to third order in the first mode amplitude δm_1 , one needs to include only the first and second harmonics in Eq. (51). Higher harmonics are not needed because they couple to δm_1 through higher nonlinearities $\mathcal{O}(\delta m_1^4)$. To leading order the ansatz thus reads

$$\tilde{m}(x) \approx m^* + \delta m_0 + \delta m_1 \cos(\pi x/L) \quad (52a)$$

$$+ \delta m_2 \cos(2\pi x/L), \quad (52b)$$

$$\eta_0 \approx \eta^* + \delta \eta_0, \quad (52c)$$

where (m^*, η^*) denotes the homogenous steady state: $\tilde{f}(m^*, \eta^*) = 0$. Using this ansatz in Eq. (14a) and keeping terms up to third order yields for the steady state pattern amplitude δm_1 (see Appendix J for details):

$$0 = F_1 \delta m_1 + F_3 \delta m_1^3 + \mathcal{O}(F_1 \delta m_1^3) + \mathcal{O}(\delta m_1^5). \quad (53)$$

The first order and third order coefficients read

$$F_1 = \tilde{f}_m - D_m \pi^2 / L^2, \quad (54a)$$

$$F_3 = \frac{\tilde{f}_{mmm}}{8} + \frac{\tilde{f}_{mm}^2}{24} \frac{L^2}{\pi^2 D_m} - \frac{\tilde{f}_{mm} \tilde{\partial}_m \sigma_{\text{loc}}}{4 \sigma_{\text{loc}}}, \quad (54b)$$

where $\tilde{\partial}_m = \partial_m - \frac{D_m}{D_c} \partial_c$ is the derivative tangential to the flux-balance subspace.

The first harmonic amplitude δm_1 , solution to Eq. (53) undergoes a pitchfork bifurcation at $F_1 = 0$. This bifurcation is simply the Turing bifurcation as it coincides with the onset of lateral instability: the homogenous steady state, $\delta m_1 = 0$, is laterally unstable only if the longest wavelength mode, $q_1 = \pi/L$, is within the band of unstable modes: $\pi^2/L^2 < q_{\text{max}}^2 = \tilde{f}_m/D_m$, i.e. if $F_1 > 0$ (cf. Eq. (54a)). Hence, the sign of the third order coefficient F_3 , evaluated at the bifurcation point $F_1 = 0$, determines whether the bifurcation is supercritical ($F_3 < 0$) or subcritical ($F_3 > 0$); see Fig. 17(b).

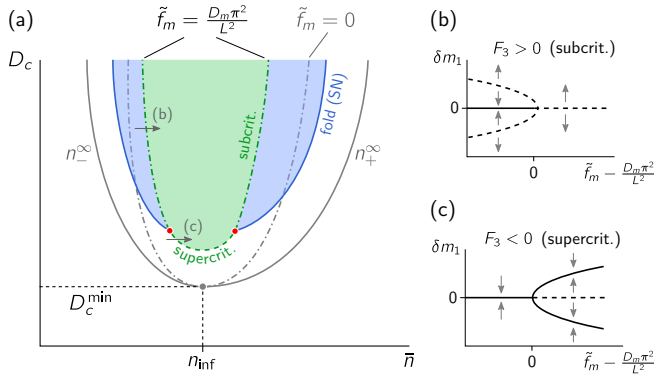


FIG. 17. Pattern bifurcation for finite domain size. (a) Schematic bifurcation structure for a system with monostable reaction kinetics (an analogous plot obtained by numerical continuation for a concrete reaction term, Eq. (A1*), is shown in Fig. 25, Appendix J). The gray lines indicate the bifurcation structure for $L \rightarrow \infty$ for comparison (cf. Fig. 11(a)). The Turing bifurcation (green dashed line, $\tilde{f}_m = D_m \pi^2 / L^2$) is supercritical in the vicinity of n_{inf} , i.e. the nullcline inflection point. In the vicinity of onset (small pattern amplitude δm_1) the third order coefficient, F_3 (cf. Eq. (54b)), of a weakly nonlinear expansion (cf. Eq. (52)), determines if the bifurcation is super- or subcritical. The schemata bifurcation diagrams (b) and (c), correspond to the small gray arrows in (a). Unstable patterns that emerge in a subcritical pitchfork bifurcation (see (b)) meet the stable patterns in a fold bifurcation (saddle-node of patterns, cf. Fig. 8). These fold bifurcations terminate in points where the lateral instability bifurcation switches from sub- to supercritical (red points), indicated by a vanishing third order coefficient $F_3 = 0$ in the weakly nonlinear expansion (cf. Eq. (53)). Along the line of supercritical lateral instability (dashed green line), stable patterns emerge directly in a supercritical pitchfork bifurcation; see (c).

On the basis of this weakly nonlinear analysis, we can study the bifurcation at $F_1 = 0$ in any control parameter μ (for instance the average total density \bar{n} , the system size L , kinetic rates, and diffusion constants). With the critical value μ_c , defined by the condition $F_1(\mu_c) = 0$, we introduce the reduced control parameter $\delta\mu = \mu - \mu_c$, and linearize Eq. (53) to lowest order in $\delta\mu$:

$$0 = \partial_\mu F_1|_{\mu_c} \delta\mu \delta m_1 + F_3(\mu_c) \delta m_1^3. \quad (55)$$

To leading order, the branch of the solution that bifurcates at $F_1 = 0$ then reads

$$\delta m_1 = \sqrt{\frac{\partial_\mu F_1|_{\mu_c}}{-F_3}} \delta\mu. \quad (56)$$

At singular points where local stability and lateral stability change simultaneously, i.e. $\sigma_{\text{loc}} = 0$ and $F_1 = 0$, the last term in F_3 diverges. Such codimension-two points require a more technically involved analysis (unfolding) that is outside the scope of this study (see e.g. [89, 90]).

From the third order coefficient F_3 (see Eq. (54b)), we can analyze the type of bifurcation in terms of geometric features (nullcline curvature $\kappa(n) \sim -\tilde{f}_{mm}|_n$, see

Appendix K) together with the quantity that characterizes the relaxation rate to chemical equilibrium (σ_{loc} , cf. Eq. (5)). The first two terms in F_3 encode geometric properties of the reactive nullcline (curvature and its rate of change), i.e. how the chemical equilibria shift as mass redistribution shifts the local phase spaces. The last term in F_3 represents the rate of change of the timescale for relaxation σ_{loc} to the chemical equilibria. In the following, we discuss the various regimes that arise due to the interplay of the three terms in F_3 . (To simplify notation, we will implicitly assume that all coefficients (\tilde{f}_m , etc.) in F_3 are evaluated at the bifurcation point μ_c .)

- (i) At the nullcline inflection point $\tilde{f}_{mm} = 0$, only the first summand of F_3 remains: $F_3 = \tilde{f}_{mmm} / 8$. The third derivative \tilde{f}_{mmm} is proportional to the rate of change of the curvature ($\tilde{f}_{mmm} \sim -\partial_m \kappa$, see Appendix K). The curvature of a typical N-shaped nullcline must be positive (bent upwards) to the right of the inflection point and negative (bent downwards) to the left of it, otherwise it is impossible to smoothly connect laterally unstable regions ($\tilde{f}_m < 0$) to laterally stable regions ($\tilde{f}_m > 0$). This implies that $\tilde{f}_{mmm} < 0$, and we conclude that the bifurcation at the nullcline inflection point is supercritical. This confirms our geometric argument above (cf. Fig. 11, and thin gray lines in Fig. 17).
- (ii) In the large system size limit ($L \rightarrow \infty$) away from the inflection point ($\tilde{f}_{mm} \neq 0$), the second term in Eq. (54b) dominates. Because this term is always positive, the Turing bifurcation in large systems is generically subcritical (cf. Fig. 17) as we have already concluded from geometric arguments in Sec. VC above.
- (iii) In a finite-sized but still large system, the last two terms of F_3 are negligible sufficiently close to the nullcline inflection point where \tilde{f}_{mm} vanishes. Hence, finite sized systems are supercritical in the vicinity of the nullcline inflection point, because \tilde{f}_{mmm} must be negative as we argued above in point (i); (cf. Fig. 17). Solving the condition $F_3 = 0$ to leading order in L^{-1} yields the estimate

$$|\tilde{f}_{mm}| < L^{-1} \sqrt{-\frac{3\pi^2}{2} D_m \tilde{f}_{mmm}}, \quad (57)$$
 for the range of supercriticality.
- (iv) In small systems, the transition from supercriticality to subcriticality will depend also on the last term in F_3 . It can contribute either positively or negatively to F_3 , depending on the details of the reaction kinetics.

Importantly, the statements (i)-(iii), regarding large systems, follow from purely geometric arguments as they are determined by the first two terms in F_3 . The reason for

this is that at large wavelength, chemical relaxation is fast compared to diffusion, so the pattern is slaved to the scaffold, i.e. the reactive nullcline. For the same reason, the long wavelength onset of lateral instability is determined by a geometric criterion (slope of the nullcline) as we showed in Sec. III D.

In conclusion, we comprehensively characterized the Turing bifurcation (sub- vs. supercritical) and the bifurcations of stationary patterns, using the (m, c) -phase-space geometry. Because of the inherent link between geometry and the physical concepts of mass-redistribution and shifting equilibria, we are able understand the physics underlying the patterns and their bifurcations. The bifurcations in the large system size limit ($L \rightarrow \infty$) — determined by geometry — provide a good starting point to study the bifurcations in a finite sized system, e.g. by numerical continuation (see Appendix F).

VIII. CONCLUSIONS AND DISCUSSION

In order to understand pattern-forming systems, two central questions need to be addressed: (i) Is the uniform steady state of the system laterally unstable for some parameter configurations? (ii) Does the system support stable patterns, and what are the properties of these patterns?

The first question can readily be answered by linear stability analysis. The ensuing eigenvalue spectra of the eigenmodes yield information regarding the growth or decay of infinitesimal perturbations. In contrast, the second question is intimately bound up with nonlinear dynamics, and is much more difficult to answer as one needs to understand the mechanism underlying the saturation of the growing modes. This saturation of the pattern amplitude might — but need not — occur at small amplitude due to weakly nonlinear coupling of modes. This case can be successfully addressed by employing weakly nonlinear analysis; see e.g. Refs. [62, 88]. In general, however, pattern amplitudes may become large even close to the onset of lateral instability, and solving the full nonlinear problem becomes analytically intractable in general. This behavior is characteristic for subcritical bifurcations, which are the rule rather than the exception, as we demonstrated here for the two-component McRD system.

Our results offer a unifying view of the two questions, as both initial pattern growth and stabilization (saturation) in an ultimate stationary pattern can be analyzed and characterized on the basis of the shape of the reactive nullcline and its intersections with the flux-balance subspace. This enables us to address many properties of the nonlinear dynamics directly in terms of phase-space geometry, which otherwise would only be accessible by numerical analysis. For instance, excitability thresholds, bifurcation diagrams, and characteristic pattern profiles can be directly read off from the shape of the nullcline.

In the following we will address new perspectives for the investigation of reaction–diffusion systems with con-

served masses. An important class of such systems are models for protein pattern formation, *in vivo* (intracellular) and *in vitro* (reconstituted systems).

In a broader context, reaction–diffusion systems are part of a large class of non-equilibrium systems that are able to form self-organized patterns. We found intriguing equivalences to two such systems — (non-)equilibrium phase separation and shear banding in complex fluids. We therefore believe that our framework offers a geometric perspective on these (and potentially other) non-equilibrium systems. Finally, we will give a brief outlook on upcoming work, on questions that are currently under investigation, and on future research directions.

A. Reaction–diffusion systems

For the sake of specificity, we will discuss the implications and application of our findings on mass-conserving reaction–diffusion systems with respect to protein pattern formation, which operates far from thermal equilibrium, and has received growing interest over the past two decades. Intracellular, i.e. *in vivo*, protein pattern formation and self-organization have been subject to a large body of research, both experimentally [73, 76, 91–100] and theoretically [35–39, 43, 44, 57, 75, 79, 87, 101–107]. Furthermore, the *in vitro* reconstitution of the MinDE system has made it possible to study protein pattern formation experimentally under a wide range of externally controllable conditions [108–113].

Taken together, these studies of both *in vivo* and *in vitro* systems have led to many important insights. However, many intriguing questions that are relevant to all reaction–diffusion systems far from equilibrium, remain open: What are the fundamental principles of pattern formation? What is the role of the (biomolecular) interaction network, and how can complex models be reduced to their essential components? How are different patterns and their wavelengths selected? In what follows, we discuss the implications of our work for such questions.

1. Model classification, network motifs and experimental accessibility

In recent years, several studies have employed high-throughput computational analyses of reaction–diffusion systems and graph theoretical analysis with the goal to infer the pattern-forming capabilities from the topology of the underlying reaction networks [114–117]. Our results offer a novel and complementary perspective on model classification and the role of the interaction-network topology for mass-conserving systems. We found a simple condition for the pattern-forming (mass-redistribution) instability in two-component McRD systems: The slope of the line of chemical equilibria (reactive nullcline) must be (sufficiently) negative. Broadly speaking, the chemical equilibrium of the faster diffusing

(i.e. cytosolic) component has to decrease with increasing total density (cf. Secs. III D and IV). Importantly, our approach goes beyond the classification based on linear (in)stability. It shows that the effect of nonlinearities on the dynamics is encoded in the curved shape of the nullcline. In particular, there is a direct connection between the nullcline shape and the characteristic spatial density profile of the pattern (cf. Sec. V B). The chemical equilibria, as represented by the reactive nullcline, might therefore provide an alternative approach to model classification. Hence, a key challenge for future research will be to study how specific kinetic interactions and model parameters affect the shape of the reactive nullcline.

Moreover, a major advantage of chemical equilibria as the essential criteria for model classification is their experimental accessibility. In principle, any line of chemical equilibria can be measured in experiments by using a single, isolated, and well-mixed reactor and externally controlling the available conserved quantity (e.g. particle number). Such experiments would allow one to probe and classify the core mechanism quantitatively without any knowledge of the molecular details (which are irrelevant for such a classification).

The concepts that we introduced — mass redistribution and shifting local equilibria — are not restricted to two-component systems with a single conservation law. They have previously been applied to the model of the (*in vitro*) MinDE system, which has two conserved protein species, MinD and MinE, and five components [28]. We believe that the results presented here point toward a more general picture that still has to be worked out. Our analysis constitutes the first step in a long-term project to find a geometric representation of the nonlinear dynamics of spatially extended systems. In the outlook, Section VIII C, we briefly describe various upcoming works and future projects that build upon the present study and generalize its results.

2. Polarity patterns, bistability and the necessary condition for Turing instability

Bistability is a generic feature of nonlinear systems, and its putative relation to polarity patterns has been critically discussed in the literature [39, 87, 103, 106]. In systems without mass conservation, bistability facilitates traveling fronts that connect the two stable chemical equilibria (homogeneous steady states). (This scenario appears in mass-conserving systems as the special case of equal diffusion constants, which entails the lack of lateral mass redistribution.) In our framework, the stable equilibria can be pictured as scaffold for the traveling front. Because the scaffold is static in systems without mass redistribution, fine-tuning is required to achieve a stationary front (cf. Sec. VII B 1). Our results show that, in mass-redistributing systems (unequal diffusion constants), the scaffold becomes dynamic and thereby supports stable polarity patterns in an extended param-

eter regime (cf. Sec. VII B). Most importantly, we found that, even in a monostable system, mass redistribution can facilitate the formation of a scaffold for polarity patterns. Hence, bistability is neither required nor sufficient for stable polarity patterns.

The necessary condition for a mass-redistribution instability is that the reactive nullcline in the phase space of chemical reactions must include a segment of negative slope (cf. Secs. III D and IV). More precisely, we have shown here that the slope must be more negative than the ratio of the membrane to the cytosolic diffusion coefficient, D_m/D_c . As membrane-bound proteins are significantly less mobile than cytosolic proteins, i.e. $D_m \ll D_c$, a small negative slope of the reactive nullcline is already sufficient for a Turing instability in the intracellular context. Recall also that the criterion for bistability is a slope that is steeper than -1 (cf. Sec. III A), which is obviously a more restrictive condition than that for lateral instability. Hence, a bistable region is generally surrounded by a larger region of lateral instability in parameter space (cf. Fig. 15).

One might wonder how generic nullclines with a segment of negative slope are. In fact, they are frequently encountered as N -shaped nullclines in a broad range of classical nonlinear systems [1, 2, 4, 18]. Typically, these nullclines encode some nonlinear feedback mechanisms that give rise to relaxation oscillations, excitability and bistability. From this perspective, it appears that they should be rather common in biological systems.

3. Subcriticality, pattern robustness, and length-scale selection

An important result of our analysis is that pattern-forming mass-redistribution instabilities are generically subcritical (cf. Secs. V C and VI D). This may be beneficial in a biological context, as it confers robustness: Once a pattern is established, it is robust towards parameter variations due to hysteresis [43, 73, 118]. However, it should be pointed out that well-known mathematical results for systems near a supercritical instability may well not apply for subcritical systems. Potentially the most prominent of such results is the existence of a *characteristic length scale*, determined by the fastest growing mode in the dispersion relation. This is often considered as a defining property of “Turing patterns”. However, for subcritical systems, the length scale of the pattern cannot be inferred from a linear stability analysis of the uniform steady state in general — not even at onset. Indeed, like some previous authors [35, 36, 44], we find that two-component models with mass conservation always show uninterrupted coarsening, i.e. the wavelength selected by the fastest growing mode at onset is observed only transiently. A geometric argument based on the framework presented here, which elucidates why uninterrupted coarsening is generic in two-component McRD systems, will be presented in an upcoming manuscript [32].

Note, however, that coarsening is not a generic feature of all mass-conserving systems. Actually, multicomponent McRD models show (multi-)stable patterns with finite wavelengths [28, 79]. We believe that identifying and understanding mechanisms of nonlinear wavelength selection that bring the coarsening processes to a halt and stabilize patterns with finite wavelength are among the most important tasks for future research on multicomponent models. While some rather general criteria have been found for one-component systems [119, 120], a comprehensive understanding of multicomponent systems remains out of reach for now.

4. Excitability

Subcriticality implies the existence of parameter regimes in which the system is excitable, i.e. where pattern formation can be triggered by sufficiently large perturbations. Excitability has been controversially discussed as a new mechanism (under the term “wave-pinning”) for pattern formation, which — it is argued — is distinct from a lateral (“Turing”) instability [39, 42, 87, 121].

We use the principle of mass redistribution on the scale of spatial regions to show how pattern formation can be induced by a perturbation that creates a (self-sustained) laterally unstable region, even if the homogenous steady state is laterally stable (cf. Sec. VI). Building on this insight, we have provided a simple geometric argument for the excitability threshold (“nucleation threshold”) based on the reactive nullcline.

Moreover, our results show that an interface — the elementary building block of a pattern — must necessarily be a laterally unstable region (cf. Sec. VA). Hence, the creation of a laterally unstable region is an essential condition for the formation of a steady-state pattern. Furthermore, any two-component system that has a regime of excitability, must also exhibit a regime where the homogenous steady state is laterally unstable, and this regime can always be reached by simply changing the average total density. We therefore conclude that linear instability and excitability are inextricably linked: there can be no excitability without linear lateral instability, and excitability can be pictured as a regional (linear) lateral instability.

5. Pattern types

In a biological system, the characteristic features of a pattern dictate the positional information it can convey, and therefore the biological function it can facilitate [57, 93, 122, 123]. For example, cell division in budding yeast (*S. cerevisiae*) requires the formation of a single, narrow polar zone, marked by a high density of the protein Cdc42, to uniquely determine the future bud site [91, 92, 97]. This requirement is met by a peak pat-

tern. Mesa-like patterns, in contrast, sharply separate two spatial domains. This is, for instance, a feature of PAR protein patterns in *C. elegans* [73, 74, 100, 107].

Another important difference between peak and mesa patterns is how they respond to changes in average total protein density, e.g. owing to up- or down-regulation of gene expression, or system size, e.g. due to growth. An increase in average mass makes peak patterns grow in amplitude, while for mesa patterns it leads to a shift in the interface position. Upon an increase in system size, peak patterns grow, because the total number of proteins in the system increases, while the relative interface position of mesa patterns remains unchanged. Hence, mesa patterns inherently scale with the system size — a property that is desirable in developmental systems.

Given the relevance of the pattern type (i.e. peak or mesa) for biological function, it would be useful to have general criteria that enable one to infer the pattern type from the underlying biochemical network. While direct inference from the network itself is in general not feasible, our analysis shows that the decisive characteristics can be obtained from the phase-space geometry. As described above, we have found such a geometric criterion based on the shape of the reactive nullcline and the ratio of diffusion constants, which is reflected in the slope of the flux-balance subspace. A mesa pattern is composed of two plateau regions, each characterized by an intersection of flux-balance subspace and reactive nullcline. In the case of a strongly asymmetric nullcline shape (e.g. nullclines that asymptotically approach the m -axis for large m ; see Figs. 7(b) and 19) and a shallow flux-balance subspace ($D_m/D_c \ll 1$), the second plateau is only formed when the average mass is sufficiently large. For lower densities, there are peak patterns instead. The approximation of the peak pattern amplitude provided in Sec. VB (details in Appendix G), provides a simple estimate of the average mass at which peak patterns transition to mesa patterns.

If the nullcline shape is more symmetric (see Figs. 2 and 7(a)), mesa patterns are generic, because the second plateau is already formed at low average mass. Stable peak patterns are possible, but require fine tuning of the average mass (see Fig. 8). The nullcline shape thus serves as a simple criterion that predicts the type of patterns formed by a two-component McRD system.

In a recent numerical study of two-component McRD models [44], a phenomenological “saturation point” was found to mark the peak- to mesa-pattern transition. Our geometric analysis has now revealed the phase-space structure that underlies this “saturation point”: it corresponds to an intersection point between reactive nullcline and flux-balance subspace; hence, its position is hence dictated by the nullcline shape. In Ref. [44], it was also found that mesa- and peak-patterns vastly differ in their rate of coarsening: mesas compete on a much slower timescale than peaks. In an upcoming work, we analyze the coarsening dynamics in terms of phase-space geometry and show that the different coarsening rates of

peak and mesa patterns are also a consequence of the nullcline shape [32].

B. Related non-equilibrium systems

Reaction–diffusion systems are part of a much broader class of systems that are able to form self-organized patterns. Many of these other systems also have conserved quantities. In the following, we will discuss two such systems that exhibit intriguing equivalences to two-component McRD systems. First, we elaborate on interesting analogies with phase separation in thermal and in active systems; recently, various non-equilibrium generalizations of the Cahn–Hilliard equation (which describes phase separation near equilibrium [61, 124]) have been investigated [66, 68]. Second, we discuss shear banding in complex fluids [125, 126]. Our geometric framework also offers a geometric perspective on these systems.

1. Connection to (non-)equilibrium phase separation

By means of the flux-balance construction on the reactive nullcline, we were able to find the generic bifurcation diagram for the two-component McRD system in the large system size limit (cf. Sec. VII). We found that the lateral instability bifurcation is generically subcritical (discontinuous). It is supercritical (continuous) only if the total density is fine-tuned exactly to an inflection point of the reactive nullcline (cf. Sec. VIID). For typical N-shaped nullclines, there is only a single inflection point, and therefore only a single supercritical point. Intriguingly, this point has characteristics similar to those of the critical point for phase separation of binary mixtures close to thermal equilibrium where binodal and spinodal lines meet. The dynamics of binary mixtures close to thermal equilibrium is described by the Cahn–Hilliard equation (also called Model B dynamics in the classification scheme by Hohenberg and Halperin [127]). A recent study shows that in the vicinity of the critical point (where the pattern amplitude is small) a systematic mapping from the two-component McRD system to the Cahn–Hilliard equation is possible using the amplitude equation formalism [82]. Whereas this mapping breaks down further away from the critical point, our geometric description is valid in general. Hence, our phase-space geometric analysis of the McRD system explains this finding and puts it into a broader context. In particular, it reveals that supercriticality at the critical point(s) is of geometric origin (i.e. results from nullcline inflection points, see Fig. 11(b)).

This phenomenological equivalence between McRD dynamics and Model B dynamics is quite remarkable, since the former is inherently far from thermal equilibrium, while the latter describes systems close to thermal equilibrium. In addition to their equivalent phase diagrams, there are further interrelations between these two dis-

tinct systems: As we discussed above in Sec. VIII A 3, it has been hypothesized that uninterrupted coarsening — a characteristic of equilibrium phase separation — is also generic for two-component McRD systems [35, 36, 44]. Indeed, for specific mathematical forms of the reaction term, uninterrupted coarsening has been proven mathematically [70, 71]. In an upcoming work [32], we will present an argument, using the phase-space geometric framework, that coarsening is generic in all two-component McRD systems.

Another interesting connection to equilibrium phase separation is the coarsening process itself: Phase-separated droplets near equilibrium coarsen via the Ostwald ripening process. Ostwald ripening can be understood as a mass-redistribution instability, the type of lateral instability that is at the heart of pattern formation in McRD systems. Our analysis suggests that droplets can be abstracted as local equilibria where the density outside the droplet is controlled by the total density in the droplet, i.e. the droplet size (cf. Fig. 5 in Sec. IV A). Gradients in the density outside differently sized droplets drive the Ostwald ripening in the same way as lateral (“Turing”) instability in a McRD system is driven by gradients in the fast-diffusing (cytosolic) component — both are mass-redistribution instabilities. Our analysis thus suggests that Turing instability is topologically equivalent to Ostwald ripening.

The equivalence between two-component McRD systems and phase separation near equilibrium (Cahn–Hilliard equation) outlined above raises the question whether there is a deeper (mathematical) connection? Phase separation dynamics near equilibrium is determined by the gradients in a free-energy landscape. Interestingly, for the special form, $f(m, c) = c - g(m)$, of the reaction term, an effective free-energy functional can be constructed [48, 52], which gives a gradient-flow structure to the reaction–diffusion dynamics with such a reaction term. Furthermore, in Ref. [52] it is also shown that these systems can be mapped to the Fix-Caginalp phase field model for non-isothermal solidification dynamics [51, 128]. Such phase-field models have in turn been related to the Cahn–Hilliard equation [61, 124] and the viscous Cahn–Hilliard equation [129], see e.g. Ref. [130].

The ensuing steady state (thermal equilibrium) of phase-separating systems can be found using a Maxwell construction, i.e. a common tangent construction on the bulk free-energy density. Interestingly, generalizations of the common tangent construction for non-equilibrium systems were introduced recently in Refs. [131, 132]. Instead of a mapping of non-equilibrium systems to an effective equilibrium description, one might ask whether our framework might facilitate the analysis of non-equilibrium generalizations of the Cahn–Hilliard equation. We believe that our phase-space geometric approach provides a complementary perspective on non-equilibrium systems that is not subject to the restrictions of a mapping to an effective thermodynamic language.

Instead, it is based on the concept of local equilibria and incorporates the principle of mass-redistribution instability, and the flux-balance construction, to characterize stationary patterns and their bifurcations.

A concrete example where such an alternative approach might prove useful involves phase separation kinetics in the context of active systems where detailed balance is broken. Recently, two such systems have been studied: First, active emulsions driven away from thermal equilibrium by chemical reactions were found to exhibit reversed Ostwald ripening [68]. Second, it was shown that local currents that break detailed balance can lead to microphase separation (interrupted coarsening) [66]. In both cases, these findings imply that nonlinear wavelength selection takes place in such systems. We speculate that a description in terms of a phase-space geometry framework as outlined in this manuscript might lead to new insights on the question of wavelength selection, as discussed briefly in the context on protein pattern formation in Sec. VIII A 3.

2. Topological equivalence with shear banding in complex fluids

Our phase space analysis also shows interesting equivalences between pattern formation in two-component McRD systems and shear banding in complex fluids. Complex fluids can exhibit a non-monotonic *constitutive* relationship $\Sigma(\dot{\gamma})$ between the total stress Σ and the (homogeneous) strain rate $\dot{\gamma}$ [125, 126]. When the total stress decreases upon an increase in strain rate, $\partial_{\dot{\gamma}}\Sigma < 0$, a mechanical instability results, which leads to a separation of a sheared fluid into “shear bands” with different viscosities and strain rates, which coexist at a common total stress. The “common total stress” construction on the *constitutive* curve $\Sigma(\dot{\gamma})$ employed to analyze this phenomenon (in a one-dimensional system) is analogous to our flux-balance construction on the reactive nullcline for two-component McRD systems (see Sec. III C), by means of a mapping $(n, \eta) \leftrightarrow (\dot{\gamma}, \Sigma)$ between the phase space variables. The total strain rate $\bar{\dot{\gamma}} = L^{-1} \int_0^L dx \dot{\gamma}$ is analogous to the average total density \bar{n} . The constitutive $\Sigma(\dot{\gamma})$ curve is analogous to the reactive nullcline. The steady state conditions are spatially uniform total stress and flux-balance (spatially uniform mass-redistribution potential; see III B) respectively. The selection of the common total stress generally depends on the details of the model [133], in particular on stress diffusion [134]. For simple models, it can be pictured similarly to a Maxwell-construction (cf. total turnover balance in a two-component McRD system illustrated in Fig. 2). Furthermore, strain-rate propagation due to stress gradients in complex fluids is equivalent to mass redistribution due to concentration gradients in McRD systems. Accordingly, the low Reynolds number limit is analogous to the $D_c \rightarrow \infty$ limit in the two-component McRD system.

Taking these analogies together, we conclude that

these physically distinct phenomena are topologically equivalent and can be studied with similar phase-space geometric tools. Such a connection might benefit both fields as more involved scenarios are investigated, e.g. coupling to additional degrees of freedom: For models of complex fluids, additional spatial dimensions [135] or coupling to internal structure of the fluid [136, 137] can lead to a variety of intricate spatiotemporal patterns; for mass-conserving reaction–diffusion systems, additional components or additional conserved species can equally lead to a broad range of phenomena [28, 79, 138]. Studying such systems in a phase-space geometric framework offers an exciting new perspective for future research.

C. Outlook — Generalization to systems with more components and more conserved species

The theoretical framework for two-component McRD systems developed here suggests several promising directions for future research. It offers means of tackling some remaining open questions regarding two-component McRD systems: What are the principles at work during the coarsening process of multiple high-density regions? What can we learn about pattern formation in heterogeneous systems (e.g. with spatial templates such as “morphogen” gradients)? What is the role of noise?

Moreover, it will be interesting to explore various avenues toward generalization to McRD systems with more components and conserved species, including applications to various specific physical and biological systems as outlined shortly below. The long-term perspective is a generalization toward a geometric theory of McRD systems. Below, we discuss some possible routes towards such a generalization in more detail. Ultimately, it may be fruitful to apply the concepts presented here to other non-equilibrium systems with conserved quantities, such as active-matter systems (see e.g. Refs. [139–148] for some recent studies and reviews) and (vibrated) granular media (see e.g. Ref. [149] for a review).

1. Two-component systems: coarsening dynamics, morphogen gradients, and noise

For two-component systems, we have comprehensively characterized elementary patterns with monotonic density profiles, i.e. a single interface. Going forward, a key task will be to investigate the nature of the coarsening dynamics of patterns with multiple interfaces in one and more spatial dimensions. Furthermore, we hypothesized that there might be a deeper connection (possibly a mapping) to near-equilibrium phase separation. These questions are currently under investigation and will be the subject of a future work [32].

On a different note, the approach of regional phase spaces is a promising tool with which to study two-

component systems in a heterogeneous spatial domain, where some external template (such as a “morphogen” gradient) guides pattern formation. By studying such heterogeneous systems, one can address the question of how self-organization may be controlled by spatiotemporal templates [34].

Another promising future direction of study is the role of noise in stochastic two-component McRD systems. Noise-induced phenomena in reaction–diffusion systems have previously been studied for models with (e.g. [38, 41]) and without conserved quantities (e.g. [150, 151]). Importantly, noise in reaction–diffusion systems is not constrained by the fluctuation-dissipation theorem, but must be inferred from the stochasticity of the chemical processes using path integral approaches [152].

2. Generalization to more complex phenomena

The two-component McRD system studied here has a comparatively simple phenomenology, exhibiting only steady states that are stationary (no oscillations) and no wavelength selection (uninterrupted coarsening). In a previous study [28], the concepts of mass redistribution and local equilibria have already been successfully employed to analyze a multicomponent multispecies McRD model (for MinDE *in vitro* pattern formation) that exhibits much more complex phenomena, like spatiotemporal chaos at onset and transition to order (standing and traveling waves). These phenomena, observed in numerical simulations, can be understood in terms of moving local equilibria. In particular, this study revealed intriguing, highly non-trivial, connections between the nonlinear pattern dynamics far from the homogeneous steady state and the dispersion relation that characterizes the linearized dynamics in the vicinity of the homogeneous steady state. However, these findings are model specific, and rely on numerical simulations. In contrast, the characterization of the two-component McRD systems presented here is independent of the specific model (reaction term) and enables us to predict the pattern formation dynamics from a simple graphical analysis, without the need to perform numerical simulations. The obvious next step is to generalize this level of understanding to more complex phenomena by studying three-component McRD systems. Such models have recently been employed to model various (bio-)physical phenomena in numerical studies [79, 138]. Studying these models in the mass-redistribution framework might reveal the principles underlying their dynamics and provide a good starting point for a generalization of the theory presented here.

For ODE dynamics, the seemingly small step from two to three variables increases the diversity of phenomena dramatically. We expect a similar situation for spatially extended systems. Note in particular that, with three components and one conserved quantity, the reac-

tive phase space will be two-dimensional, which allows for more complex local dynamics and attractors, such as limit cycle oscillations. A fully general study of three-component McRD systems will therefore probably not be possible from the outset. Instead we propose to focus on cases where a time-scale separation enables one to build on the results for two-component systems. For instance, one might study cases where the coupling to the additional third component is slow (the model investigated in Ref. [79] is of that form). This is a typical strategy in Nonlinear Dynamics; see e.g. Ref. [15] for an overview in the context of neural excitability.

3. Model reduction and classification

While multicomponent, multispecies models can exhibit complex phenomenology, as discussed above, this is not *necessarily* the case. For instance, cell polarization of eukaryotic cells is often brought about by a large number of interacting protein species. Well-studied examples are the Cdc42 system of *S. cerevisiae* [37, 44, 75, 91] and the PAR system of *C. elegans* [43, 73, 100, 107]. Despite the complexity of these systems, their phenomenology — cell polarization — is simple and can already be captured by two-component systems as studied here. This raises the question whether complex models can be reduced to an underlying minimal “core” that captures their essential phenomenology. The finding that redistribution of conserved quantities is the core driver of pattern formation in McRD systems suggests that such a reduction might be possible in the phase space of conserved quantities — the *control space*.

Conserved quantities are control parameters for chemical equilibria. Hence, the bifurcation scenario of chemical equilibria in the control space may hence serve as a criterion for classifying models. One example of such a class is the cusp bifurcation scenario, found by numerical analysis of various cell-polarization models in Ref. [43], and identified here as the general bifurcation scenario underlying pattern formation in two-component McRD systems. In an upcoming work, we will use our framework to elucidate the control-space geometry underlying the pole-to-pole oscillations of the *in vivo* MinDE system [33]). As there are two conserved quantities, the total densities of MinD and MinE respectively, the control space is two-dimensional and there are surfaces (instead of lines) of chemical equilibria. Together with the principles of scaffolding by local chemical equilibria, these surfaces allow for a geometric analysis of the *in vivo* MinDE dynamics. We propose this geometrically motivated approach as an alternative to algebraically motivated model reduction methods, such as the quasi-steady-state approximation of slowly diffusing components [153] or (extended) center-manifold reduction [154, 155]. Such an approach offers the advantage that it does not require abstract mathematical calculations and instead enables one to gain physical intuition from elementary geomet-

ric objects and graphical constructions. Furthermore, as pointed out above in Sec. VIII A, chemical equilibria in principle allow one to assess phase-space geometry experimentally. This could ultimately make it possible to infer theoretical models from experimental data at a mesoscopic level, especially in situations where access to more molecular information (at the protein level) is not available yet.

ACKNOWLEDGMENTS

We would like to thank B. Lohner who was involved at early, preliminary stages of this project, M. Wigbers and B. Polovnikov for critical reading of the manuscript and for providing valuable feedback. E.F. acknowledges financial support from the Deutsche Forschungsgemeinschaft (DFG) via project P03 within TRR174 (‘Spatiotemporal Dynamics of Bacterial Cells’). F.B. acknowledges financial support by the DFG Research Training Group GRK2062 (‘Molecular Principles of Synthetic Biology’).

F.B. and J.H. contributed equally to this work.

Appendix A: Models used for illustration and numerical studies

To visualize the our findings on pattern formation in two-component McRD systems we use two prototypical reaction terms, $f(m, c)$, that exhibit two distinct nullcline shapes. Both variants effectively model attachment–detachment dynamics as used to describe cell-polarization systems:

(i) The reaction kinetics used in Ref. [39], to conceptually describe cell-polarization based on autocatalytic recruitment (Michaelis-Menten kinetics with Hill coefficient 2) and linear detachment:

$$f(m, c) = \left(k_{\text{on}} + k_{\text{fb}} \frac{m^2}{K_{\text{d}}^2 + m^2} \right) c - k_{\text{off}} m. \quad (\text{A1})$$

We can non-dimensionalize by expressing time in units of k_{off}^{-1} and densities in units of K_{d} . Furthermore, we set the (non-dimensional) feedback rate $k_{\text{fb}}/k_{\text{off}} =: \hat{k}_{\text{fb}} = 1$ for specificity, leaving only $k := k_{\text{on}}/k_{\text{off}}$ as free parameter in the non-dimensional reaction term:

$$f(m, c) = \left(k + \frac{m^2}{1 + m^2} \right) c - m. \quad (\text{A1}^*)$$

Fig. 18 shows the nullcline in (m, c) -phase space of the reaction term Eq. (A1*) for $k = 0.07$, together with a numerically determined stationary pattern (steady-state solution to Eq. (1)) and the local equilibria (spatial profile on the right).

(ii) Dynamics due to attachment together with linear self-recruitment and enzyme driven detachment (described by first order Michaelis–Menten kinetics):

$$f(m, c) = (k_{\text{on}} + k_{\text{fb}} m)c - k_{\text{off}} \frac{m}{K_{\text{d}} + m}. \quad (\text{A2})$$

We non-dimensionalize by expressing time in units of the attachment rate k_{on} and densities in units of the dissociation constant K_{d} of the detachment kinetics. The two remaining parameters are the (non-dimensional) feedback rate $\hat{k}_{\text{fb}} := k_{\text{fb}}/k_{\text{on}}$ and detachment rate $\hat{k}_{\text{off}} := k_{\text{off}}/k_{\text{fb}}$:

$$f(m, c) = (1 + \hat{k}_{\text{fb}} m)c - \hat{k}_{\text{off}} \frac{m}{1 + m}, \quad (\text{A2}^*)$$

where we dropped the hats. Fig. 19 shows a typical reactive nullcline for the reaction term Eq. (A2*) together with a stationary peak pattern and the local chemical equilibria that scaffold it.

a. *Length scale* — For convenience, we do not specify a unit of length in the domain size L and the diffusion constants $D_{m,c}$. In an intracellular context a typical size would be $L \sim 10 \mu\text{m}$, and typical diffusion constants $D_m \sim 0.01\text{--}0.1 \mu\text{m}^2\text{s}^{-1}$ on the membrane and $D_c \sim 10 \mu\text{m}^2\text{s}^{-1}$ in the cytosol. Rescaling to different spatial dimensions is straightforward.

b. *Nullcline shape predicts the pattern type* — Important for the distinction between peak-forming vs. mesa-forming systems is the behavior of the reactive nullcline for large n . If it approaches the m -axis monotonically for large n , then peak patterns are will form in a large range of \bar{n} for $D_m/D_c \ll 1$ (see Fig. 26). Otherwise, mesa patterns are typical while peak/trough patterns only form in narrow regimes at the edges of the range of pattern existence $[n_{-}^{\infty}, n_{+}^{\infty}]$. For attachment–detachment kinetics, one can study the nullcline behavior for large n by comparing the largest powers in the denominator and numerator of the functional form $c^*(m) = m d(m)/a(m)$ of the nullcline. For the reaction term Eq. (A1*), one obtains $c^*(m \rightarrow \infty) \rightarrow m$, i.e. typically mesa patterns. For the reaction kinetics Eq. (A2*), one has $c^*(m \rightarrow \infty) \rightarrow 0$, favoring peak patterns for $D_c \gg D_m$.

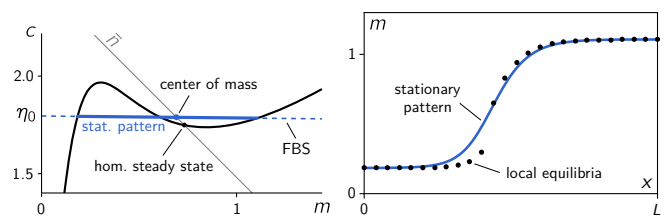


FIG. 18. Left: numerically phase-space distribution (thick blue line) of a computed stationary pattern embedded in the flux balance subspace (dashed blue line). The thin gray line shows the reactive phase space corresponding to the average total density \bar{n} . Right: spatial profile (solid blue line) together with numerically determined local equilibria (●). Parameters: $k = 0.07$, $\bar{n} = 2.48$, $D_m = 0.1$, $D_c = 10$, $L = 10$

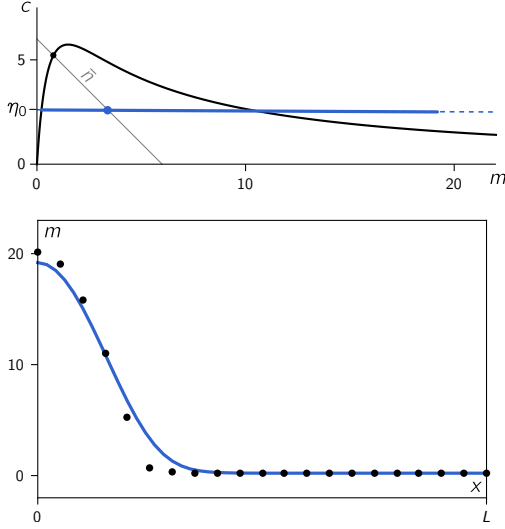


FIG. 19. Above: Numerically determined phase space distribution and stationary pattern profile and for an MCRD system with the reaction kinetics Eq. (A2*). Below: stationary pattern together with local equilibria (●). Parameters: $k_{\text{FB}} = 0.45$, $k_{\text{off}} = 16$, $\bar{n} = 6$, $D_m = 1$, $D_c = 200$, $L = 10$

Appendix B: Numerical simulation

The reaction–diffusion dynamics were simulated on a domain with no-flux boundaries using the numerical PDE-solver routine `NDSolve[]` provided by Mathematica (see Supp. File `PDE-solver_minimal-setup.nb` for an example setup). In the videos we show the density distribution in phase space and the real space profile $m(x, t)$ together with local chemical equilibria.

Appendix C: Linear stability analysis

This section provides the technical details of linear stability analysis.

1. Canonical linear stability analysis

Linear stability analysis of a reaction–diffusion system is performed by expanding a spatial perturbation in the eigenbasis of the diffusion operator (Laplacian) in the geometry of the system. In a line geometry with reflective boundary conditions at $x = 0, L$, the eigenfunctions of the Laplacian are the discrete Fourier modes $\cos(k\pi x/L)$ with $k \in \mathbb{N}$. Linearization of the dynamics of a mass-conserving two-component system around a homogeneous steady state (m^*, c^*) yields the linear dynamics

$$\partial_t \begin{pmatrix} \delta m_q(t) \\ \delta c_q(t) \end{pmatrix} = J(q) \begin{pmatrix} \delta m_q(t) \\ \delta c_q(t) \end{pmatrix} \quad (\text{C1})$$

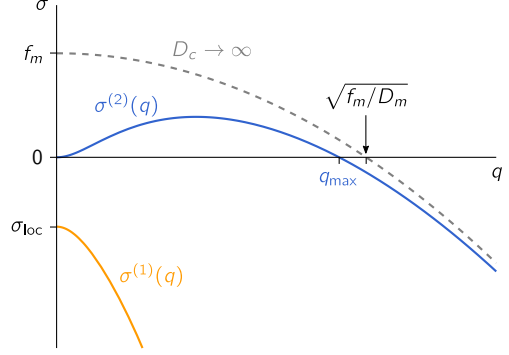


FIG. 20. Generic dispersion relation of the two-component MCRD system in a laterally unstable regime. The two branches $\sigma_q^{(1,2)}$ of the eigenvalue problem for $J(q)$ are shown in blue and yellow. At $q \rightarrow 0$, the branches connect to the eigenvalues $\sigma_{\text{loc}} = f_m - f_c$ and 0 of the local stability problem. For $D_c \rightarrow \infty$, the second branch approaches $\sigma_q^{(2)} \rightarrow f_m - D_m q^2$ for $q > 0$. Accordingly, q_{max} approaches $\sqrt{f_m/D_m}$. “Parameters”: $f_m = 0.7$, $f_c = 1$, $D_m = 1$, $D_c = 10$.

with the Jacobian

$$J(q) = \begin{pmatrix} -D_m q_k^2 + f_m & f_c \\ -f_m & -D_c q_k^2 - f_c \end{pmatrix}, \quad (\text{C2})$$

where we use the abbreviations $q_k = k\pi/L$ for the (discrete) wavenumbers and $f_{m,c} = \partial_{m,c} f|_{(m^*, c^*)}$ for the linearized kinetics at the homogeneous steady state. The eigenvalues of the Jacobian yield the growth rates $\sigma_q^{(i)}$ of the respective eigenmodes such that a perturbation in the spatial eigenfunction $\cos(qx)$ evolves in time as

$$\begin{pmatrix} \delta m_q(t) \\ \delta c_q(t) \end{pmatrix} = \sum_{i=1,2} A_q^{(i)} \mathbf{e}_q^{(i)} \exp(\sigma_q^{(i)} t) \cos(qx), \quad (\text{C3})$$

with the eigenvectors $\mathbf{e}_q^{(i)}$. For a given initial condition (perturbation), the coefficients $A_q^{(i)}$ are determined by projecting initial condition the onto the eigenbasis $\mathbf{e}_q^{(i)} \cos(qx)$.

To calculate the eigenvalues of the Jacobian, we use that the eigenvalues of a 2×2 -matrix can be expressed in terms of its trace τ and determinant δ :

$$\sigma^{(1,2)} = \tau/2 \pm \sqrt{\tau^2/4 - \delta}, \quad (\text{C4})$$

where the indices $\{1, 2\}$ correspond to $\{-, +\}$ on the RHS.

The trace and determinant of the Jacobian $J(q)$ can be written as

$$\begin{aligned} \tau_q &= f_m - f_c - (D_m + D_c)q^2, \\ &= \sigma_{\text{loc}} - (D_m + D_c)q^2, \end{aligned} \quad (\text{C5a})$$

$$\begin{aligned} \delta_q &= q^2 D_m D_c \left(q^2 + \frac{f_c}{D_c} - \frac{f_m}{D_m} \right), \\ &= q^2 D_m D_c (q^2 - q_{\text{max}}^2), \end{aligned} \quad (\text{C5b})$$

where we used the expression Eq. (27) for q_{\max} .

From Eq. (C5a), it follows that for a locally stable hom. steady state ($\sigma_{\text{loc}} < 0$) the trace τ_q is negative for all q . Hence, the only way to get lateral instability is a negative determinant $\delta_q < 0$. This implies that eigenvalues with positive real part must be purely real, since the term under the square root in Eq. (C4) is positive. This means that there cannot be oscillatory lateral instability for a locally stable hom. steady state. Moreover, the instability condition $\delta_q < 0$ immediately yields the band of unstable modes $[0, q_{\max}]$.

Figure 20 shows the two branches of eigenvalues, $\sigma_q^{(1,2)}$, for a laterally unstable case. In the limit $q \rightarrow 0$, the first branch connects to the eigenvalue of a well-mixed system $\sigma_0^{(1)} = \sigma_{\text{loc}}$ (cf. Sec. III A). The corresponding eigenvector lies in the reactive phase space for $q = 0$, and hence fulfills mass conservation.

The second branch, $\sigma_q^{(2)}$, smoothly goes to zero for $q \rightarrow 0$. The eigenvector $\mathbf{e}_0^{(2)}$ corresponding to the marginal eigenvalue $\sigma_0^{(2)} = 0$ points along the reactive nullcline. It represents the shift of the local equilibrium due to a change in total density. For a homogeneous perturbation with $q = 0$ (corresponding to the stability of a well-mixed system), such a perturbation is not allowed since it breaks mass conservation. For $q \neq 0$ mass-redistribution shifts the equilibria. Note that the eigenvector deviates from the marginal direction along the reactive phase space when $q \neq 0$ (see Appendix C 4 and Supplementary Material of Ref. [28]). In particular, the eigenvalue of the marginal mode q_{\max} it points along the flux-balance subspace, $\mathbf{e}_{q_{\max}}^{(2)} \propto (1, -D_m/D_c)^T$, as we found in Sec. IV A in the main text.

We found that the band of unstable modes for the two-component MCRD system always extends down to long wavelength ($q \rightarrow 0$), a situation called “type II” instability in the Cross–Hohenberg classification scheme [62]. In systems with more components and/or multiple conserved species, this is no longer true — the band of unstable modes can be bound away from zero (“type I” in Cross–Hohenberg scheme), see e.g. Ref. [28].

2. Approximation close to the onset of lateral instability

The eigenvalues of a 2×2 -matrix, Eq. C4, to leading order in $\delta/\tau \ll 1$ are given by

$$\sigma^{(1)} = \tau - \delta/\tau + \mathcal{O}(\delta^2/\tau^2), \quad (\text{C6a})$$

$$\sigma^{(2)} = \delta/\tau + \mathcal{O}(\delta^2/\tau^2). \quad (\text{C6b})$$

We will now use this approximation for the two-component MCRD dynamics where the trace and determinant of the Jacobian for a mode q are given by Eqs. (C5). A straight forward calculation shows that δ_q reaches its extremum at $q^* = q_{\max}/\sqrt{2}$, with a minimal

value of $\delta_{q^*} = -\tilde{f}_m^2 D_c / (4D_m)$. Hence, the above approximation is valid in the vicinity of lateral instability onset ($\tilde{f}_m \gtrsim 0$), far away from the onset of local instability (which takes place at $\sigma_{\text{loc}} = 0$). The dispersion relation then reads

$$\sigma_q^{(1)} \approx \sigma_{\text{loc}} - (D_m + D_c)q^2, \quad (\text{C7a})$$

$$\sigma_q^{(2)} \approx \frac{D_m D_c}{-\sigma_{\text{loc}}} q^2 (q_{\max}^2 - q^2), \quad (\text{C7b})$$

for $\tilde{f}_m^2 D_c / D_m \ll |\sigma_{\text{loc}}|$. The first branch, $\sigma_q^{(1)}$, simply represents relaxation to local equilibrium. The laterally unstable branch, $\sigma_q^{(2)}$, shown in Fig. 21(a), is the identical to the dispersion relation of Model B dynamics (Cahn–Hilliard equation, spinodal decomposition [61]). We can rewrite Eq. (C7b) as

$$\sigma_q^{(2)} \approx -D_{\text{eff}} q^2 - \frac{D_m D_c}{-\sigma_{\text{loc}}} q^4 \quad (\text{C7b}^*)$$

which shows that in the long-wavelength limit (diffusion-limited regime) we recover effective (anti-)diffusive dynamics with the effective diffusion constant $D_{\text{eff}} = D_c \partial_n c^*(n) + D_m \partial_n m^*(n)$ that is negative for lateral instability. (To get from Eq. (C7b) to Eq. (C7b^{*}), one needs $\partial_n c^*(n) = \partial_m c^*(m) / (1 + \partial_m c^*(m))$.)

Figure 21 gives an overview of the various regimes of mass-redistribution instability and their interrelation. A typical dispersion relation (solid green line) — together with various limiting cases (see caption for details) — deep in the laterally unstable regime (i.e. far from onset) is shown in (b). This is the case studied in detail in the main text (Sec. IV A, where we discussed diffusion- and reaction-limited regimes and the role of membrane diffusion in particular).

3. Jacobian of mass-redistribution instability

The Jacobian Eq. (C2) for the dynamics in (m, c) -variables can be transformed into the Jacobian for the dynamics in (n, c) -variables most suitably describe mass redistribution instability (MRI). Using the relation $\delta m = \delta n - \delta c$ on the (m, c) -Jacobian Eq. (C2), we obtain the (n, c) -Jacobian

$$J_{(n,c)} = \begin{pmatrix} -D_m q^2 & -(D_c - D_m)q^2 \\ -f_m & -D_c q^2 + f_m - f_c \end{pmatrix}. \quad (\text{C8})$$

Using $\sigma_{\text{loc}} = f_m - f_c$ and $\partial_n c^* \cdot \sigma_{\text{loc}} = f_m$ for the local eigenvalue σ_{loc} and the slope of the nullcline $\partial_n c^*$, we can rewrite the (n, c) -Jacobian as

$$J_{(n,c)} = \begin{pmatrix} -D_m q^2 & -(D_c - D_m)q^2 \\ -\partial_n c^* \cdot \sigma_{\text{loc}} & -D_c q^2 + \sigma_{\text{loc}} \end{pmatrix}. \quad (\text{C9})$$

The linear stability of a mode q in a spatially continuous system, is equivalent to the stability of two compartments coupled by (diffusive) exchange with rates

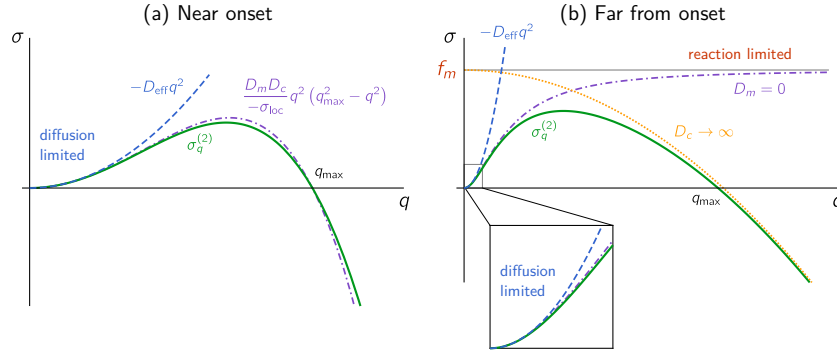


FIG. 21. Overview of the regimes of mass-redistribution instability and their interrelations. (a) Near onset ($D_m/D_c \approx -\chi$ and therefore $q_{\max} \ll \sqrt{f_m/D_m}$), the laterally unstable branch ($\sigma_q^{(2)}$, green solid line) of the dispersion relation is approximated by a fourth-order polynomial (purple, dash-dotted line; cf. Eq. (C7)(b)) that corresponds to the dispersion relation of Model B dynamics. For $q \ll q_{\max}$, the instability is *diffusion limited* (blue dashed line) and effectively described by anti-diffusion with the effective diffusion constant $D_{\text{eff}} = D_c \partial_n c^* + D_m \partial_n m^*$ (see Sec. III D). (b) Dispersion relation far from onset ($D_m/D_c \ll |\chi|$). The case without membrane diffusion (purple dash-dotted line) was elaborated in the main text (Sec. IV A), where we identified diffusion-limited and reaction-limited regimes (cf. Fig. 3(d), diffusive exchange rate $\mathcal{D}_c = D_c q^2$). Finite membrane diffusion suppresses the instability at short wavelength in the reaction-limited regime ($q \gg \sqrt{|\sigma_{\text{loc}}|/D_c}$). There, the dispersion relation is approximated by $f_m - D_m q^2$ (yellow dotted line, note in particular $q_{\max} \approx \sqrt{f_m/D_m}$, the approximation becomes exact in the limit $D_c \rightarrow \infty$). The diffusion-limited regime ($q \ll \sqrt{|\sigma_{\text{loc}}|/D_c}$, blue dashed line) has the same behavior as in the vicinity of onset (a) with the additional simplification that far from onset, the effective diffusion constant $D_{\text{eff}} \approx D_c \partial_n c^*$. “Parameters”: $f_m = 0.5, f_c = 1$ ($\Rightarrow \chi = -0.5, \sigma_{\text{loc}} = -0.5$), $D_m = 1$ and $D_c = 2.1$ for (a) and $D_c = 50$ for (b).

$\mathcal{D}_{m,c} = D_{m,c} q^2$ (as described in the main text, cf. Eq. (32)). The Jacobian of the two-compartment system respectively reads

$$J_{(n,c)} = \begin{pmatrix} -\mathcal{D}_m & -(\mathcal{D}_c - \mathcal{D}_m) \\ -\partial_n c^* \cdot \sigma_{\text{loc}} & -\mathcal{D}_c + \sigma_{\text{loc}} \end{pmatrix}. \quad (\text{C10})$$

For the special case $D_m = 0$, this Jacobian (cf. Eq. (34)) was derived and discussed in Sec. IV. There we argued based on the physical processes underlying a mass-redistribution instability — shifting local equilibria ($\partial_n c^*$), chemical relaxation towards local equilibria (σ_{loc}) and diffusive mass redistribution (D_c) — which are directly represented by the terms in the Jacobian. The role of membrane diffusion is also apparent from the structure of the (n, c) -Jacobian Eq. (C10): It suppresses short wavelengths (large q) via the diagonal-term ($-D_m q^2$) and counteracts mass-redistribution (off-diagonal term $\propto (D_c - D_m)$). See Sec. IV in for a detailed discussion.

a. Linear stability estimate for small membrane diffusion

In the reaction-limited regime of mass-redistribution instability, cytosolic gradients, δc , will be small: $\delta c \ll \delta m$; see eigenvector Eq. C12. Thus, the reactive flow (that builds up the cytosolic gradient driving the mass-redistribution instability) can be estimated by $f_m \delta m$. The diffusive flow on the membrane $D_m \delta m / L^2$ counteracts the mass-redistribution instability and re-balances the system ($D_m \delta m / L^2 \sim f_m \delta m$) at the length scale $\ell = \sqrt{D_m / f_m}$. Recall, that we need $q \gg \sqrt{|\sigma_{\text{loc}}| / D_c}$

to be in the reaction limited regime, so the length scale estimate ℓ is only valid when $\ell^{-1} \gg \sqrt{|\sigma_{\text{loc}}| / D_c}$, i.e. $D_m / D_c \ll -\chi / (1 + \chi)$. This means that the estimates become invalid close to the long wavelength onset of lateral instability where instead the approximation Eq. (C7), presented above, holds.

4. Eigenvectors of MRI

In the main text, we derived the Jacobian for MRI in the case $D_m = 0$ (see Eq. (34)) and studied its eigenvalues, i.e. the growth rate of perturbations, in the reaction- and diffusion limited regimes of MRI (see Fig. 3(d)). The eigenvectors corresponding to these eigenvalues (shown schematically in Fig. 3(e)) are easily obtained in the limiting regimes. To simplify notation, we introduce the notation $\gamma = \partial_n c^*(n)$ for the nullcline slope in (n, c) -phase space.

In the diffusion limited regime ($\mathcal{D}_c \ll |\sigma_{\text{loc}}|$), one finds

$$\mathbf{e}^{(2)} \approx \begin{bmatrix} 1 \\ \gamma \end{bmatrix} + \frac{\mathcal{D}_c}{|\sigma_{\text{loc}}|} \begin{bmatrix} 0 \\ \gamma(1 - \gamma) \end{bmatrix}, \quad (\text{C11})$$

corresponding to the eigenvalue $\sigma^{(2)} \approx -\gamma \mathcal{D}_c$. The eigenvector points along the reactive nullcline as one expects from the physical intuition of slaving to local equilibria.

In the reaction limited regime ($|\sigma_{\text{loc}}| \ll \mathcal{D}_c$), one finds

$$\mathbf{e}^{(2)} \approx \begin{bmatrix} 1 \\ 0 \end{bmatrix} + \frac{|\sigma_{\text{loc}}|}{\mathcal{D}_c} \begin{bmatrix} 0 \\ -\gamma \end{bmatrix}, \quad (\text{C12})$$

corresponding to the eigenvalue $\sigma^{(2)} \approx \gamma\sigma_{\text{loc}}$. The eigenvector points along the n -axis because small cytosolic gradients already lead to fast redistribution compared to the rate of chemical reactions in the reaction limited regime.

5. A mechanical analog for MRI

Mass-redistribution instability can be illustrated with a simple mechanical system exhibiting the key features underlying such an instability (cf. Fig. 5).

Consider a water-filled bucket (cross-sectional area A) resting on an overdamped spring with spring constant k as shown in Fig. 22(a). The equilibrium position $h^*(V)$ of the water level above ground is controlled by the volume V of water the bucket. Adding an amount δV of water, the water level in the bucket increases by $\delta V/A$, while the bucket lowers by an amount $\delta V\rho g/k$ as the spring is compressed due to the added weight force $\delta V\rho g$. Both effects balance exactly when $k = k_{\text{crit}} := \rho g/A$. For a harder spring ($k > k_{\text{crit}}$), the compression is smaller, such that the water level measured from the ground will decrease. Conversely, when the spring is sufficiently soft ($k < k_{\text{crit}}$), it will be compressed more than the water level in the bucket raises, so that the water level measured from the ground will decrease upon an increase of V .

The mechanical equilibrium of such a bucket-on-spring system is a mechanical analog for the (local) chemical equilibrium in a well-mixed compartment (cf. Sec. IV). When two buckets are coupled by a tube that allows water to flow from one bucket to the other, there will be an instability when $\partial_V h^*(V) < 0$ (i.e. $k < k_{\text{crit}}$): any small perturbation $\delta V = V_2 - V_1$ will lead to a difference in water levels δh . The resulting difference in hydrostatic pressure will lead to a flow from the bucket with lower water volume (higher water level h^*) to the bucket with higher water volume (lower water level h^*), and hence further increase the perturbation (see Fig. 22(b)). Conversely, for $\partial_V h^*(V) > 0$ the flow goes from the bucket with more water to the bucket with less water, and thus returns to a homogeneous steady state (see Fig. 22(c)).

Appendix D: Some comments on the adiabatic scaffolding limit

Adiabatic scaffolding, i.e. slaving of the chemical concentrations to the local chemical equilibrium can be derived by separating the timescales of diffusion and local reactions. To that end, let us scale the reaction terms in the reaction-diffusion dynamics Eq. (1) by ε^{-1} :

$$\partial_t m = D_m \nabla_x^2 m + \varepsilon^{-1} f(m, c), \quad (\text{D1a})$$

$$\partial_t c = D_c \nabla_x^2 c - \varepsilon^{-1} f(m, c). \quad (\text{D1b})$$

In the adiabatic scaffolding limit $\varepsilon \rightarrow 0$, local relaxation to chemical equilibrium becomes arbitrarily fast

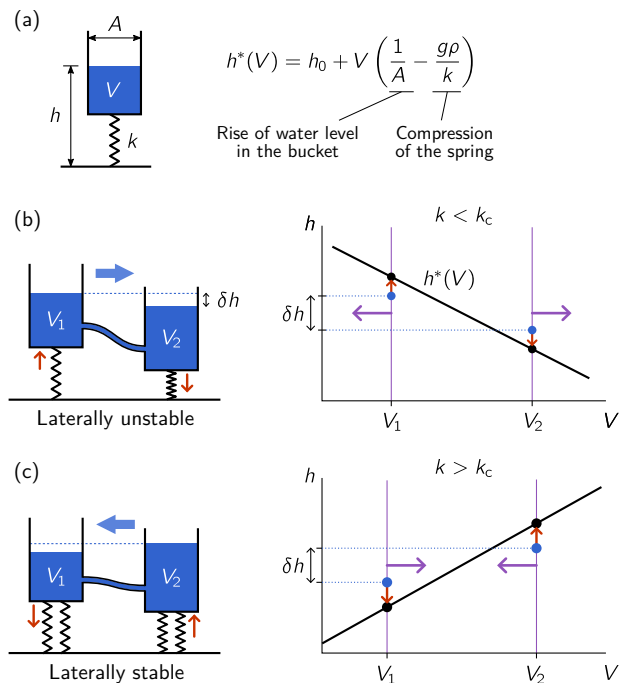


FIG. 22. Illustration of a mass-redistribution instability with a simple mechanical system exhibiting the key features necessary for such an instability. (a) A single water-filled bucket resting on an overdamped spring. The water level in mechanical equilibrium, $h^*(V)$, is controlled by the volume V of water in the bucket. (b) Coupling two buckets on sufficiently soft springs (i.e. $\partial_V h^*(V) < 0$) via a pipe leads to mass-redistribution instability as water flows through the pipe (flow indicated by blue arrow) to remove the gradient in hydrostatic pressure $\sim \delta h$. The instability can be visualized in a (V, h) -diagram (on the right) that is equivalent to the (n, c) -diagram (Fig. 3(c)) in the two-compartment reaction-diffusion system. (c) For hard springs, the equilibrium water level rises with the water volume ($\partial_V h^*(V) > 0$) such that the system of two coupled buckets returns to a homogeneous steady state after a perturbation (lateral stability).

compared to diffusive redistribution — the concentrations will be slaved to a stable chemical equilibrium. The characteristic spatial scale(s) of the dynamics and of stationary patterns are given by a balance of reaction and diffusion. In particular, in Sec. VA, we learned that the interface width is determined by $\pi\sqrt{D_m/\tilde{f}_m}$. Under the scaling of reaction rates by ε^{-1} , this length scale will go to zero as $\propto \varepsilon^{1/2}$. Hence, in the adiabatic scaffolding limit, there is no “microscopic” length scale. This behavior is characteristic for a singular perturbation problem where some physics is lost when the small parameter ε is set to zero [5, 80]. A rigorous analysis of Eqs. (D1) could be performed in terms of singular perturbation theory. To lowest order in ε , any series of jumps (sharp interfaces) between two plateaus n_{\pm} that fulfill $D_c c^*(n_+) + D_m m^*(n_+) = D_c c^*(n_-) + D_m m^*(n_-)$, such that $D_c c^*(\tilde{n}(x)) + D_m m^*(\tilde{n}(x)) = \eta_0$ is constant in space, is a valid steady state of Eq. (23). However, to be consis-

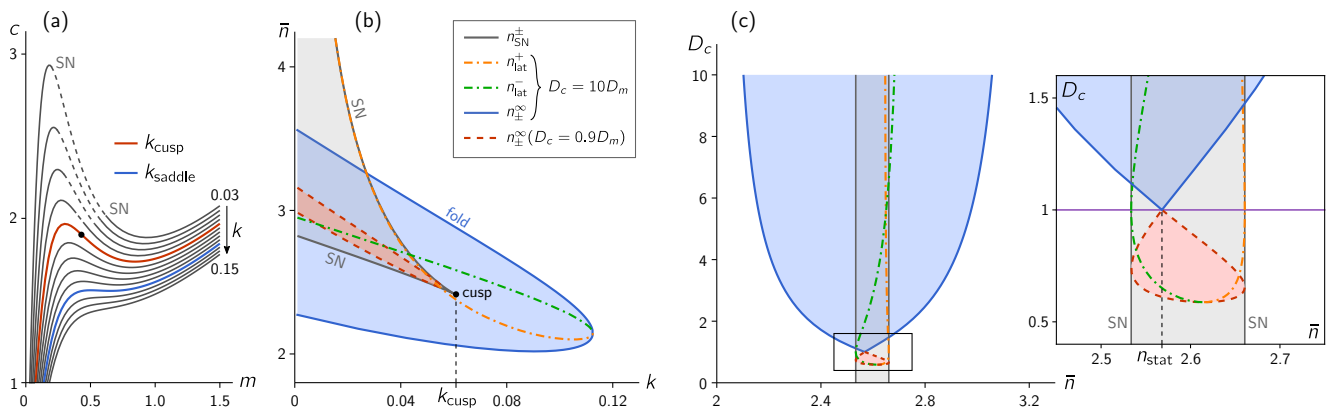


FIG. 23. Bifurcation diagrams obtained by the flux-balance construction (reaction term Eq. (A1*) from Ref. [39]). (a) Deformation of the reactive nullcline under variation of the kinetic rate k from 0.03 to 0.015. Dashed sections indicate local instability in the regime of bistability, that emanates from the cusp bifurcation at k_{cusp} (red nullcline, inflection point marked by black dot). The nullcline exhibiting a saddle point is shown in blue. (b) (k, \bar{n}) -bifurcation diagram (compare Fig. 15(b) in the main text) where the lateral instability bifurcation lines (n_{lat}^{\pm} ; dash-dotted in orange and green) and the regime of pattern existence (shaded in blue, delimited by n_{\pm}^{∞} shown as solid blue line) are shown for $D_c = 10D_m$. Additionally, the region where unstable stationary patterns exist for $D_c = 0.9D_m$ is shaded in red, delimited by a dashed red line. Note the region in the top-right corner, where the local reaction kinetics are bistable, but no stationary patterns exist. (c) (\bar{n}, D_c) -bifurcation diagram for $k = 0.045$, where the reaction kinetics Eq. (A1*) exhibit a region of bistability; the inset shows a blow-up of the boxed region around $\bar{n} \approx n_{\text{stat}}$ and $D_c \approx D_m$. The bifurcation diagrams (b) and (c) were constructed based on following the geometric reasoning presented in Sec. VII with the help of a Mathematica script (see Supp. File `flux-balance-construction.nb`).

tent with Eq. (D1) in the limit $\varepsilon \rightarrow 0$, the FBS-position must be $\eta_0 = \eta_0^{\infty}$ as determined by total-turnover balance Eq. (42). In addition, the given total density \bar{n} constrains the the spatial average $\langle \tilde{n}(x) \rangle_{[0,L]} = L_+ n_+ + L_- n_- = \bar{n}$, where L_{\pm} are the aggregate lengths of the high and low density regions. In future work, going to higher order in the singular perturbation theory might provide further insight into the pattern formation dynamics, in particular the coarsening process.

In Sec. IV, we choose a less technical way to qualitatively illustrate the elementary pattern formation dynamics: we consider the adiabatically scaffolded dynamics not on a continuous domain but in two diffusively coupled compartments. In this ‘coarse grained’ setting, adiabatic scaffolding is well-posed because a ‘microscopic’ length scale as been imposed externally by the discretization into two-compartments.

Appendix E: Geometric construction of bifurcations

In Sec. VC and Sec. VII we describe how the bifurcations diagrams of stationary pattern can be constructed geometrically using the reactive nullcline and the flux-balance subspace. We implemented this procedure in Mathematica (see Supp. File `flux-balance-construction.nb` to find quantitative bifurcation structures. As an illustrative example, we present the results for the reaction kinetics Eq. (A1*); see Figs. 23 and 25. Figure 23(a) shows the shape of the reactive nullcline for a range of the kinetic rate parameter k (non-dimensional

attachment rate). For $k > k_{\text{saddle}}$, the nullcline is monotonic, such that pattern formation is impossible. (Recall that we set the non-dimensional feedback rate to 1, so k effectively describes the relative strength of basal attachment vs. feedback due to recruitment.) At $k = k_{\text{saddle}}$ a section of negative slope emerges on the nullcline, giving rise to lateral instability for $D_c/D_m \rightarrow \infty$. Further lowering k increases the range of negative nullcline slope and increases the maximal negative nullcline slope (thus decreasing D_c^{min} , cf. Eq. (47)). Figure 23(b) shows the regimes of lateral instability and pattern existence for $D_c = 10D_m$. At $k = k_{\text{cusp}}$ the maximal negative nullcline slope becomes -1 , indicating a cusp bifurcation of the chemical equilibria. From this cusp point (black dot on the red nullcline in (a)), a regime of bistability emerges, section of unstable equilibria shown as dashed line in (a)). The locally bistable regime (shaded in gray in (b) is delimited by two saddle-node bifurcations (SN) which emerge from the cusp point, shown as black dot in (b). In the locally bistable regime, there exist *unstable* stationary patterns for $D_c < D_m$. These patterns can be constructed in the same way as stable stationary patterns for $D_c > D_m$. Their range of existence for $D_c = 0.9D_m$ is shaded in red in (b), delimited by a dashed red line.

Figure 23(c) shows the geometrically constructed (\bar{n}, D_c) -bifurcation diagram for $k = 0.045$, i.e. for a bistable nullcline (corresponding to the schematic bifurcation diagram shown in Fig. 13 in the main text). The (\bar{n}, D_c) -bifurcation diagram for a monostable nullcline is shown in Fig. 25 in Appendix F, where we also show the bifurcation structure for finite domain size, L , obtained by numerical continuation.

Appendix F: Numerical continuation of stationary patterns

To calculate steady states and their bifurcation structures for systems with finite size, we use a standard numerical continuation scheme (pseudo-arclength continuation, see e.g. chapter 4 in Ref. [156]). The stationarity condition Eq. (14a) was discretized using finite differences, yielding a set of equations for the concentrations at the grid points. These equations, together with the flux-balance subspace Eq. (10) and the constraint of average total density Eq. (1c), are used to numerically determine the stationary patterns and their bifurcations (in the Mathematica software). To continue the fold bifurcations of stationary patterns, we use a bordered matrix method [156].

To determine the stability of the stationary patterns, we use a finite difference discretization of the reaction-diffusion dynamics (1) linearized around the steady state. The resulting eigenvalue problem is solved with Mathematica. The eigenvalue with the largest real part (“dominant eigenvalue”) determines the pattern stability (see Fig. 28, which is discussed in Appendix I).

a. Bifurcation structure for \bar{n}

Figure 8 in the main text shows the \bar{n} -bifurcation structure of stationary patterns determined by numerical continuation for the reaction kinetics (A1*). In Fig 8, the pattern amplitude is plotted against \bar{n} . For the same bifurcation structure, Fig. 24, shows additional plots of the maximum and minimum concentrations in (a) and the FBS-position, η_0 , in (b). For mesa patterns $\tilde{m}(0)$ and $\tilde{m}(L)$ are the plateau concentrations and therefore slaved to $m_{\pm}^{\infty} = m_{\pm}(\eta_0^{\infty})$, while the FBS-position η_0^{∞} is almost constant. At the boundaries of the range where patterns exist (limited by $[n_{-}^{\infty}, n_{+}^{\infty}]$, for $L \rightarrow \infty$), the mesa patterns undergo fold bifurcations where they meet the branches of unstable peak/trough patterns (dashed lines) that emanate from the homogeneous steady state (black line, dash-dotted in the regime of lateral instability). In both plots, the prediction from the analytic approximation of (unstable) peak/trough patterns (see Appendix G) is shown as red solid lines.

b. Two-parameter (\bar{n}, D_c) -bifurcation diagram

Figure 25 shows the two-parameter (\bar{n}, D_c) -bifurcation diagram for a monostable reactive nullcline (corresponding to the schematic diagram in Fig. 17(a); the fixed parameters are the same as in Fig. 8). The fold-bifurcation lines (solid blue lines) of stationary patterns at finite domain size were obtained by numerical continuation. The respective bifurcation lines in the infinite system size limit, n_{\pm}^{∞} (solid gray lines), were geometrically constructed (cf. Appendix E). The laterally unstable regime,

bounded by the dash-dotted green line, was determined by linear stability analysis. On the right, a blow-up of the region around the critical point $(\bar{n}_{\text{inf}}, D_c^{\text{min}})$. The finite sized system,

The tip of the laterally unstable regime in a finite-sized system is shifted upwards by an amount $\sim L^{-2}$ because of the stability condition $\tilde{f}_m = \pi^2 D_m / L^2$. Close to critical point, the patterns emerge in a supercritical pitchfork bifurcation (dashed green line). The points where the onset becomes sub-critical are marked by in red disks. At these points the two lines of fold bifurcations of stationary patterns originate. The sub-critical lateral instability bifurcation is shown as green dash-dotted line.

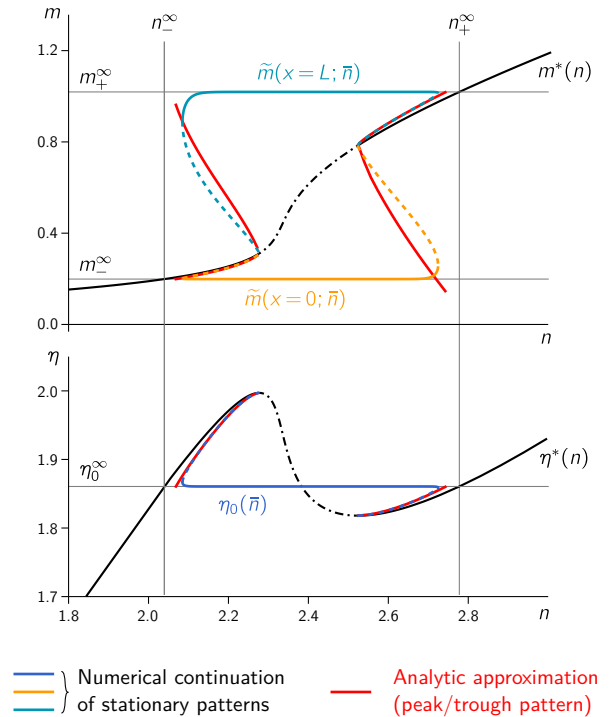


FIG. 24. Numerically determined bifurcation diagram for a two-component MCRD system with the reaction kinetics Eq. (A1*) for the control parameter \bar{n} (average total density). The figure supplements Fig. 8 in the main text, where the bifurcation structure is shown for the pattern amplitude $|\tilde{m}(L) - \tilde{m}(0)|$. The homogeneous steady state is shown as black line, dash-dotted in the regime of lateral instability (note that the slope criterion, Eq. (25), can be written as $\partial_n \eta^* < 0$). For stationary patterns, concentrations at the domain boundaries $\tilde{m}(0)$ and $\tilde{m}(L)$ (yellow and teal lines in the top panel), and the FBS-position η_0 (blue line in the bottom panel) are shown. Thin gray lines indicate the plateau densities m_{\pm}^{∞} and the FBS-position, η_0^{∞} , in the large system size limit $L \rightarrow \infty$. Red lines show the heuristic approximation of peak/trough patterns Eq. (G1), which are the unstable transition states in the multistable regimes (cf. Fig. 8). Note the almost perfect agreement of analytic approximation and numerical solutions for the FBS-position η_0 .

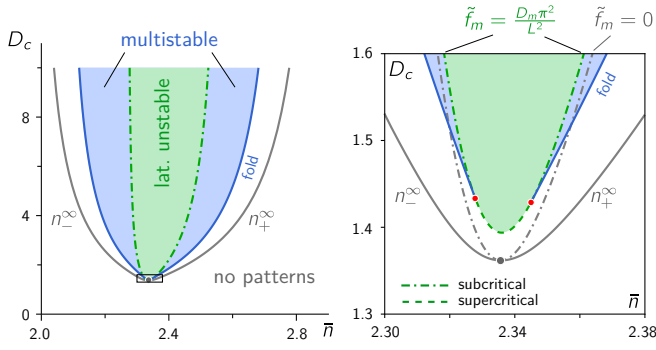


FIG. 25. Right: Numerically determined (\bar{n}, D_c) -bifurcation structure of stationary patterns in a finite sized domain; left: blow-up of the vicinity of the critical point. The continuous blue line marks the fold bifurcation of stationary patterns where stable and unstable stationary patterns meet (cf. Fig. 8(b)). The geometrically constructed bifurcation lines for $L \rightarrow \infty$ are shown in gray. The fold bifurcation where stable and unstable patterns merge terminates in the points where the Turing bifurcation switches from sub- to supercritical ($F_3 = 0$, cf. Eq. (53)). Along the line of supercritical Turing bifurcation (dashed green line), stable patterns emerge directly in a supercritical pitchfork bifurcation. Reaction term: Eq. (A1*); see Fig. 18 for the nullcline shape and a typical pattern profile. Parameters: $k = 0.07$, $D_m = 1$, $L = 100$.

Appendix G: Approximation of peak/trough patterns

In the following, we detail the construction of approximate peak/trough patterns that was briefly introduced in Sec. VB. For specificity, we present the construction for peak patterns – generalization to trough patterns is straight forward.

In our analysis of pattern types (Sec. VB), we characterized peak patterns as composed of an interface region at a system boundary connected to a plateau region (cf. Fig. 7(b)). We have also characterized interfaces by linearization around the inflection point in Sec. VA which yielded a sinusoidal interface shape with a width $L_{\text{int}}(\eta_0)$ (cf. Eq. (38)). We now construct a peak pattern by piecing together such an (approximate) interface at the left domain boundary and a plateau at $m_-(\eta_0)$ in the remainder of the system:

$$\tilde{m}_{\text{peak}}(x) \approx \begin{cases} m_0 + A \sin \pi \left(\frac{x}{L_{\text{int}}} - \frac{1}{2} \right) & x < L_{\text{int}} \\ m_- & x > L_{\text{int}} \end{cases}. \quad (\text{G1})$$

Within this approximation, the pattern inflection point is always at $x_0 = L_{\text{int}}/2$. To match the interface to the plateau continuously at $x = L_{\text{int}}$, the amplitude must be $A = m_- - m_0$. The plateau $m_-(\eta_0)$ and inflection point $m_0(\eta_0)$ are geometrically determined. To close the approximation, one has to find the FBS-position consistent with the given average total density \bar{n} (to fulfill the constraint Eq. (1c)). From Eq. (G1), one obtains the

approximate total density average

$$\bar{n}(\eta_0, L) \approx \eta_0 + (1 - D_m/D_c) \left[m_-(\eta_0) + \frac{L_{\text{int}}(\eta_0)}{L} (m_0(\eta_0) - m_-(\eta_0)) \right]. \quad (\text{G2})$$

This relation can be inverted to obtain a relation $\eta_0(\bar{n}, L)$ for peak patterns with a density-profile approximated by Eq. (G1).

Peak/trough patterns are encountered in two contexts. First, stable peak patterns are typical for reaction kinetics that exhibit a strongly asymmetric nullcline shape, e.g. Eq. (A2*), when $D_m \ll D_c$ (see Fig. 19 for a typical peak pattern). Secondly, *unstable* peak/trough patterns form the unstable branches that connect the subcritical Turing bifurcation with the stable pattern branch (see Fig. 8). These unstable peak/trough patterns play the role of ‘transition’ states since they lie on the separatrix that separates the basins of attraction of the homogeneous steady state and the stationary pattern in the multistable regimes.

For both scenarios, we compared the analytic approximation Eq. (G1), where η_0 is determined via Eq. (G2), with numerical continuation of the stationary patterns.

The approximation of unstable peak/trough patterns for the reaction kinetics Eq. (A1*) is shown in the bifurcation structure Fig. 24.

Figure 26 shows the \bar{n} -bifurcation diagram of stationary patterns for the reaction kinetics Eq. (A2*). There is a large regime of peak patterns where the pattern amplitude keeps increasing with average total density \bar{n} . Peak patterns transition to mesa patterns when peak saturates in the third FBS-NC intersection point m_+ . The amplitude of mesa patterns is almost independent of \bar{n} , because a change of total density merely shifts the interface position of mesa patterns (compare Fig. 8). Ultimately, mesa patterns transition to trough patterns which then undergo a fold bifurcation where they meet with the unstable branch of trough patterns that emerges from the homogeneous steady state. The asymmetry of the reactive nullcline (Fig. 19(a)) is reflected by the asymmetry of the bifurcation structure. The dot-dashed red lines in Fig. 26 show the analytic approximation for pattern amplitude (a), the FBS-position (b) and pattern profiles (c). The approximation of peak patterns becomes less accurate as the average total density increases and ultimately breaks down at the transition to mesa patterns (around $\bar{n} \approx 60$ in Fig. 26). The approximation of trough patterns is less accurate because the trough saturates more “abruptly” in m_- : Recall that the approximation underlying Eq. (G2) is a linearization of the interface region around the inflection point (cf. Sec. VA). This approximation breaks down in regions of high nullcline curvature, indicative of high nonlinearities. Interestingly, even though the pattern profile is not well approximated for troughs (see Fig. 26(c)), the estimate for the FBS-position η_0 is close to the true value (see inset

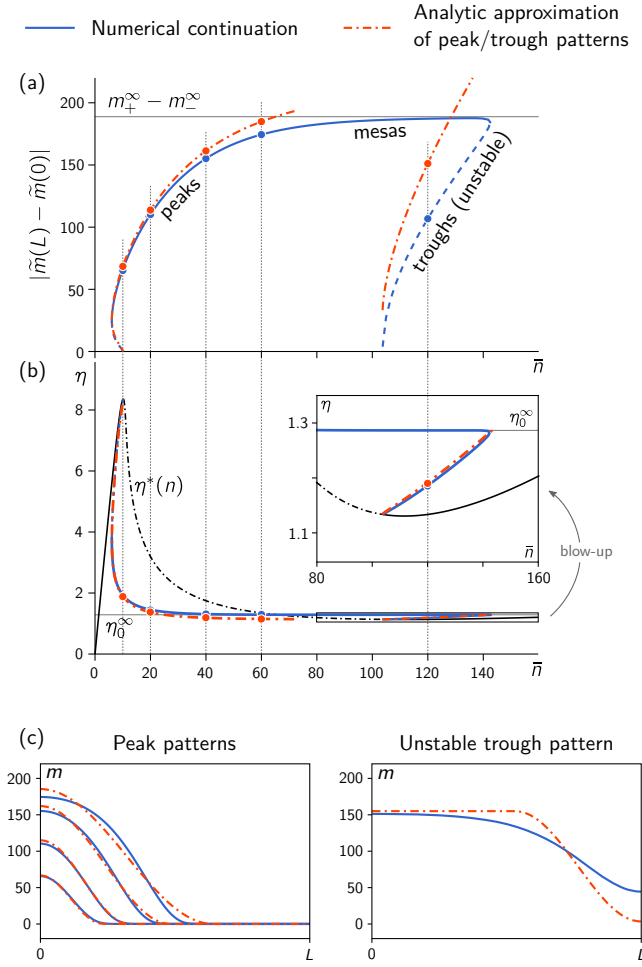


FIG. 26. Numerically determined \bar{n} -bifurcation structure of stationary patterns for the reaction term Eq. (A2*) (see Fig. 19(a) for the nullcline shape). (a) Amplitude $|\tilde{m}(L) - \tilde{m}(0)|$ and FBS-position η_0 (b) of stationary patterns from numerical continuation (blue line, dashed for unstable patterns) and the analytic peak-approximation Eq. (G1) (dash-dotted red line). Peak-type patterns transition to mesa patterns as total average density is increased. The transition threshold can be estimated by the point where the peak approximation (red, dash-dotted line) for the pattern amplitude exceeds the (geometrically determined) plateau amplitude $|m_+^\infty - m_-^\infty|$ (thin gray line). In the (\bar{n}, η_0) -plot (b), the homogeneous steady states (equivalent to the reactive nullcline via $\eta^* = c^* + m^* D_m / D_c$) are shown as solid black line (dash-dotted where laterally unstable). Inset: blowup of the η -axis in the trough pattern region. (c) Stationary pattern profiles from numerical continuation (solid blue lines) and from the analytic approximation (dash-dotted red lines) for various total average densities, corresponding to the dots in (a). Left: $n = 10, 20, 40, 60$, stable peak patterns; right: $\bar{n} = 120$, unstable trough pattern. Fixed parameters: $k_{\text{fb}} = 0.3$, $k_{\text{off}} = 20$, $L = 20$, $D_m = 1$, and $D_c = 200$.

in Fig. 26(c)), indicating that the relevant physics (total turnover balance) is still captured.

Appendix H: Lateral excitability

In Sec. VI, we argued that to trigger pattern formation from a laterally stable homogenous steady state, a perturbation must induce a (self-)sustained laterally unstable region. Based on this intuition we provided a simple geometric heuristic for the excitability threshold: a perturbation of the membrane concentration profile must be such that concentrations in a spatial region are pushed beyond the laterally unstable part of the nullcline in phase space. Hence, the intersection point of the line $c = c^*(\bar{n})$ with the laterally unstable section of the nullcline, provides an estimate $m_{\text{th}}(\bar{n})$ for the threshold that the membrane perturbation has to exceed in a spatial region (see Fig. 27(b), cf. Fig. 10). This criterion does not take into account the spatial shape of a perturbation, but only its characteristics in phase space. We tested how robust the estimate is against different spatial profiles using numerical simulations of the reaction-diffusion dynamics Eqs. (1) with the reaction term Eq. (A1*). We consider prototypical perturbations with a ‘step-like’ profile (see Fig. 27(a)):

$$m_{\text{pert}}(x) = \begin{cases} m^*(\bar{n}) - a & x < L - w \\ m^*(\bar{n}) + b & x > L - w. \end{cases} \quad (\text{H1})$$

For the perturbation to conserve the global average total density, we must set $b = a \frac{L-w}{w}$. The ‘step-like’ profiles therefore form a two-parameter family of perturbations with the shape parameters w (width of the region where density is increased) and a (density removed uniformly from the rest of the system). Because the concentration may not drop below zero, only perturbations with $a < m^*(\bar{n})$ are physically sensible. The (heuristic) threshold in phase space $m_{\text{th}}(\bar{n})$ (see Fig. 27(b)) is exceeded in the (high density) region $x > L - w$ when

$$a > a_{\text{th}}(w; \bar{n}) := \frac{w}{L-w} [m_{\text{th}}(\bar{n}) - m^*(\bar{n})]. \quad (\text{H2})$$

Note that the threshold $m_{\text{th}}(\bar{n})$ in phase space is a function of the average total density. We tested various total average densities \bar{n} across the multistable regime $n_-^\infty < \bar{n} < n_{\text{lat}}^-$, and varied the ‘shape parameters’ of the perturbation — amplitude a and width w — throughout their respective maximal ranges: $0 < a < m^*(\bar{n})$ and $0 < w < L$. Figure 27 shows that there is good agreement between the geometrically estimated threshold and the actual basins of attraction determined by numerical simulation.

Appendix I: Stability of stationary patterns

In our analysis of stationary patterns, we have touched the question of stability of these patterns only periph-

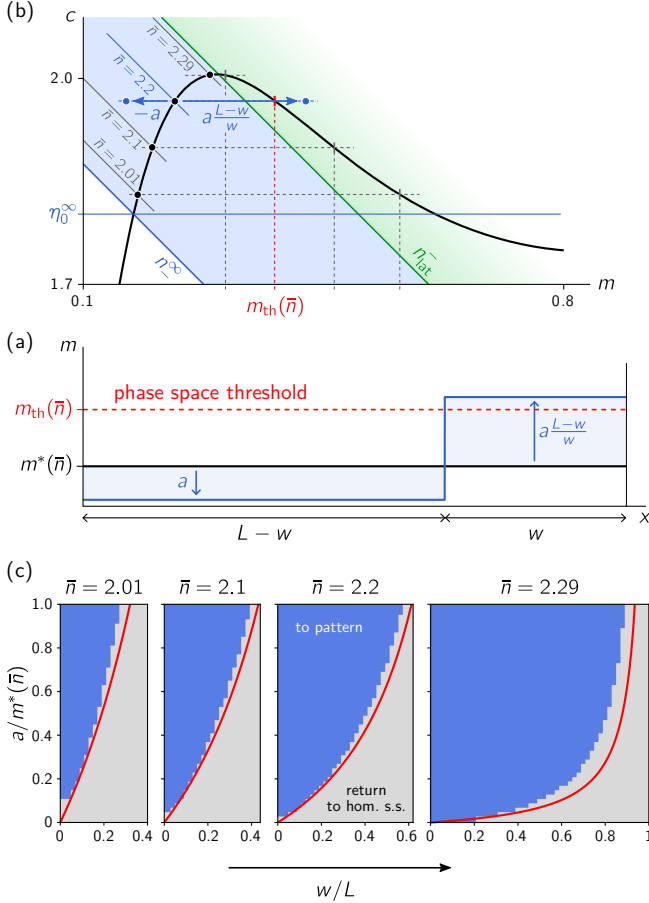


FIG. 27. Test of the geometric heuristic for the excitability threshold by numerical simulations. (a) We consider a prototypical type of perturbation of the homogenous steady state $m^*(\bar{n})$: a ‘step function’ profile moving membrane density from the region $x < L - w$ into the region $x > L - w$; cf. Eq. (H1). Membrane density is lowered by an amount a on the left and increased by an amount $a \frac{L-w}{w}$ so that total mass is conserved. (b) In phase space, the threshold $m_{\text{th}}(\bar{n})$ for a perturbation of membrane density is determined by the intersection point of the line $c = c^*(\bar{n})$ with the laterally unstable section of the nullcline. Colored dashed lines show this construction for various total densities $\bar{n} = 2.01, 2.1, 2.2, 2.29$ in the range of multistability $n_{\infty}^{\infty} < \bar{n} < n_{\text{lat}}^-$ (shaded in blue). The laterally unstable region is shaded in green. (c) The geometrically determined threshold $m_{\text{th}}(\bar{n})$ predicts (red line, $a_{\text{th}}(w; \bar{n})$) which ‘shapes’ of perturbations, parametrized by amplitude a and width w , trigger formation of a stationary pattern. This prediction is in good agreement with the basins of attraction of stationary pattern (shaded in blue) and homogeneous state (shaded in gray) in the parameter space of perturbation ‘shapes’. (Reaction term: Eq. (A1*), parameters: $k = 0.067$, $D_m = 0.1$, $D_c = 10$, $L = 20$.)

erally in Sec. VII B. Coarsening, i.e. the instability of multi-peak / multi-mesa patterns, in two-component McRD systems has been studied before both numerically [36, 44] and semi-analytically [35] for specific choices for the reaction kinetics $f(m, c)$. For specific reaction terms $f(m, c)$ that allow a mapping of the reaction–diffusion dynamics to an effective gradient dynamics, stability of patterns can be analyzed with the help of the effective free energy that is minimized by the stationary pattern [48, 52]. In the broader class of two-component systems without conserved total density, stability of stationary patterns has been subject to numerous mathematical studies, see e.g. Refs. [86, 157, 158].

Instead of the technical tools typically employed there, we choose a more heuristic approach here, building on the physical intuition we have gained throughout this work. We restrict our analysis to the case of mesa patterns with a small interface width compared to the system size ($L_{\text{int}} \ll L$).

Our starting point is the insight that the stationary pattern $(\tilde{m}(x), \tilde{c}(x))$ is embedded in a flux-balance subspace, Eq. (10), whose position η_0^{∞} is determined by total turnover balance, Eq. (17). We hence write the stationary pattern as a pair $(\tilde{m}(x), \eta_0^{\infty})$, where only $\tilde{m}(x)$ depends on x . Next, recall that the pattern itself is scaffolded by local chemical equilibria. In particular, the plateaus are slaved to the plateau scaffolds $m_{\pm}(\eta_0^{\infty})$, and the pattern inflection point is determined by $m_0(\eta_0^{\infty})$. Following a perturbation $\delta m(x, t)$ of the stationary pattern profile, the plateaus will quickly return to their locally stable chemical equilibria, the plateau scaffolds m_{\pm} . On the other hand, a perturbation of the mass-redistribution potential (“FBS-position”) $\delta \eta$, will not only shift the plateau scaffolds, but also cause an imbalance of total reactive turnover. This imbalance drives the dynamics of $\eta(x, t)$ and thus determines the stability of the pattern, as we will see in the following.

The dynamics of $\eta(x, t) = c(x, t) + m(x, t)D_m/D_c$ follows straightforwardly from the reaction–diffusion dynamics Eq. (1) and read:

$$\begin{aligned} \partial_t \eta(x, t) &= D_c \nabla_x^2 \eta + (D_m/D_c - 1) \partial_t m \\ &= D_c \nabla_x^2 \eta + D_m (D_m/D_c - 1) \nabla_x^2 m \\ &\quad + (D_m/D_c - 1) \tilde{f}(m, \eta) \end{aligned} \quad (11)$$

In linearization around a steady-state pattern $(\tilde{m}(x), \eta_0^{\infty})$, we have

$$\begin{aligned} \partial_t \delta \eta(x, t) &= D_c \nabla_x^2 \delta \eta + D_m (D_m/D_c - 1) \nabla_x^2 \delta m \\ &\quad + (D_m/D_c - 1) [\tilde{f}_m \delta m + \tilde{f}_\eta \delta \eta]_{(\tilde{m}(x), \eta_0^{\infty})}, \end{aligned} \quad (12)$$

where the membrane perturbation $\delta m = \delta m(x, t)$ is governed by the linearization of the reaction–diffusion dynamics Eq. (1a). The intuition is that $\delta m(x, t)$ quickly relaxes to the scaffold of local equilibria. We therefore focus on the dynamics of $\delta \eta(x, t)$, which will affect the scaffold itself by shifting local equilibria, in particular the plateau scaffolds $m_{\pm}(\eta)$.

Reactive turnover balance is primarily determined in the interfacial region (cf. Fig. 2) around the pattern inflection point x_0 . We therefore focus on the interface region to learn how an imbalance of total reactive turnover affects the perturbation of the mass-redistribution potential (“FBS-shift”) $\delta\eta(x, t)$. To that end, we use that the gradient of the membrane profile, $\nabla_x \tilde{m}(x)$, is negligible in the plateaus and whereas it peaks at the inflection point x_0 . We hence multiply Eq. (I2) by $\nabla_x \tilde{m}(x)$ and integrate over the whole domain $[0, L]$ to obtain

$$\begin{aligned} \partial_t \delta\eta(x_0, t) &\approx \delta\eta(x_0, t) \frac{D_m/D_c - 1}{m_+ - m_-} \int_{m_-}^{m_+} dm \tilde{f}_\eta(m, \eta_0^\infty) \\ &+ D_c \nabla_x^2 \delta\eta(x_0, t) + \mathcal{O}(\delta m(x, t)). \end{aligned} \quad (\text{I3})$$

We neglect contributions $\mathcal{O}(\delta m(x, t))$ that correspond to perturbation along the direction of the FBS and quickly relax to the scaffold on the timescale $|\sigma_{\text{loc}}|^{-1}$, fast compared to the contribution by the first term in Eq. (I3). Furthermore, because mass-redistribution $\eta(x, t)$ quickly homogenizes in the (small) interface region, we can neglect the second term $\nabla_x^2 \delta\eta(x_0, t)$.

Fig. 28 shows a comparison of the heuristic estimates of perturbation growth/decay rate based on Eq. (50) to numerically determined dominant eigenvalues $\sigma_{\text{max}}(D_c)$ (linear stability analysis of stationary patterns determined by numerical continuation). The dominant eigenvalue $\sigma_{\text{max}}(D_c)$ crosses over from system size independent growth rate of perturbations for $D_c < D_m$ to system size dependent decay of perturbations for $D_c > D_m$. The instability is well estimated by turnover imbalance term in Eq. (50) (dashed red line in the inset in (b)), while the rate at which perturbations decay in the stable regime ($D_c > D_m$) is limited by diffusive transport $\sigma_{\text{diff}} \sim D_c/L^2$ between the far ends of the system. Reactive timescales will become limiting in the stable regime only when $\sigma_{\text{diff}} \approx \sigma_{\text{loc}}$, i.e. for fast enough cytosolic diffusion or a small system.

Appendix J: Weakly nonlinear analysis

Our goal is to find the stationary pattern in the vicinity of the onset of lateral instability (Turing bifurcation). To that end, we expand the stationary state $(\tilde{m}(x), \eta_0)$ in harmonic functions (eigenmodes of the Laplace operator under no-flux boundary conditions):

$$\begin{aligned} \tilde{m}(x) &\approx m^* + \delta m_0 + \delta m_1 \cos(\pi x/L) \\ &+ \delta m_2 \cos(2\pi x/L), \end{aligned} \quad (\text{J1a})$$

$$\eta_0 \approx \eta^* + \delta\eta_0, \quad (\text{J1b})$$

where $\eta^* = D_m/D_c m^* + c^*$ is the FBS position of the homogenous steady state. Mass conservation necessitates $\delta m_0 + \delta\eta_0 - D_m/D_c \delta m_0 = 0$, hence

$$\delta\eta_0 = (D_m/D_c - 1) \delta m_0$$

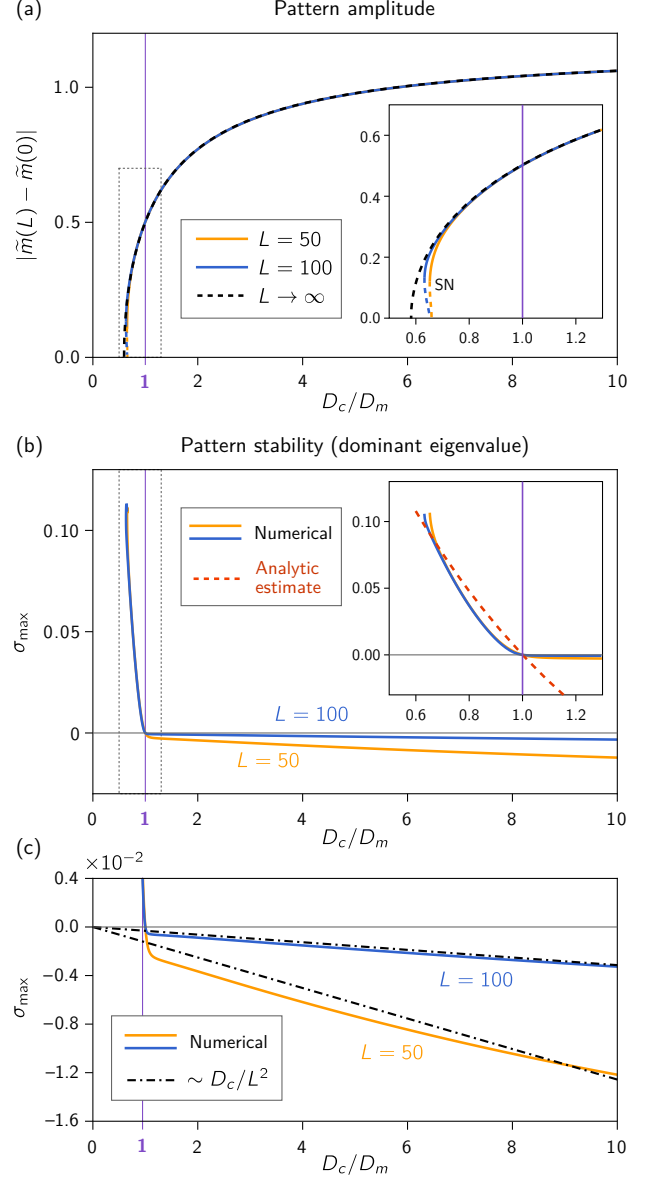


FIG. 28. Stability of stationary patterns as a function of D_c . (a) Pattern amplitude for a D_c -sweeps at constant $\bar{n} = n_{\text{stat}}$ for two system sizes $L = 50$ (yellow) and $L = 100$ (blue), obtained by numerical continuation, and geometric construction (corresponding to $L \rightarrow \infty$, dashed black line). The fixed parameters are the same as in Fig. 8. Finite size affects the stationary pattern amplitude only in the vicinity of the saddle-node bifurcation at $\approx D_c^{\text{min}}$ (see inset: zoom on gray box). The purple line marks $D_c = D_m$. (b) Numerically determined dominant eigenvalues (maximal real part shown as solid lines) indicating linear stability of the patterns. Patterns are stable for $D_c > D_m$ and unstable for $D_c < D_m$, as predicted by the geometric arguments. The dominant eigenvalue for the unstable patterns is almost independent of system size. The approximation based on this geometric intuition of turnover imbalance (first term in Eq. (50)) is shown as red, dashed line in the inset. (c) Blow-up of the σ -axis, for negative values. For stable patterns ($D_c > D_m$), decay of perturbations is mainly determined by the timescale $\sim D_c/L^2$ of mass-transfer from one end of the system to the other. (The dot-dashed lines show the relation $-\alpha D_c/L^2$, where the prefactor $\alpha \approx 3.1$ that depends on the system specifics has been fitted by eye.)

We plug the ansatz Eq. (J1a) into the stationarity condition, Eq. (14a), Taylor expand \tilde{f} , and project onto the zeroth harmonic (this is most conveniently done in CAS software, e.g. Wolfram Mathematica)

$$0 = (\tilde{f}_m + (1 - D_m/D_c)\tilde{f}_\eta)\delta m_0 + \frac{1}{4}\tilde{f}_{mm}\delta m_1^2 + \mathcal{O}(\delta m_0^2, \delta m_1^2\delta m_2, \delta m_0\delta m_1^2, \delta m_0\delta m_2^2), \quad (\text{J2})$$

and onto the second harmonic

$$0 = (\tilde{f}_m - 4D_m\pi^2/L^2)\delta m_2 + \frac{1}{4}\tilde{f}_{mm}\delta m_1^2 + \mathcal{O}(\delta m_2^2, \delta m_0\delta m_1^2, \delta m_0^2\delta m_2, \delta m_1^2\delta m_2). \quad (\text{J3})$$

Solving for δm_0 and δm_2 we get

$$\delta m_0 = \frac{1}{4}\frac{\tilde{f}_{mm}}{\tilde{f}_m + (1 - D_m/D_c)\tilde{f}_\eta}\delta m_1^2 + \mathcal{O}(\delta m_1^4), \quad (\text{J4a})$$

$$\delta m_2 = \frac{1}{4}\frac{\tilde{f}_{mm}}{\tilde{f}_m - 4D_m\pi^2/L^2}\delta m_1^2 + \mathcal{O}(\delta m_1^4). \quad (\text{J4b})$$

These equations describe how asymmetry of the nullcline shape (and thereby reactive turnover) influences the pattern profile. For $\tilde{f}_{mm} = 0$ the turnovers on either side of the inflection point grow symmetrically (with opposite sign) as the amplitude δm_1 of the pattern increases. This symmetry of the turnovers only occurs at the inflection point of the nullcline where its shape is point-symmetric. Away from the inflection point of the nullcline, its shape is no longer symmetric around the steady state (m^*, c^*), and, respectively, the turnovers grow asymmetrically in the two halves of the system. This asymmetry creates an imbalance of the total turnover that is compensated by two effects: (i) the flux-balance subspace shifts (i.e. η_0 will deviate from η^*), and (ii) the pattern itself becomes asymmetric as the second harmonic will have a non-zero amplitude δm_2 . Together, these two effects compensate the asymmetry of the turnovers, such that flux-turnover balance is reached.

The amplitude δm_1 of the stationary pattern is obtained by projecting (14a) onto the first harmonic $\cos(\pi x/L)$

$$0 = F_1 \delta m_1 + F_3 \delta m_1^3 + \mathcal{O}(\delta m_1^5), \quad (\text{J5})$$

where

$$F_1 = \tilde{f}_m - D_m\pi^2/L^2, \quad (\text{J6})$$

and

$$F_3 = \frac{\tilde{f}_{mmm}}{8} - \frac{\tilde{f}_{mm}}{8}\frac{\tilde{f}_{mm}}{\tilde{f}_m - 4D_m\pi^2/L^2} - \frac{\tilde{f}_{mm}\tilde{f}_{mm} - (1 - D_m/D_c)\tilde{f}_{m\eta}}{4}\frac{\tilde{f}_{mm}}{\tilde{f}_m - (1 - D_m/D_c)\tilde{f}_\eta}. \quad (\text{J7})$$

Since there is no second order term in Eq. (J5), patterns always originate in a pitchfork bifurcation. At the bifurcation point, the first order coefficient vanishes ($F_1 = 0$).

The system is laterally unstable if F_1 is positive (cf. Eq. (27)). Hence, only if $F_3 < 0$, the third order coefficient can saturate the pattern amplitude (supercritical bifurcation). For $F_3 > 0$ the bifurcation is subcritical.

The third order coefficient can be simplified further: A simple calculation shows that

$$\tilde{f}_m - (1 - D_m/D_c)\tilde{f}_\eta = f_m - f_c = \sigma_{\text{loc}}, \quad (\text{J8})$$

and therefore

$$\begin{aligned} \tilde{f}_{mm} - (1 - D_m/D_c)\tilde{f}_{m\eta} &= \partial_m \sigma_{\text{loc}}(m, \eta - m D_m/D_c) \\ &= \tilde{\partial}_m \sigma_{\text{loc}}(m, \eta) \end{aligned} \quad (\text{J9})$$

where $\tilde{\partial}_m = \partial_m - (D_m/D_c)\partial_c$ is the derivative along the flux-balance subspace. With that, the second summand in the brackets in F_3 (cf. Eq. (J7)) can be rewritten and we obtain

$$F_3 = \frac{\tilde{f}_{mmm}}{8} - \frac{\tilde{f}_{mm}}{2} \left(\frac{\tilde{f}_{mm}/2}{\tilde{f}_m - 4D_m\pi^2/L^2} + \frac{\tilde{\partial}_m \sigma_{\text{loc}}}{\sigma_{\text{loc}}} \right). \quad (\text{J10})$$

We further rewrite the denominator of the first summand in the brackets as $F_1 - 3D_m\pi^2/L^2$, and use that F_1 vanishes at the bifurcation point (i.e. is small in its vicinity). We thus have

$$F_3 = \frac{\tilde{f}_{mmm}}{8} + \frac{\tilde{f}_{mm}^2}{24}\frac{L^2}{\pi^2 D_m} - \frac{\tilde{f}_{mm}}{4}\frac{\tilde{\partial}_m \sigma_{\text{loc}}}{\sigma_{\text{loc}}} + \mathcal{O}(F_1). \quad (\text{J11})$$

Note that in weakly nonlinear approximation Eq. (53) in the main text, we have pulled the $\mathcal{O}(F_1)$ out from F_3 to simplify notation. The role and physical interpretation of the three terms in F_3 , as written in the form Eq. (J11), are discussed in the main text in Sec. VIII D.

Appendix K: Nullcline curvature approximation

As we will show in the following, in the vicinity of the onset of lateral instability (recall the slope criterion $-D_m/D_c > \chi = -f_m/f_c$, cf. Eq. (25)), the nullcline curvature κ can be approximated by

$$\kappa \approx -\frac{f_c^2}{(f_m^2 + f_c^2)^{3/2}}\tilde{f}_{mm}. \quad (\text{K1})$$

To see how this relation comes about, we start by rewriting \tilde{f}_{mm} in terms of derivatives of f :

$$\begin{aligned} \tilde{f}_{mm} &= \partial_m^2 f \left(m, \eta - \frac{D_m}{D_c} m \right) \\ &= f_{mm} - 2\frac{D_m}{D_c} f_{mc} + \left(\frac{D_m}{D_c} \right)^2 f_{cc} \end{aligned} \quad (\text{K2})$$

In the vicinity of the Turing bifurcation, we have $-D_m/D_c \approx -f_m/f_c$ (from the slope criterion for lateral instability), so we obtain

$$\tilde{f}_{mm} \approx f_c^{-2} (f_c^2 f_{mm} - 2f_m f_c f_{mc} + f_m^2 f_{cc}). \quad (\text{K3})$$

When one compares this to the formula for the curvature κ of an implicitly determined curve $f(m, c) = 0$

$$\kappa = -\frac{f_c^2 f_{mm} - 2f_m f_c f_{mc} + f_m^2 f_{cc}}{(f_m^2 + f_c^2)^{3/2}}, \quad (\text{K4})$$

one sees that the numerator of the curvature formula matches the term in the brackets in Eq. (K3). Thus, by combining Eqs. (K3) and (K4), we obtain the approximation Eq. (K1).

-
- [1] S. H. Strogatz, *Nonlinear Dynamics and Chaos*, 2nd ed. (Westview Press, 2014).
- [2] E. M. Izhikevich, *Dynamical systems in neuroscience: the geometry of excitability and bursting* (The MIT Press, Cambridge, Massachusetts, 2007).
- [3] A. S. Mikhailov, *Foundations of Synergetics I: Distributed Active Systems*, 2nd ed., Springer Series in Synergetics 51 (Springer-Verlag Berlin Heidelberg, 1994).
- [4] J. D. Murray, *Mathematical Biology I. An Introduction*, 3rd ed., Interdisciplinary Applied Mathematics, Vol. 17 (Springer, New York, 2002).
- [5] E. A. Jackson, *Perspectives of Nonlinear Dynamics*, Vol. 1 (Cambridge University Press, 1989).
- [6] M. Cross and H. Greenside, *Pattern Formation and Dynamics in Nonequilibrium Systems* (Cambridge University Press, 2009).
- [7] E. Ott, *Chaos in Dynamical Systems*, 2nd ed. (Cambridge University Press, 2002).
- [8] H. Poincaré, *Les méthodes nouvelles de la mécanique céleste*, Vol. 1–3 (Gauthiers-Villars, Paris, 1892, 1893, 1899) english translation edited by D. Goroff, published by the American Institute of Physics, New York, 1993.
- [9] S. Wiggins, *An Introduction to Applied Nonlinear Dynamical Systems and Chaos*, 2nd ed., edited by J. Marsden, S. Antman, and L. Sirovich (Springer, New York, 2003).
- [10] J. Guckenheimer and P. Holmes, *Nonlinear Oscillations, Dynamical Systems, and Bifurcations of Vector Fields*, Applied Mathematical Sciences No. 42 (Springer, New York, 1983).
- [11] R. Thom, *Structural Stability And Morphogenesis* (Addison-Wesley, 1975) translated from the French edition by D. H. Fowler.
- [12] T. Poston and I. Stewart, *Catastrophe Theory and Its Applications* (Dover, 2012).
- [13] E. Schöll and H. G. Schuster, eds., *Handbook of Chaos Control*, 2nd ed. (Wiley-VCH, 2008).
- [14] A. L. Hodgkin and A. F. Huxley, *The Journal of Physiology* **117**, 500 (1952).
- [15] E. M. Izhikevich, *International Journal of Bifurcation and Chaos* **10**, 1171 (2000).
- [16] H. Haken, *Physics Letters A* **53**, 77 (1975).
- [17] M. Sciamanna and K. A. Shore, *Nature Photonics* **9**, 151 (2015).
- [18] B. Novák and J. J. Tyson, *Nature Reviews Molecular Cell Biology* **9**, 981 (2008).
- [19] J. J. Tyson, C. I. Hong, C. Dennis Thron, and B. Novak, *Biophysical Journal* **77**, 2411 (1999).
- [20] J. E. Ferrell, T. Y.-C. Tsai, and Q. Yang, *Cell* **144**, 874 (2011).
- [21] A. Roberts and R. Saha, *Climate Dynamics* **48**, 2123 (2016).
- [22] A. C. Fowler, T. Murray, and F. S. L. Ng, *Journal of Glaciology* **47**, 527 (2001).
- [23] C. K. R. T. Jones, *Geometric singular perturbation theory*, edited by R. Johnson, Dynamical Systems. Lecture Notes in Mathematics, Vol. 1609 (Springer, New York, 1994) pp. 44–118.
- [24] G. Hek, *Journal of Mathematical Biology* **60**, 347 (2009).
- [25] R. Fisher, *Annals of Eugenics* **7**, 355 (1937).
- [26] A. Kolmogorov, I. Petrovsky, and N. Piscounov, *Moscou Univ. Bull. Math.* **1**, 1 (1937).
- [27] D. Jones, M. Plank, and B. Sleeman, *Differential Equations and Mathematical Biology*, 2nd ed., Chapman & Hall/CRC Mathematical and Computational Biology Series (Taylor & Francis, 2009).
- [28] J. Halatek and E. Frey, *Nature Physics* **14**, 507 (2018).
- [29] L. Onsager, *Physical Review* **37**, 405 (1931).
- [30] These chemical equilibria should not be confused with the concept of local thermal equilibria as in Onsager's theory of close to equilibrium dynamics [29].
- [31] J. Denk, S. Kretschmer, J. Halatek, C. Hartl, P. Schwille, and E. Frey, *Proc. Natl. Acad. Sci. U.S.A.*, 201719801 (2018).
- [32] F. Brauns, J. Halatek, and E. Frey, (unpublished).
- [33] F. Brauns, J. Halatek, and E. Frey, (unpublished).
- [34] T. Hermann, M. Wigbers, F. Brauns, and E. Frey, (unpublished).
- [35] S. Ishihara, M. Otsuji, and A. Mochizuki, *Phys. Rev. E* **75**, 015203 (2007).
- [36] M. Otsuji, S. Ishihara, C. Co, K. Kaibuchi, A. Mochizuki, and S. Kuroda, *PLoS Computational Biology* **3**, e108 (2007).
- [37] A. B. Goryachev and A. V. Pokhilko, *FEBS Letters* **582**, 1437 (2008).
- [38] S. J. Altschuler, S. B. Angenent, Y. Wang, and L. F. Wu, *Nature* **454**, 886 (2008).
- [39] Y. Mori, A. Jilkine, and L. Edelstein-Keshet, *Biophysical Journal* **94**, 3684 (2008).
- [40] A. Jilkine and L. Edelstein-Keshet, *PLoS Computational Biology* **7**, e1001121 (2011).
- [41] A. Jilkine, S. B. Angenent, L. F. Wu, and S. J. Altschuler, *PLoS Computational Biology* **7**, e1002271 (2011).
- [42] L. Edelstein-Keshet, W. R. Holmes, M. Zajac, and M. Dutot, *Philosophical Transactions of the Royal So-*

- ciety B: Biological Sciences **368**, 20130003 (2013).
- [43] P. K. Trong, E. M. Nicola, N. W. Goehring, K. V. Kumar, and S. W. Grill, *New Journal of Physics* **16**, 065009 (2014).
- [44] J.-G. Chiou, S. A. Ramirez, T. C. Elston, T. P. Witelski, D. G. Schaeffer, and D. J. Lew, *PLoS Computational Biology* **14**, e1006095 (2018).
- [45] E. F. Keller and L. A. Segel, *Journal of Theoretical Biology* **26**, 399 (1970).
- [46] K. Pham, A. Chauviere, H. Hatzikirou, X. Li, H. M. Byrne, V. Cristini, and J. Lowengrub, *Journal of Biological Dynamics* **6**, 54 (2012).
- [47] A. Pogan and A. Scheel, *J. Dyn. Differ. Equ.* **24**, 249 (2012).
- [48] R. N. Goh, S. Mesuro, and A. Scheel, *SIAM Journal on Applied Dynamical Systems* **10**, 360 (2011).
- [49] F. van Wijland, K. Oerding, and H. Hilhorst, *Physica A: Statistical Mechanics and its Applications* **251**, 179 (1998).
- [50] D. A. Kessler and H. Levine, *Nature* **394**, 556 (1998).
- [51] G. Caginalp, *Archive for Rational Mechanics and Analysis* **92**, 205 (1986).
- [52] Y. Morita and T. Ogawa, *Nonlinearity* **23**, 1387 (2010).
- [53] I. Prigogine and R. Lefever, *The Journal of Chemical Physics* **48**, 1695 (1968).
- [54] T. Kolokolnikov, T. Erneux, and J. Wei, *Physica D: Nonlinear Phenomena* **214**, 63 (2006).
- [55] T. Kolokolnikov, M. Ward, and J. Wei, *Physica D: Nonlinear Phenomena* **236**, 104 (2007).
- [56] Y. Mori, A. Jilkine, and L. Edelstein-Keshet, *SIAM Journal on Applied Mathematics* **71**, 1401 (2011).
- [57] J. Halatek, F. Brauns, and E. Frey, *Philosophical Transactions of the Royal Society B: Biological Sciences* **373**, 20170107 (2018).
- [58] A. M. Turing, *Philosophical Transactions of the Royal Society B: Biological Sciences* **237**, 37 (1952).
- [59] We will use the terms lateral instability and Turing instability interchangeably. This means we take the term slightly more general than it is typically done in the literature, where Turing instability became exclusively associated with instabilities that have a characteristic wavelength at onset, called ‘type I’ in the Cross-Hohenberg classification scheme [62].
- [60] The nullcline slopes in (m, c) -phase space, $\partial_m c^*(m)$, and in (n, c) -phase space $\partial_n c^*(n)$, are related via $\partial_n c^*(n) = \partial_m c^*(m)/(1 + \partial_m c^*(m))$. Recall that for a locally stable fixed point $\partial_m c^*(m) > 1$ (see Eq. (7) in Sec. III A).
- [61] J. W. Cahn, *Acta Metallurgica* **9**, 795 (1961).
- [62] M. C. Cross and P. C. Hohenberg, *Reviews of Modern Physics* **65**, 851 (1993).
- [63] I. Lifshitz and V. Slyozov, *Journal of Physics and Chemistry of Solids* **19**, 35 (1961).
- [64] C. Wagner, *Zeitschrift für Elektrochemie* **65**, 581 (1961).
- [65] M. E. Cates and E. Tjhung, *Journal of Fluid Mechanics* **836**, P1 (2017).
- [66] E. Tjhung, C. Nardini, and M. E. Cates, *Physical Review X* **8**, 031080 (2018).
- [67] C. A. Weber, D. Zwicker, F. Jülicher, and C. Fan Lee, *preprint*, arXiv:1806.09552 (2018).
- [68] D. Zwicker, A. A. Hyman, and F. Jülicher, *Physical Review E* **92**, 012317 (2015).
- [69] K. Kang, T. Kolokolnikov, and M. J. Ward, *IMA Journal of Applied Mathematics* **72**, 140 (2007).
- [70] E. Latos, Y. Morita, and T. Suzuki, *Journal of Dynamics and Differential Equations* **30**, 823 (2018).
- [71] S. Jimbo and Y. Morita, *Journal of Differential Equations* **255**, 1657 (2013).
- [72] L. Wolpert, *Journal of Theoretical Biology* **25**, 1 (1969).
- [73] N. W. Goehring, P. K. Trong, J. S. Bois, D. Chowdhury, E. M. Nicola, A. A. Hyman, and S. W. Grill, *Science* **334**, 1137 (2011).
- [74] C. Hoegge and A. A. Hyman, *Nature Reviews Molecular Cell Biology* **14**, 315 (2013).
- [75] B. Klünder, T. Freisinger, R. Wedlich-Söldner, and E. Frey, *PLoS Computational Biology* **9**, e1003396 (2013).
- [76] T. Freisinger, B. Klünder, J. Johnson, N. Müller, G. Pichler, G. Beck, M. Costanzo, C. Boone, R. A. Cerione, E. Frey, and et al., *Nature Communications* **4**, 1807 PE (2013).
- [77] M. Ivanov, V. Popkov, and J. Krug, *Phys. Rev. E* **82**, 011606 (2010).
- [78] E. J. Crampin, E. A. Gaffney, and P. K. Maini, *Journal of Mathematical Biology* **44**, 107 (2002).
- [79] S. M. Murray and V. Sourjik, *Nature Physics* **13**, 1006 (2017).
- [80] M. J. Ward, *Bulletin of Mathematical Biology* **68**, 1151 (2006).
- [81] P. W. Bates and P. C. Fife, *SIAM Journal on Applied Mathematics* **53**, 990 (1993).
- [82] F. Bergmann, L. Rapp, and W. Zimmermann, *Physical Review E* **98** (2018), 10.1103/physreve.98.020603.
- [83] S. M. Allen and J. W. Cahn, *Acta Metallurgica* **20**, 423 (1972).
- [84] For a simple contact process with noise, the case $D_c < D_m$ (i.e. the self-recruiting component is the faster diffusing one), shows interesting correlations, while a first order phase transition has been conjectured for $D_m < D_c$ [49]. Note, however, that the simple contact process under consideration in Ref. [49] does not exhibit bistability.
- [85] The slope χ of a continuous reactive nullcline smoothly approaches the slope -1 at the saddle-node bifurcations of the chemical equilibria. Hence, as D_c is decreased, the laterally unstable regions shrink, but disappear fully only at $D_c = D_m$. In the vicinity of the saddle-node bifurcations for sufficiently small $D_c \gtrsim D_m$, no stationary patterns exist, but there are still small regions of lateral instability.
- [86] Y. Nishiura and H. Fujii, *SIAM Journal on Mathematical Analysis* **18**, 1726 (1987).
- [87] A. B. Goryachev and M. Leda, *Molecular Biology of the Cell* **28**, 370 (2017).
- [88] P. Manneville, *Dissipative structures and weak turbulence*, edited by P. Manneville (Academic Press, Boston, 1990).
- [89] V. I. Arnold, *Geometrical Methods in the Theory of Ordinary Differential Equations*, 2nd ed., edited by M. Levi (Springer, New York, 1988).
- [90] J. Murdock, *Normal Forms and Unfoldings for Local Dynamical Systems*, Springer Monographs in Mathematics (Springer, New York, 2003).
- [91] R. Wedlich-Söldner, *Science* **299**, 1231 (2003).
- [92] H.-O. Park and E. Bi, *Microbiology and Molecular Biology Reviews* **71**, 48 (2007).
- [93] J. Lutkenhaus, *Annual Review of Biochemistry* **76**, 539 (2007).

- [94] J. M. Weimer, Y. Yokota, A. Stanco, D. J. Stumpo, P. J. Blackshear, and E. Anton, *Development* **136**, 2965 (2009).
- [95] K.-T. Park, W. Wu, K. P. Battaile, S. Lovell, T. Holyoak, and J. Lutkenhaus, *Cell* **146**, 396 (2011).
- [96] N. W. Goehring and S. W. Grill, *Trends in Cell Biology* **23**, 72 (2013).
- [97] S. G. Martin and R. A. Arkowitz, *FEMS Microbiology Reviews* **38**, 228 (2014).
- [98] F. Wu, J. Halatek, M. Reiter, E. Kingma, E. Frey, and C. Dekker, *Molecular Systems Biology* **12**, 873 (2016).
- [99] M. Guzzo, S. M. Murray, E. Martineau, S. Lhospice, G. Baronian, L. My, Y. Zhang, L. Espinosa, R. Vincenzelli, B. P. Bratton, and et al., *Nature Microbiology* **3**, 948 (2018).
- [100] P. Gross, K. V. Kumar, N. W. Goehring, J. S. Bois, C. Hoege, F. Jülicher, and S. W. Grill, *Nature Physics* (2018), 10.1038/s41567-018-0358-7.
- [101] M. Howard, A. D. Rutenberg, and S. de Vet, *Physical Review Letters* **87** (2001), 10.1103/physrevlett.87.278102.
- [102] K. C. Huang, Y. Meir, and N. S. Wingreen, *Proceedings of the National Academy of Sciences* **100**, 12724 (2003).
- [103] A. Gamba, I. Kolokolov, V. Lebedev, and G. Ortenzi, *Journal of Statistical Mechanics: Theory and Experiment* **2009**, P02019 (2009).
- [104] J. Halatek and E. Frey, *Cell Reports* **1**, 741 (2012).
- [105] S. Alonso and M. Bär, *EPJ Nonlinear Biomedical Physics* **2** (2014), 10.1140/epjnbp14.
- [106] D. Cusseddu, L. Edelstein-Keshet, J. Mackenzie, S. Portet, and A. Madzvamuse, *Journal of Theoretical Biology* (2018), 10.1016/j.jtbi.2018.09.008.
- [107] R. Gesele, J. Halatek, and E. Frey, (2018), 10.1101/451880.
- [108] M. Loose, E. Fischer-Friedrich, J. Ries, K. Kruse, and P. Schwille, *Science* **320**, 789 (2008).
- [109] V. Ivanov and K. Mizuuchi, *Proceedings of the National Academy of Sciences* **107**, 8071 (2010).
- [110] A. G. Vecchiarelli, M. Li, M. Mizuuchi, and K. Mizuuchi, *Molecular Microbiology* **93**, 453 (2014).
- [111] Y. Caspi and C. Dekker, *eLife* **5**, e19271 (2016).
- [112] S. Kretschmer, K. Zieske, and P. Schwille, *PLOS ONE* **12**, e0179582 (2017).
- [113] P. Glock, J. Broichhagen, S. Kretschmer, P. Blumhardt, J. Mücksch, D. Trauner, and P. Schwille, *Angewandte Chemie International Edition* **57**, 2362 (2018).
- [114] A. H. Chau, J. M. Walter, J. Gerardin, C. Tang, and W. A. Lim, *Cell* **151**, 320 (2012).
- [115] L. Marcon, X. Diego, J. Sharpe, and P. Müller, *eLife* **5** (2016), 10.7554/elife.14022.
- [116] S. S. Sugai, K. L. Ode, and H. R. Ueda, *Cell Reports* **19**, 863 (2017).
- [117] X. Diego, L. Marcon, P. Müller, and J. Sharpe, *Physical Review X* **8** (2018), 10.1103/physrevx.8.021071.
- [118] A. Eldar, B.-Z. Shilo, and N. Barkai, *Current Opinion in Genetics & Development* **14**, 435 (2004).
- [119] P. Politi and C. Misbah, *Physical Review Letters* **92** (2004), 10.1103/physrevlett.92.090601.
- [120] P. Politi and C. Misbah, *Physical Review E* **73** (2006), 10.1103/physreve.73.036133.
- [121] N. Verschuere and A. Champneys, *SIAM Journal on Applied Dynamical Systems* **16**, 1797 (2017).
- [122] B. Alberts, A. Johnson, J. Lewis, M. Raff, K. Roberts, and P. Walter, *Molecular Biology of the Cell*, 5th ed. (Garland Science, New York, 2007).
- [123] F. O. Bendezu and S. G. Martin, *Science Signaling* **5**, pe53 (2012).
- [124] J. W. Cahn and J. E. Hilliard, *The Journal of Chemical Physics* **28**, 258 (1958).
- [125] P. D. Olmsted, *Rheologica Acta* **47**, 283 (2008).
- [126] T. Divoux, M. A. Fardin, S. Manneville, and S. Lerouge, *Annual Review of Fluid Mechanics* **48**, 81 (2016).
- [127] P. C. Hohenberg and B. I. Halperin, *Reviews of Modern Physics* **49**, 435 (1977).
- [128] P. C. Fife, *Electronic Journal of Differential Equations* **2000**, 1 (2000).
- [129] F. Bai, C. M. Elliott, A. Gardiner, A. Spence, and A. M. Stuart, *Nonlinearity* **8**, 131 (1995).
- [130] C. Dupaix, D. Hilhorst, and I. Kostin, *Journal of Dynamics and Differential Equations* **11**, 333 (1999).
- [131] R. Wittkowski, A. Tiribocchi, J. Stenhammar, R. J. Allen, D. Marenduzzo, and M. E. Cates, *Nature Communications* **5**, 4351 EP (2014).
- [132] A. P. Solon, J. Stenhammar, M. E. Cates, Y. Kafri, and J. Tailleur, *New Journal of Physics* **20**, 075001 (2018).
- [133] J. K. G. Dhont and W. J. Briels, *Rheologica Acta* **47**, 257 (2008).
- [134] M.-A. Fardin, O. Radulescu, A. Morozov, O. Cardoso, J. Browaeys, and S. Lerouge, *Journal of Rheology* **59**, 1335 (2015).
- [135] S. M. Fielding, *Physical Review Letters* **104** (2010), 10.1103/physrevlett.104.198303.
- [136] S. M. Fielding, *Soft Matter* **3**, 1262 (2007).
- [137] M. Turcio, A. E. Chávez, J. E. López-Aguilar, R. O. Vargas, A. Capella, and O. Manero, *Physics of Fluids* **30**, 114104 (2018).
- [138] S. Alonso and M. Bär, *Physical Biology* **7**, 046012 (2010).
- [139] M. C. Marchetti, J. F. Joanny, S. Ramaswamy, T. B. Liverpool, J. Prost, M. Rao, and R. A. Simha, *Reviews of Modern Physics* **85**, 1143 (2013).
- [140] J.-B. Caussin, A. Solon, A. Peshkov, H. Chaté, T. Dauxois, J. Tailleur, V. Vitelli, and D. Bartolo, *Physical Review Letters* **112** (2014), 10.1103/physrevlett.112.148102.
- [141] M. E. Cates and J. Tailleur, *Annual Review of Condensed Matter Physics* **6**, 219 (2015).
- [142] A. P. Solon, H. Chaté, and J. Tailleur, *Physical Review Letters* **114**, 068101 (2015).
- [143] A. P. Solon, J.-B. Caussin, D. Bartolo, H. Chaté, and J. Tailleur, *Physical Review E* **92** (2015), 10.1103/physreve.92.062111.
- [144] M. M. Genkin, A. Sokolov, O. D. Lavrentovich, and I. S. Aranson, *Physical Review X* **7** (2017), 10.1103/physrevx.7.011029.
- [145] A. Forrow, F. G. Woodhouse, and J. Dunkel, *Physical Review Letters* **119** (2017), 10.1103/physrevlett.119.028102.
- [146] A. Doostmohammadi, J. Ignés-Mullol, J. M. Yeomans, and F. Sagués, *Nature Communications* **9** (2018), 10.1038/s41467-018-05666-8.
- [147] L. Huber, R. Suzuki, T. Krüger, E. Frey, and A. R. Bausch, *Science* **361**, 255 (2018).
- [148] I. Maryshev, A. B. Goryachev, D. Marenduzzo, and A. Morozov, *arXiv:1806.09697* (2018).
- [149] I. S. Aranson and L. S. Tsimring, *Reviews of Modern Physics* **78**, 641 (2006).

- [150] F. Sagués, J. M. Sancho, and J. García-Ojalvo, [Reviews of Modern Physics](#) **79**, 829 (2007).
- [151] T. Biancalani, F. Jafarpour, and N. Goldenfeld, [Physical Review Letters](#) **118** (2017), 10.1103/physrevlett.118.018101.
- [152] M. F. Weber and E. Frey, [Reports on Progress in Physics](#) **80**, 046601 (2017).
- [153] S. Smith and N. Dalchau, [Journal of The Royal Society Interface](#) **15**, 20170805 (2018).
- [154] L. Sewalt, A. Doelman, H. Meijer, V. Rottschäfer, and A. Zagaris, [Physica D: Nonlinear Phenomena](#) **298-299**, 48 (2015).
- [155] A. Doelman, L. Sewalt, and A. Zagaris, [Chaos](#) **25**, 036408 (2015).
- [156] B. Fiddler, ed., *Handbook of Dynamical Systems*, Vol. 2 (Elsevier, 2002).
- [157] T. Kolokolnikov, M. J. Ward, and J. Wei, [Studies in Applied Mathematics](#) **115**, 21 (2005).
- [158] T. Kolokolnikov and R. McKay, [Discrete and Continuous Dynamical Systems - Series B](#) **17**, 191 (2011).